List of Publications

1. A Ansari, D Mohanta, A Saha, Exploiting valence band mapping and select blue-green and red phosphorescence decay of γ-irradiated nanoscale Eu^{3+}:Gd_2O_3 below concentration quenching, *Optical Materials*, **122**, 111627, 2021.

2. A Ansari, S Dey, D Mohanta, Significant red-luminescence from citrate-gel and hydrothermally derived nanoscale Eu^{3+}:Gd_2O_3 with alkali metal ion (Na^+, K^+) co-doping, *Bulletin of Materials Science*, **45 (1)**, 1-12, 2022.

3. A Ansari, D Mohanta, Structural and XPS studies of polyhedral europium doped gadolinium orthovanadate (Eu^{3+}:$GdVO_4$) nanocatalyst for augmented photodegradation against Congo-red, *Physica E: Low-dimensional Systems and Nanostructures*, **115357**, 2022.

Conferences:

1. *ISNSCON 2018 6th World Congress on Nanomedical Sciences*, Jamia Hamdard and University of Delhi, Vigyan Bhawan, New Delhi, 2019

2. *International Virtual Conference on Advances in Functional Materials* (AFM 2020), KIIT, Odisha, India.

3. *Condensed Matter Days 2018*, (CMDAYS-2018), Department of Physics, University of Burdwan, West Bengal.

Addenda

Optical Materials 122 (2021) 111627

Contents lists available at ScienceDirect

Optical Materials

journal homepage: www.elsevier.com/locate/optmat

Research Article

Exploiting valence band mapping and select blue-green and red phosphorescence decay of γ-irradiated nanoscale Eu^{3+}: Gd_2O_3 below concentration quenching

Aftab Ansari [a], Dambarudhar Mohanta [a,*], Abhijit Saha [b]

[a] Nanoscience and Soft-Matter Laboratory, Department of Physics, Tezpur University, PO: Napaam, Tezpur, 784028, Assam, India
[b] UGC-DAE Consortium for Scientific Research, Kolkata Centre, Sector III, LB-8, Bidhan Nagar, Kolkata, 700 106, West Bengal, India

ARTICLE INFO

Keywords:
Phosphor
Eu^{3+} transition
Gadolinium oxide
γ-irradiation
TR-PL
XPS

ABSTRACT

We report on manifested blue-green and red emission features in Eu^{3+} doped Gd_2O_3 nanophosphors, subjected to 1.3 MeV gamma (γ) -irradiation and up to a dose of 2.4 kGy. While Eu^{3+} states can be predicted at the core, occurrence of divalent species (Eu^{2+}) at the nanoparticle surfaces was revealed from the X-ray photoelectron spectroscopy (XPS) studies. Characteristic Eu^{3+} activated orange-red emissions (590–650 nm) were revealed, and the nature of the corresponding transitions assigned. Moreover, time resolved photoluminescence (TR-PL) technique was employed to evaluate the lifetime of carriers participating in specific recombination emission events with and without specimens being exposed to γ -rays. The lifetime decay of our nanophosphor ranges between ~1.6–1.3 ms, for electrically driven (ED: $^5D_0 \rightarrow {}^7F_2$) and ~1.98–1.56 ms, for magnetically driven (MD: $^5D_0 \rightarrow {}^7F_1$) emissions. The modulation of ED and MD transitions in a suitable nanophosphor will have immense scope in next generation smart windows, display panels and bioimaging prospects.

1. Introduction

The use of rare earth (RE) elements, in pure and oxide forms, is not necessarily rare. The RE oxides have drawn growing interest in the last few decades due to their excellent optoelectronic properties and accordingly, their scope can be realized in a wide range of applications. To name a few, are low threshold lasers, high performance luminescent panels, drug-carrying vehicles, magnetic resonance imaging (MRI) contrast agent, frequency up-converters, biosensors and labels as well as photocatalytic agents. The RE oxides have been extensively used as luminescent probes, with Gd_2O_3 being extremely popular in processing efficient nanophosphors [1]. Furthermore, it could ensure high thermal and chemical stability, low phonon cut-off energy while being in different crystallographic phases, i.e., monoclinic, cubic and hexagonal [2]. Gd^{3+} ions possess a maximum of seven unpaired, *4f* electrons ($^8S_{7/2}$) that would give rise to an optimal electron magnetic moment, not experienced by any other elements in the periodic table [3].

Often the RE phosphors include lanthanide ions as activation centers with appropriate energy spacing. At large, two kinds of activation centers are involved in the phosphors, either as emission centers and/or trap centers. Lanthanide ions, such as Ce^{3+}, Eu^{3+}, Nd^{3+} with *5d* → *4f*, or *4f* → *4f* transitions act as emission centers [4]. Trap centers can be lattice/intrinsic defects (e.g., oxygen vacancies (V_O), *F*-centers, anti-site defects), impurities (e.g., Cu^{+}, Co^{2+}, Ti^{3+}) [5], and also aliovalent or isovalent co-dopants (e.g., Dy^{3+} in $SrAl_2O_4$:Eu^{2+}) [6]. Both the emission/trap centers are located well inside the forbidden gap. The trap centers can either be electron trap, or hole trap depending on whether they exist a few electron volts (eV) below the bottom of conduction band (CB), or above the top of valence band (VB). The physical mechanism, which includes four main processes are discussed vividly in earlier reports [7]. They are namely *i) excitation*: illumination of a phosphor by external sources at specific wavelengths leading to the liberation of charge carriers (electrons and/or holes), *ii) trapping process*: non-radiative capture of charge carriers by the electron through CB, or hole traps through VB. Quantum tunneling process through the forbidden band can also be realized in the trapping process under suitable conditions, *iii) de-trapping process*: upon termination of excitation, the captured charge carriers can get released via thermal/optical energy of stimulation [7,8], finally, *(iv) recombination*: the released charge carriers move back to the emission centers yielding delayed luminescence via *e-h* recombination mechanisms. Consequently, the wavelength of emission desired is the characteristic feature of emission centers and

* Corresponding author.
E-mail address: best@tezu.ernet.in (D. Mohanta).

https://doi.org/10.1016/j.optmat.2021.111627
Received 17 June 2021; Received in revised form 21 September 2021; Accepted 26 September 2021

that the intensity and duration of the luminescence profiles are invariably determined by the parameters relating the trap centers, such as trap depth, trap density, or concentration. Thus the detailed mechanism of phosphorescence can be exploited by choosing the host and the concentration of dopants judiciously.

Moreover, the transitions relating to lanthanide-based phosphors are unique considering their forbidden nature. In general, trivalent lanthanide-doped complexes have their $4f^n$ subshell shielded by the $5s^2$ and $5p^6$ subshells that display line emission features [9]. Thus, the most important Hamiltonian to determine the energy level of $4f$ is the atomic part (H_A), and the position pattern of the spectral terms of each lanthanide ion is mainly determined by the spin–orbit interaction (H_{SO}) of the electrons [10]. However, when the ion is introduced into a crystal lattice, the crystal field can distort the partly filled $4f$ electron shell to have multiplets being split and shifted upon the interaction of localized $4f$ electrons with the local electric field of the crystal. The number of energy levels and their energies arising from the J-term splitting are of major concern in the crystal field theory. Numerous reports predict selective emissions as a consequence of allowed electrically driven ($^5D_0 \rightarrow {}^7F_2$), or magnetically driven ($^5D_0 \rightarrow {}^7F_1$) transitions [9,11]. However, their tunable optical properties with varying dopant concentration and emphasizing radiation treatment are not yet discussed in the existing literature. More precisely, the *5d-4f* transitions can be influenced greatly with the incorporation of selectively chosen RE dopant and intentionally introduced defect states/trap centers via radiation exposure [12,13]. Previously, thermoluminescence (TL) glow curves were studied after generation of defects due to γ-irradiation effect [14]. As TL glow curves arise because of thermal excitation and not inter band electronic excitation they cannot offer valuable information as regards, involved *D-F* transitions.

In this study, we present the effect of γ-irradiation on the forbidden transitions and the effect of traps/defect sites generated on the hypersensitive transitions of Eu^{3+}. Also, the nature and dynamics of luminescence response of Eu^{3+} doped Gd_2O_3 nanoparticles are discussed emphasizing radiation induced phenomena. A detailed view relating to the effect of dopant concentration as well as γ-doses has been deliberated considering manifested radiative transitions via electrically and magnetically driven lifetime components. Moreover, a simple theoretical treatment has been employed while discussing the role of dopant environment on select radiative events. X-ray photoelectron spectroscopy (XPS) further enables us to have an in-depth profiling of our nanophosphor specimen for several surface related revelations. Emitted photoelectrons upon incident X-rays are analyzed for their energy and intensity, while revealing the oxidation states of the elements present in the system. We came across to only a limited number of available reports that dealt with a detailed description of XPS analysis for the RE doped nanophosphors [15–17]. Highlighted in the beginning of analysis section, our XPS study also aims to bridge the gap in existing literature, disclosing weighted information from the outermost layers of the as prepared Eu^{3+}: Gd_2O_3 nanophosphor.

2. Experimental: materials and methods

2.1. Processing Gd_2O_3 nanophosphor via citrate-gel route

Unlike many other oxides which are relatively easy to synthesize, nanometric REOs demand appropriate routes owing to their excellent chemical and mechanical stability. In fact, top-down approaches, which generally rely on crushing and smashing are never easy for the REO yielding its nanoscale form. Nevertheless, allowing aggregation of molecular species combined with the formation of a less-stable hydroxide form, and subsequent reduction to its oxide form is an attractive means in the bottom-up approach. Here, nanoscale Gd_2O_3 product is derived through a citrate-gel method following relevant steps described elsewhere [18,19], but with slight modification. At first, gadolinium acetate (GdAc) [$Gd(CH_3COO)_3$, CDH, 99.9% pure] is dispersed in millipore® (deionized, DI) water followed by preparation of a equimolar solution with the addition of citric acid (CDH, 99% pure) under vigorous stirring (~300 rpm, ½ h). Then the as-received gel-like mixture was placed carefully in a hot-air oven, maintaining a temperature of 90 °C. The annealing process facilitates adequate reduction of GdAc to $Gd(OH)_3$ and subsequent removal of the undesired water content. The Gd_2O_3 nanopowder is acquired after calcination at a relatively high temperature (~600 °C) for a time duration of nearly 5 h. Next, the product was subjected to repeated washing and centrifugation (~6000 rpm) followed by filtration steps prior to oven heating (~80 °C) overnight. The final product is preserved in a desiccator for subsequent experimentation.

In order to synthesize europium doped Gd_2O_3 nanopowder, europium acetate (CDH, 99% pure) is considered as the key-reactant. A suitable amount of the reactant was added to the sol after completion of the first step in the above-mentioned route and consequently, several batches of nanoscale Gd_2O_3 systems could be derived with the inclusion of Eu dopant in the range of 1–7%. The nanoscale, pristine and Eu^{3+} doped Gd_2O_3 systems are labeled as, GNP and EuGNP; respectively. As for the irradiation experiment, γ –photons of average energy ~1.3 MeV (available from a Co^{60} source facility at UGC-DAE CSR, Kolkata) are employed at a rate of 1.75 kGy/h, choosing two doses of ~0.9 kGy and 2.4 kGy. Kept in borosilicate glass vials, the GNP and EuGNP nanopowders were first dispersed in deionized water and then sealed air-tight prior to transferring into the shielded irradiation chamber.

2.2. Analytical techniques

To reveal structural characterization of the GNP and EuGNP nanosystems, a Rigaku mini-Flex X-ray diffractometer (XRD) equipped with CuK_α radiation ($\lambda = 1.54$ Å) has been employed, while diffraction data is acquired in the range of Bragg's angle (2θ) ~ 10–80°, and in steps of 0.05°. Moreover, morphological feature of the nanometric Gd_2O_3 is revealed through the transmission electron microscopy (TEM) imaging performed on a JEOL 2100 machine. Furthermore, photoluminescence (PL) emission and time resolved photoluminescence (TR-PL) spectra are captured on a luminescence spectrophotometer with the time correlated single photon counting (TCSPC) capability (Horiba, USA). At first, steady state spectral emission features are acquired corresponding to specific excitation lines (wavelength, $\lambda_{ex} = 300$ nm and 400 nm) in the present case. While the first excitation line was chosen to acquire the characteristic feature in the deep-blue regime, the second excitation line offered spectral emission features especially in the red regime. Furthermore, TR-PL decay profiles are acquired for specific wavelength of emissions. On the other hand, Raman spectra are recorded by employing a Renishaw In-Via Raman spectrometer (Renishaw, Wottonunder- Edge, UK) and using the 514.5 nm line of Ar^+ laser as the excitation source, while the detector assembly provided data resolution of ~0.3 cm^{-1}. XPS based analysis is also made by means of Thermo-Scientific ESCALAB Xi $^+$ spectrometer having a monochromatic Al K_α X-ray source (1486.6 eV) and a spherical energy analyzer that operates in the CAE (constant analyzer energy) mode using the electromagnetic lenses.

3. Results

3.1. Morphological and structural analyses of Eu^{3+}: Gd_2O_3 nanophosphor

A series of X-ray diffractograms of the undoped and Eu^{3+} doped Gd_2O_3 nanosystems are depicted in Fig. S1(a), and then shown independently in Fig. S1(b-f). The diffractograms essentially show four prominent peaks positioned at the Bragg's angles (2θ) of 28.57°, 33.11°, 47.52°, and 56.4° assigned to the (222), (400), (440), (622) crystallographic planes of the cubic phase Gd_2O_3 system, with space group no. 199 (*I-213*) (JCPDS no. 76–0155) [20]. The corresponding FWHM

values are displayed in Table S1. We employed Vesta® to determine the interplanar spacings of the afore-mentioned crystallographic planes and found to be, ~0.31 nm, 0.27 nm, 0.19 nm and 0.16 nm. Ignoring the instrument line broadening aspect, the average crystallite size (d) and micro-strain (ε) of the nanosystems can be estimated through the well-known Williamson-Hall (W–H) formula:

$$\beta cos\theta = \frac{0.9\lambda}{d} + 4\varepsilon sin\theta. \quad (1)$$

In eqn. (1), β is the full width at half maxima (FWHM) in radians, θ is the diffraction angle in degrees and λ is the wavelength (CuK_α, 1.543 Å) of the X-rays employed. We obtained d ~18 nm, with the typical microstrain value found in the order of 10^{-4}, in most cases.

The microscopic information can be visualized through the TEM images, depicted in Figure S2(a,b). Here, nanocrystalline feature of the GNP and 3%EuGNP specimens with a thin amorphous surface layer due to citric acid coating has been witnessed. The SAED patterns, shown as figure-insets in sub-figure (i) essentially exhibit concentric ring-type patterns along with distinct bright spots featuring local departure from the perfect periodicity. In both Figure S2 (a) and (b), shown in (iv), the magnified part of (i), would highlight nanoparticles with lattice fringes oriented in different directions. In Figure S2(a), the HRTEM sub-figures (ii) and (v) represent lattice fringe patterns of two distinct nanoparticles highlighting positions of the normal atomic sites and point defects. With the help of *ImageJ*®, the respective interplanar spacings were determined from the plots for grey values against distance and estimated to be, ~0.28 nm and ~0.3 nm and corroborate with the (400) and (222) planes of the cubic phase Gd_2O_3; respectively [3]. Corresponding fast Fourier transform (FFT) images of the two-lattice pattern-types are shown in (iii) and (vi). Similar analyses were also made for 3% EuGNP specimen with corresponding lattice spacings being ~0.27 nm and 0.29 nm for (400) and (200) planes; respectively.

3.2. XPS based revelations

3.2.1. Valence band mapping

The valence band mapping (VBM) spectra can be found in Fig. 1 (A) (a). The spectra were subjected to deconvolution with the background for the spectra subtracted according to the well-known Tougaard rule [21] as depicted in Fig. 1 (A) (b-f). The most important observation in the spectra, i.e. the valance band maximum was determined to be ~8.4 eV, which is highly typical for cubic Gd_2O_3 phase [22]. The plot with normalized intensity in Fig. 1A (g) reveals that the spectra for all europium doping levels retain their profile.

In order to have a better insight into the valence band structure and influence of Eu incorporation, we determined the intensity and FWHM ratios as shown in Fig. 1 (B), involving the various states. In Fig. 1 (B) (a), we observe an intensity drop for Gd*4f* in 3% doped EuGNP system with a rise in higher doping levels; similar observations are also made for Gd*5p*-O*2s* overlap. In Fig. 1B (b), we observe highest peak intensity for the signal corresponding to O^{2-} defects in the case of highest doping level considered-i.e., 7% doped EuGNP system. We also observed that, the intensity ratio for Gd*4f* and the Gd*5p*-O*2s* overlap is maximum for such case (Fig. 1 (B) (c)).

3.2.2. XPS based surface revelations

Fig. 2 (A) (a-e) displays the complete XPS spectra revealing Gd*4d* and *3d* states along with occurrence of O*1s* peak. Upon Eu inclusion as dopant, a short peak at ~1137 eV has been observed, which is of prime interest as this peak is a characteristic of +3 oxidation sate of Eu [17]. Auger lines are prominent in any spectrum and are also observed in K-L-L shells ~1013, 999, 978 eV etc. Moreover, we captured peaks at

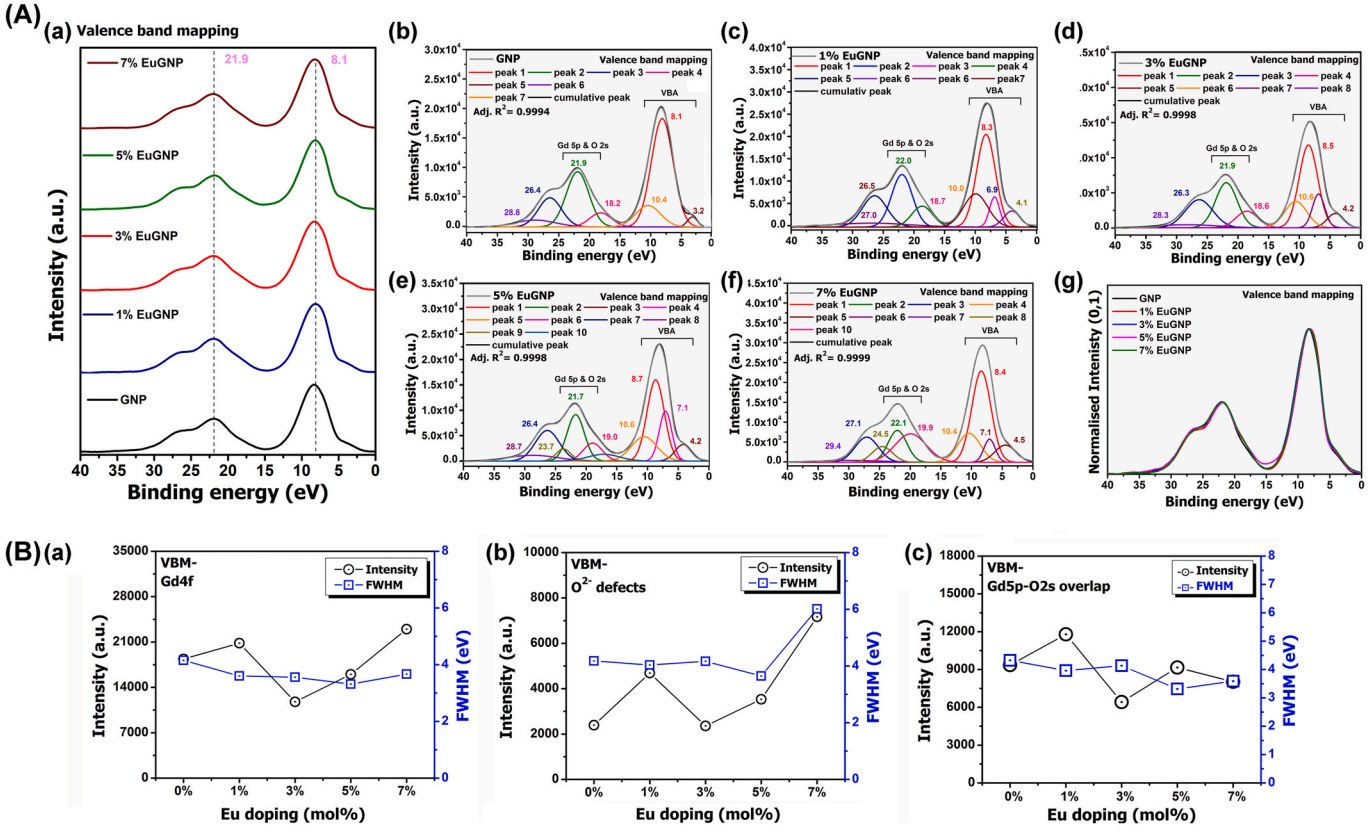

Fig. 1. **(A) (a)** Comparative plot for valence band mapping (VBM) spectra of the as-prepared samples with individual deconvoluted profiles shown in (b), (c), (d), (e) and (f) for GNP, 1% EuGNP, 3% EuGNP, 5% EuGNP and 7% EuGNP respectively; (g) displays the plot with normalized intensity for the above mentioned sample profiles. **(B)** Comparative accounts of intensity of signals corresponding to (a) Gd*4f*, (b) O^{2-} defects, and (c) Gd*5p*-O*2s* overlap are shown.

~529.8 eV, corresponding to the known +3 oxidation state of Gd [23]. All dopant concentrations, except the upper limit (7% doped EuGNP) case, have offered the aforesaid peak.

3.2. 2.1 XPS Gd4d and O1s core level spectra. The XPS core level spectra, corresponding to the Gd*4d* photoemission lines observed were studied comprehensively. Shirley rule for background correction was followed while deconvolution and two major peaks were displayed in Fig. 2 (B) (g-k) [24]. The peak maxima ~142 eV is assigned to the Gd(III) species, while the other peak at 147 eV can be considered mainly due to low-spin of the system, with a usual spin polarization of 0.39 [17]. The acquired photoemission features being depicted in Fig. 2(C).

In Fig. 2 (D) we find both the Intensity ratio as well as FWHM ratio of ^9D state (~147 eV) with respect to ^7D state (~143 eV). Whereas, Fig. 2 (E) displays the core level spectra for O*1s* of the various samples characterizing a plot profile with asymmetrical twin peaks between 535 eV and 530 eV O1s spectra typically consists of a main signal due to O^{2-} and Gd^{3+} bond at ~529.4 eV, while the sub-peak located at 532.1 eV is due to the hydrated oxygen species [31]. The deconvoluted spectra offer a rather very complex nature of overlapping peaks, assigned to the

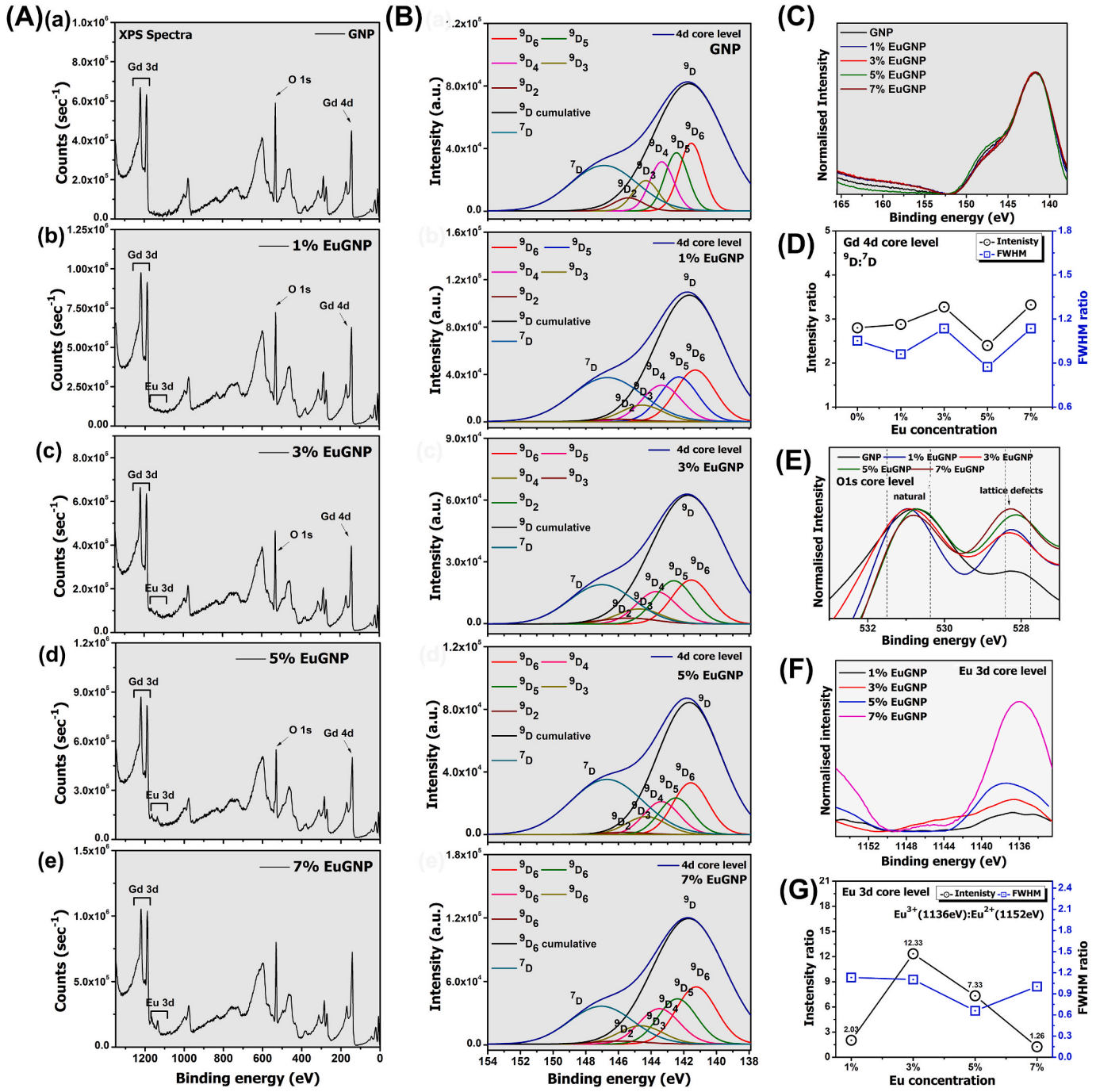

Fig. 2. A(a-e) Complete XPS spectra revealing Gd *4d* and *3d* states along with occurrence of O*1s* peak. The XPS core level spectra corresponding to the Gd*4d* photoemission lines observed were studied comprehensively, with their deconvoluted profiles shown in B(a-e) for varied dopant concentrations. The photoemission lines being shown in Fig. (C). (D) Relative intensity as well as FWHM ratio of 9*D* state (~147 eV) with respect to 7*D* state (~143 eV) in Gd*4f* profiles while (E) displays the core level spectra for O*1s*. (F) Eu *3d* core level spectra for the studied samples with plots for relative intensity and FWHM ratio for prominent peaks observed shown in (G).

contributing factors as mentioned in Table 1 and Supplementary, Fig. S3 (a-e).

3.2. .2.2. XPS Eu3d core level spectra. Fig. 2F essentially depicts the Eu*3d* core level spectra for the EuGNP samples and we observed that the spectra gained a well-defined profile as the doping concentration increases. The major peaks of our concern could be probed after deconvolution, first being centred at, ~1136 eV while other one appeared as satellite peak at, ~1152 eV that corresponded to +3 and +2 oxidation states of Eu, respectively [15,16,25]. The deconvoluted spectra are presented in Figure S3 (f-i)), in the *Supplementary,* while Fig. 2G displays the plot for intensity and FWHM ratios of the concerned peaks.

3.3. Carrier transitions analyzed through optical spectroscopy

The absorption and reflectance characteristics of the GNP and EuGNP nanosystems can be found in Figure S4. As for the undoped GNP system (Figure S4(a)), a poorly resolved peak observed at ~230 nm, arises due to the $^8S_{7/2}$ to $^6D_{9/2}$ transitions within the Gd^{3+} matrix and otherwise termed as host excitation band by earlier groups [26]. In case of 1% and 3% doped EuGNP nanosystems, the broad peak maxima at ~276 nm, 360 nm have arisen due to intra *f* band transitions of Eu^{3+} ions. However, these *f-f* transitions are absent in case of 5% and 7% EuGNP nanosystems (Figure S4(d,e)). Instead, a 'charge transfer band' (CTB) centred at ~235 nm and arising due to the charge transfer between the 7*f* orbitals of the dopant Eu^{3+} and 2*p* orbital of the host O^{2-} can be witnessed.

Usually, the optical band gap is derived from the Tauc's plot following the power law expression given by equation (2) below. The optical gaps can also be determined through a model proposed by Kumar et al. [27]. Following eqn. (2), this method incorporates the phononic absorption and takes into account its contribution to the band gap as shown in Figure S4 (b,d,f,h,j). We have,

$$\alpha(h\upsilon) = F(h\upsilon) = \frac{\{1 - R(h\upsilon)\}^2}{2R(h\upsilon)} \quad (2)$$

$$\alpha h\upsilon = \frac{ln\left[\frac{[(R_{max} - R_{min})}{(R(h\upsilon) - R_{min}}\right]}{2l}. \quad (3)$$

Here, α is absorption coefficient, R is reflectance, and l as optical path length. While it is well known that Gd based oxides always come with a very wide band gap (~5 eV), in the present case it was estimated as, ~5.3 eV. The band gaps and phonon absorption energies for the undoped GNP and Eu:GNP systems, as predicted through Kumar's model are depicted in Figure S4(k).

3.4. Revealing D-F transitions through photoluminescence studies

3.4.1. Identifying D-F transitions

The room temperature steady state PL excitation (PLE) as well as PL emission spectra for both the undoped and Eu-doped GNP can be found in Fig. 3(A) (blue-green regime) and Fig. 3(B) (orange-red regime). The excitation spectra of doped GNP ($\lambda_{em} = 612$ nm) displayed a small broad peak at ~230 nm, attributed to CTB and a highly intense band centering at ~256 nm, known to result in intense emission from the $^5D_0$ levels of Eu^{3+} (inset of Fig. 3 (B)(a) [28].

Excitation at 300 nm has led the undoped Gd_2O_3 displaying two prominent peaks in the blue-green region, centred at 490 nm and 545 nm Figure S5A(a). The 538 nm peak observed can be attributed to excitation corresponding to $^8S_{7/2}$ to ^6I_J optical transitions in Gd^{3+}(Figure S5(A)(a)) [29]. Upon Eu^{3+} doping, captivatingly newer peaks were evident as in Fig. 3A(a). Upon deconvolution, the peak centers were found to be located at ~465 nm, 490 nm, 512 nm, 532 nm and 545 nm, attributing to the $^5D_2$-$^7F_0$, $^5D_2$-$^7F_2$, $^5D_2$-$^7F_1$, $^5D_1$-$^7F_1$, and $^5D_1$-$^7F_2$ transitions in Eu^{3+}; respectively [11,30]. For convenience, these transitions are annotated as, T1, T2, T3, T4, and T5; respectively (Figure S5(A)(b-j)). T4 is the most intense emission and is found to be maximum for 3% EuGNP (Fig. 3A(a), S5A(c)). T2/T5 full width becomes maximum for 3% EuGNP as can be seen in Fig. 5A(d). Strikingly, upon deconvolution, we observe the presence of very rarely reported $^5D_0$-$^7F_0$ transition, positioned at ~580 nm which is ordinarily forbidden according to the Laporte's rule and can be found from Fig. 4. Moreover, various transitions via $^5D_0$-^7F_J (J = 0,1,2,3,4) in the red and far-red regime are witnessed with intensities far greater than that from the higher excited levels (Fig. 3 B(a,b)). For clarity, these transitions are annotated as T6, T7, T8, T9, T10; respectively. Typically, ^7F_J, with $J = 0$, 2,4 (T6, T8, T10) are accompanied by ED transitions; while $J = 1,3$ (T7, T9) represent MD transitions [9]. Not surprisingly, we observe the intensity of T6 to be half to that of T7, for the 3% EuGNP specimen (Fig. 5)).

To be mentioned, close temperature dependent emission profiles are examined at two distinct temperatures (5 °C and 15 °C), for 1% and 3% doping levels (Figure S6). While comparing, higher doping levels were not considered, as they suffer from concentration quenching effect. Interestingly, upon lowering the temperature to 5 °C the intensity of ~612 nm peak in 1% EuGNP is enhanced, while the response of 3%

Table 1
Signals assigned for XPS *O1s* core level spectra for Eu^{3+}:Gd_2O_3 nanophosphor.

XPS core level spectra	Excess O and lattice defects			Natural lattice oxygen			Gd-OH bond			Anamolous bond		
	Center (eV)	Intensity ratio	FWHM	Centre (eV)	Intensity ratio	FWHM	Center (eV)	Intensity ratio	FWHM	Center (eV)	Intensity ratio	FWHM
GNP	528.2	–	1.7	532.2	–	2.0	533.6	–	2.4	535.1	–	2.5
				530.9	1.7	1.9						
				529.8	0.8	1.8						
1% EuGNP	528.5	2.1	1.4	531.4	1.4	1.5	533.6	0.3	1.4	535.8	0.4	1.7
				530.4	1.0	1.5	532.4	0.8	1.6	534.5	0.4	1.5
				529.4	0.7	1.4						
3% EuGNP	528.2	1.3	1.4	532.0	0.6	1.4	534.1	0.2	1.5	536.1	0.1	1.2
				531.1	0.9	1.4						
				530.2	0.8	1.3						
				529.2	0.7	1.4	533.0	0.5	1.4	535.2	0.2	1.4
5% EuGNP	528.7	1.5	1.3	532.9	0.3	1.4	534.0	0.2	1.4	536.4	0.3	1.4
				532.0	0.7	1.3						
	528.1	0.8	1.2	531.2	0.9	1.3						
				530.5	0.9	1.3						
				529.5	0.7	1.3						
7% EuGNP	528.1	2.1	2.0	532.3	0.3	2.2	–	–	–	–	–	–
				531.1	1.1	2.0						
				530.4	1.0	2.2						

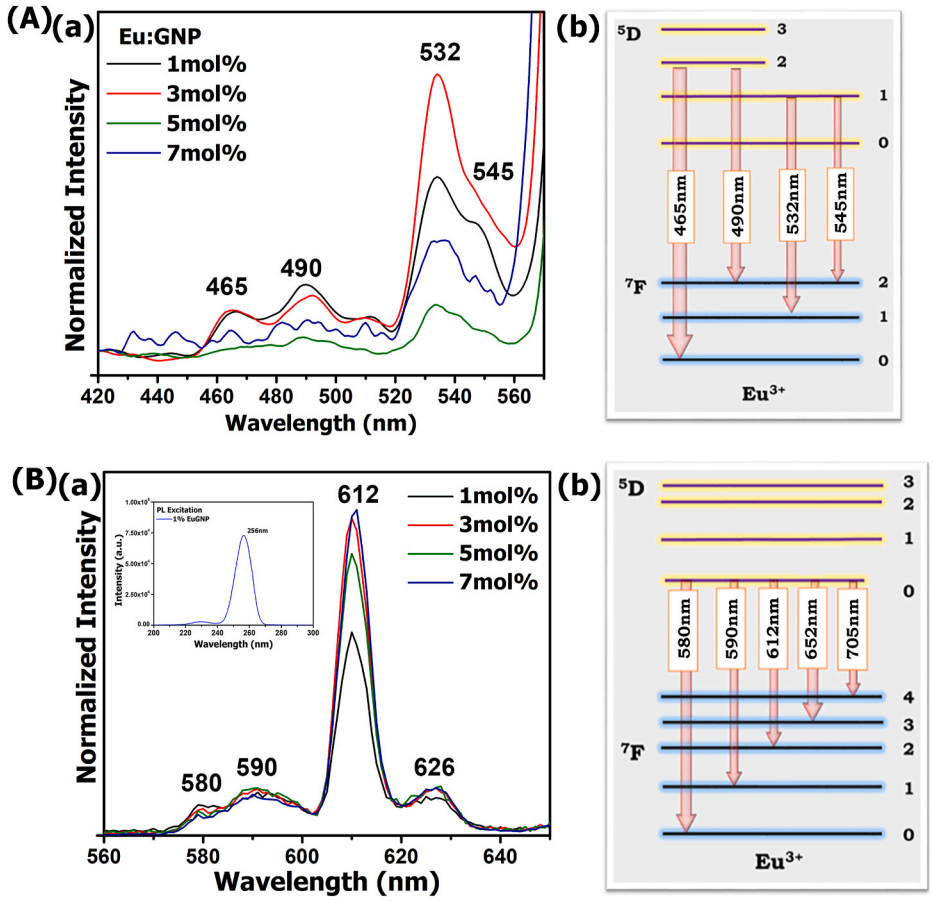

Fig. 3. PL emission profiles in (A)(a) blue-green regime, (B)(a) orange-red regime for the Eu^{3+} doped Gd_2O_3 samples. The PL excitation spectra for the EuGNP system is provided as inset of (B)(a).; The schematic diagrams for involved energy levels corresponding to the transitions observed for blue-green, and orange-red regions are depicted in (A)(b), and (B)(b); respectively.

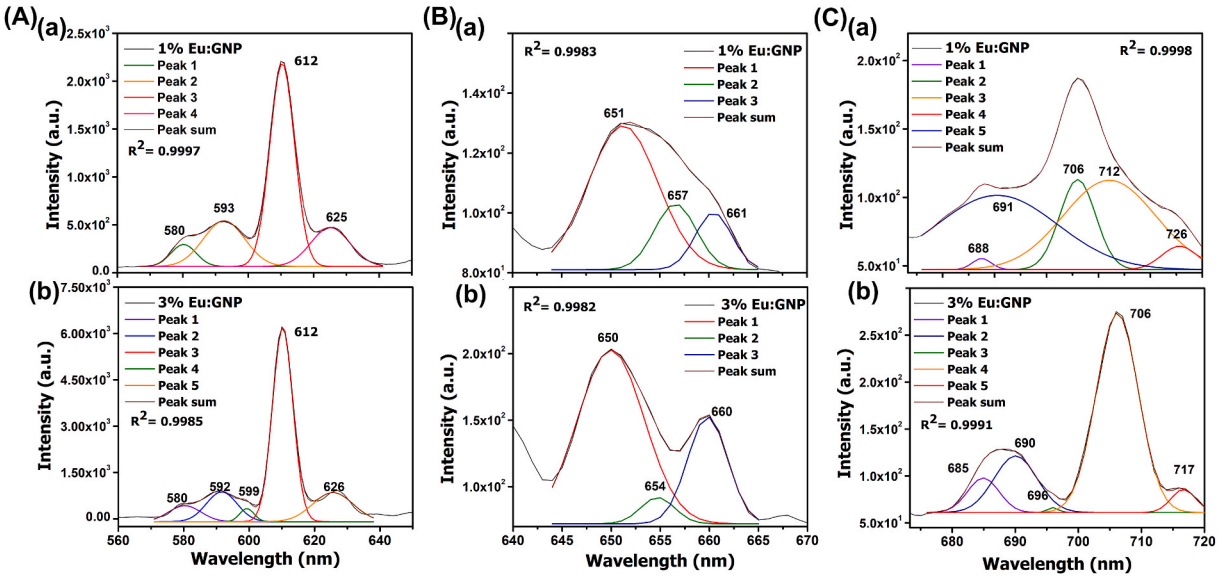

Fig. 4. Deconvoluted PL emission profiles in the orange-red regime with 400 nm excitation wavelength displaying emissions *viz.* (A) $^5D_0$-$^7F_{0,1,2}$, (B) $^5D_0$-$^7F_3$, and (C) $^5D_0$-$^7F_4$ for (a) 1% EuGNP and (b) 3% EuGNP; respectively.

EuGNP remains constant. The peak splitting was seen to be more prominent for T9 as well as T10. The vibronic intensity of T8 is known to be suppressed at lower temperatures and consequently, sharper profiles were observed [31]. The splitting of ~626 nm peak with the occurrence of peaks at 623 nm and 628 nm at 15 °C has been witnessed (Figure S6A (a)). At a temperature of 5 °C, the peaks appear at 618 nm and 627 nm. Thus with a moderate change in temperature, a pronounced effect with the occurrence of a peak at 609 nm, possibly due to splitting of most

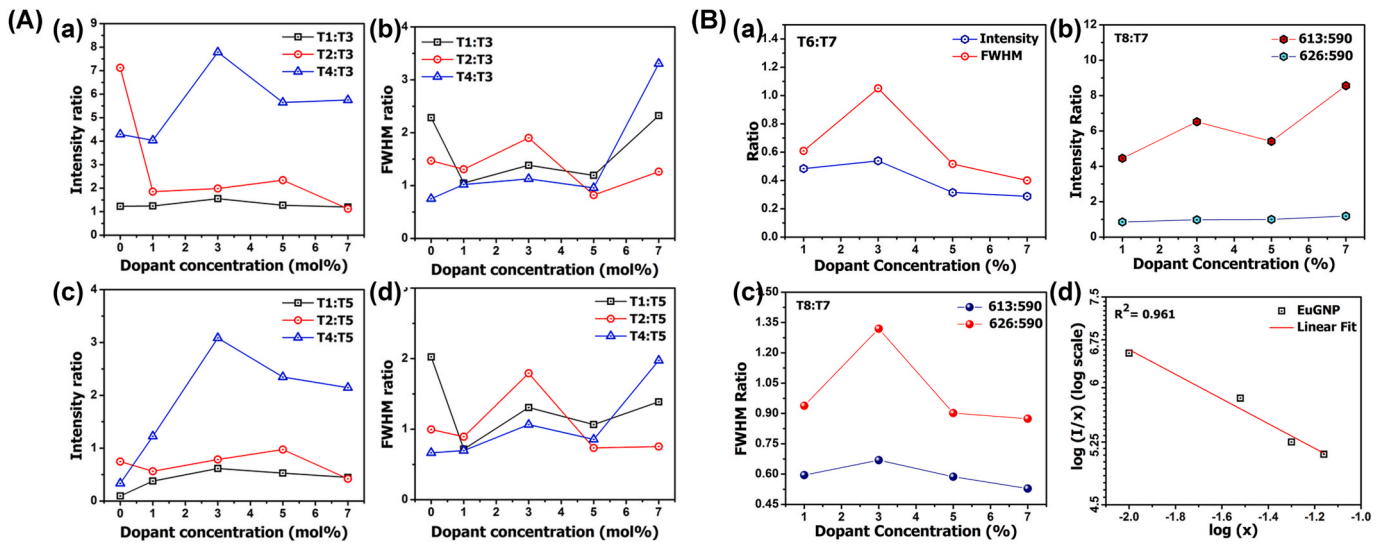

Fig. 5. Relative intensity and FWHM ratios for the various assigned PL emission peaks for the as-prepared EuGNP samples: (A)(a-d) blue-green regime, and (B)(a–c) orange-red regime. The plot according to Dexter's model following eqn. (6) for the various doped samples is depicted in B(d).

intense peak at 612 nm. The proportionate change in vibronic response may account for such an effect, and noticeable for doping levels below critical concentration.

3.4.2. Effect of γ -irradiation on radiative transitions in Eu^{3+}:Gd_2O_3 nanophosphor

The deconvoluted emission profiles for the irradiated samples are shown in Fig. 6. In reference to unirradiated system, as for the 1% EuGNP initially at irr-A (0.8 kGy), the intensity ratio T8:T7 decreased and then augmented to regain a comparable value upon subjected to irr-B (2.4 kGy). Conversely, in 3% EuGNP the intensity ratio T8:T7 first increases for irr-A and then tending to decline at the higher dose, irr-B. Another interesting feature is due to the crystal field splitting led occurrence of MD transitions ~590 nm (and 585 nm) after irradiation.

3.4.3. Photoluminescence decay dynamics of the ED and MD transitions

In all cases the build-up state did not begin from zero indicating possibility of two excitation pathways to populate the $^5D_0$ level, one being via $^5D_1$ level and the other promoting ions directly into $^5D_0$ (Fig. 7) [32]. In order to determine the decay lifetime, all curves were primarily fitted to a mono exponential function using Origin 8.5®. In our study, the lifetime of T8 is estimated to be 1.6 ms for 1% EuGNP and 1.3 ms for 3% EuGNP. The effect of irradiation can be observed to induce impacts on decay lifetime of both the doping levels considered and discussed in the next section.

4. Discussion

The as-prepared, red nanophosphors were determined to be of cubic phase through XRD analysis. Observations from TEM imaging suggests that nanopowders are composed of several nanoparticles of varied morphologies, including those of faceted polyhedral types. These nanosystems often possess facets and side-edges as evident from the micrographs. The determined lattice planes are in fine agreement with the XRD results and Vesta® based analysis. The respective interplanar spacing following the FFT of lattice fringes determined using *ImageJ*®, also support the observations made by the XRD data, and SAED patterns. Apparently, inclusion of Eu^{3+} has led to a noticeable reduction in the spacing between the successive planes due to a variation in site allocation of Eu^{3+} on the host lattice.

4.1. VBM spectra, dopant environment and defects

For further investigation into the system with special emphasis on the surface related phenomenon, we employed XPS study to visualize binding energies. Primarily, the VBM spectra revealed complex multi-band nature with various peaks observed for involved electronic levels. For clarity, we broadly classify the spectra into three regions of interest-

(i) **3–11 eV:** O*2p* partial states are revealed in this region. These states contribute to the distinctive Gd–O bonds which sometimes could overlap with Gd*4f* double peaks, also visible in this regime [22].
(ii) **17–20 eV:** In this regime, peaks that arise are usually due to oxygen vacancies (point defects) in the system, high in case of doped oxide nanosystem.
(iii) **18–24 eV:** O*2s* electronic core like states found in this region inherently overlaps with Gd*5p* peak, which is also visible at ~23 eV [22].

It was known earlier that, an increased dopant concentration in a nanosystem leads to an increase in defect sites within the lattice through substitutional or interstitial means. Also, a higher Eu concentration implies higher interaction of Eu orbitals with that for O and hence the observation of declined Gd*4f*-O*2s* overlap. The intensity drops in Gd*4f* signal for 3%EuGNP system which suggests that the interaction between the Gd^{3+} with that of the surrounding Eu^{3+} might be higher than that for other cases. It is noteworthy that proper incorporation and appropriate symmetry around the doped system facilitates enhanced interaction between the doped one and the host lattice and consequently, changes with variation in concentration.

XPS spectra revealed the presence of relevant Gd, Eu and O species, associated with distinct binding energies. Technically, the intensity in the XPS spectra is directly proportional to the number of atoms in a surface layer measured [33]. Thus the effect of increment in dopant concentration is clearly obvious from the spectra as it was evident that the signals for Eu*3d* gains intensity and offers a well-defined profile with increasing concentration. The signal corresponding to the +3 oxidation state of Gd at 529.8 eV was found to be absent in case of 7% EuGNP nanosystem. The overlapping of the peak with other peaks originating around 528 eV could be a possible explanation for the disappearance. The peak ~528 eV is, in general, attributed to lattice defects and excess O in the oxide system, confine to the nanoparticle surfaces [34]. Further

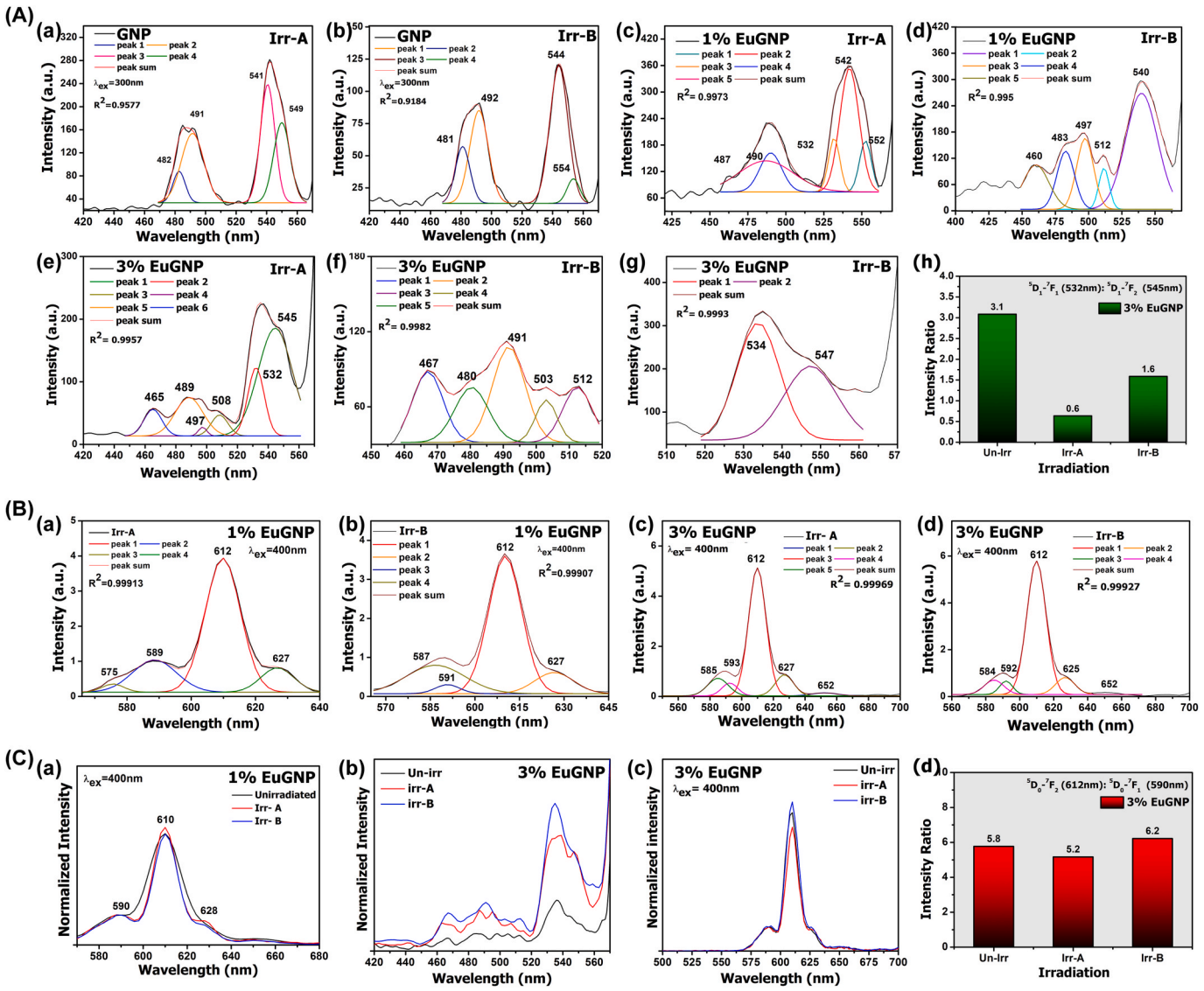

Fig. 6. PL emission analysis of as-prepared GNP and EuGNP nanophosphors for (A)(a-h) blue-green, and (B)(a-d) orange-red regions considering for both varied dopant concentration and radiation dose. Relative emission intensity for 1%EuGNP and 3%EuGNP are shown in (C)(a). and (C)(b); respectively. Note the profiles of 3%EuGNP in the (C)(b) blue-green, and (C)(c) orange-red regions. Prominent ED and MD transitions compared for both the regions are presented in (A)(h), and (C)(d); respectively.

insights could be gained with the core level XPS spectra and were comprehensively studied. Profound signals for Gd(III) species and Eu (III) species are observed from Gd*4d* and Eu*3d* core level spectra; respectively. The Gd*4d* hole and Gd*4f* electrons involve very large electrostatic interactions in between and hence a complex multiplet structure was speculated for Gd*4d* spectra. Overlapping of XPS signals lead to the displayed broad peak profiles [22]. While the key plot profiles were observed with minimal effect of the variation in dopant concentration, an asymmetric plot, characteristic to twin plots for Gd*4d* caused due to spin splitting has been witnessed. Splitting caused by exchange interactions in the nanosystem results in ^9D initial state and ^7D final state, which were studied elaborately with a five-fold Voigt fitting [35]. Observations for the intensity ratios between these initial and final states suggest the contributions of spin polarization to the profile being greater in the case of 3% and 7% doped Eu^{3+}:Gd_2O_3 nanosystems.

Signals for the Gd–O bond were revealed from the XPS core level O*1s* spectra and are believed to be caused by the hydroxyl groups absorbed during formation of the system. Since the systems were prepared by a wet route, the occurrence of near surface oxygen species can be considered as common. A decrease in intensity of the peak corresponding to lattice oxygen is witnessed, which could be due to an increment in anomalous oxygen bonding present in the system. Apart from the hydroxyl groups revealed, the anomalous bonds that exist in the system are O–O bonding, O–OH or [Gd…O–OH] bonding which also give rise to observable peaks in the spectra [36]. Upon Eu doping, Eu–O bonds may be favored and a certain amount of Eu would occupy O centers thereby increasing chances of lattice defects. Consequently, surface oxygen defects arise because of which the anomalous bonds prevailed over natural bonds.

4.2. Likelihood of Eu^{2+} and Eu^{3+} states

Usually, the Eu $4f^6$ and Eu $4f^7$ final sate configurations are responsible for such intrinsic splitting observed in the Eu*3d* core level spectra, resulting to signals of the Eu(III) and Eu(II) states [37]. The intensity ratio is maximum for that of 3% doped EuGNP, which strikingly drops with increasing dopant concentration. This result is captivating as it allows us to highlight an important aspect in explaining the XPS spectra of Eu, relating the variation in valence of Eu at core and surface layers [37]. In general, dopant distribution into the matrix is irregular.

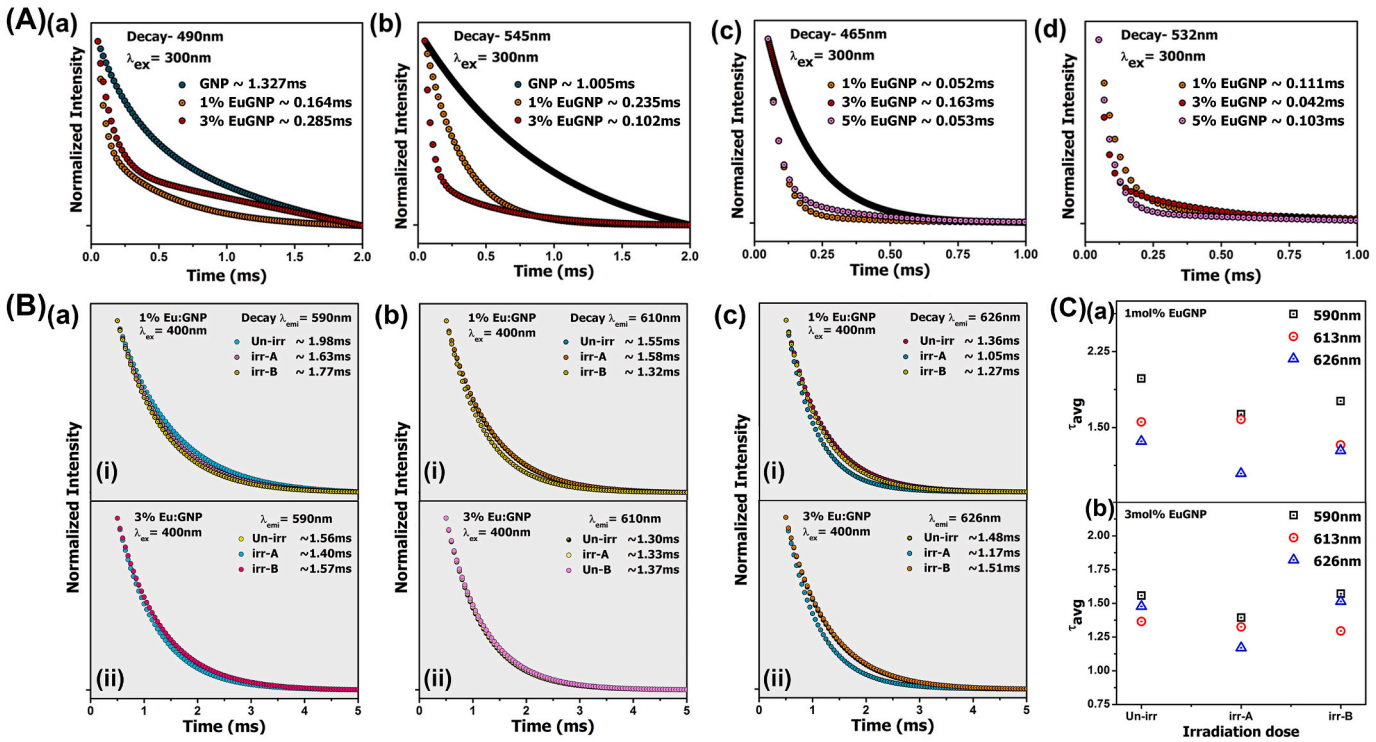

Fig. 7. TR-PL decay dynamics for various emission peaks observed in blue-green region (A)(a–d). (B)(a-c) orange-red region for (upper panel) 1%EuGNP, and (lower panel) 3% EuGNP with and without irradiation. (C) Calculated average lifetimes for the prominent transitions involved (a) 1% EuGNP, and (b) 3% EuGNP.

Comparing between the surface and core and it is generally recognized that most of the Eu^{3+} ions are present in the core. However, the scenario changes to an extensive degree in a nanosystem where the surface to volume ratio is higher. Considering the fact that a trivalent Eu always forms stronger bonds than a divalent species, the loss of bonding (dangling) in forming a surface will always be larger for the trivalent case. Thus due to a variation in the co-ordination, lower valence (i.e. Eu^{2+}) is more favored at the surfaces, while in the core the trivalent nature prevails. This is alternatively known as 'surface valence transition' and various researchers in this regard have argued that the divalent signal comes from the surface layers only [15,38]. We suspect that in case of 3% inclusion of dopant, the incorporation of Eu ions at the core reaches maximum and as the concentration is increased, more dopant ions are accommodated at the nanoscale surface regime. In conclusion, the decrement in intensity ratio could be explained assuming that the divalent signal arrives from the surface layers. Henceforward, as the concentration increases, the scope of Eu^{2+} ions to occupy the sites available in the surface layer extends [39–41].

The as-prepared samples were then subjected to optical absorption, spectroscopic investigations in order to analyze the associated carrier transitions. The transitions between the 3432 multiplets in Gd^{3+} due to reorganization of the seven *4f* electrons profoundly contribute to the energy absorption mechanisms and leads to weakly intense peaks below 300 nm in the UV–Vis absorption spectra [42]. Apart from the reorganization of Gd*4f* electrons, another possible energy absorption mechanism involving Gd matrix requires transitions between *4f* and *5d* which usually characterize high energies with peaks arising below 220 nm. Interestingly, this transition type could be realized only in the case of 1% and 5% EuGNP nanosystems in which the host excitation band is not exhibited due to the predominant peak profiles in the 270 nm region. Peaks above 300 nm characterize *f-f* transitions of Eu^{3+} ions within its $4f^6$ transitions. As the CTB requires a greater number of Eu^{3+} ions in the host for substitution of Gd^{3+} ions, the corresponding peaks were well recognized only for higher doping levels (5% and 7% doped EuGNP). Thus, Gd based matrix and Eu^{3+} ion interaction and charge transfer is revealed to be more prominent in case of low doping levels from the absorbance and reflectance profiles. This observation relating the effective interaction between the dopant and matrix ions at lower concentrations was also predicted from the XPS analysis. Reflectance profiles were utilized in determining the optical band gap of the systems as the absorbance profiles of prepared samples (off-white in appearance) are weak. Further, small changes in the optical band gap determined could be due to the quantum confinement effects in the nanosystem of reduced dimension [43]. The band gap determined from the Kumar's model enables us to comprehend the indirect transitions involved, encompassing absorption and emission of phonons [44]. Our observations indicate that the involved indirect optical transitions are suitably phonon-assisted. The effect of dopants resulting in altered optical band gap of Gd_2O_3 has also been reported earlier [45].

4.3. Manifested ED and MD transition mediated blue-green and red emission

With the aim and motive to probe and associate the electrically driven, ED and magnetically driven, MD transitions involved in Eu, a thorough analysis of photoluminescence aspects has been considered. The PL excitation spectra also revealed the CTB observed in the absorbance profiles. It is known that the Eu^{3+} ions are first excited to higher $^5D_{1,2,3}$ levels and then relaxed nonradiatively by multiphonon emission process to the emitting $^5D_0$ level [32]. Moreover, a widely accepted excitation mechanism for the RE ions displaying PL can also account for where with the incomplete inner shells, the electronic centers (deep levels positioned close to the middle of the band gap is responsible for non-radiative recombination of electrons and holes generated into the bands) formed by dopant Eu^{3+} have isoelectronic character (same overall charge and appear to be neutral with respect to the host) and part of recombination energy can be transferred to the core, thereby promoting it to an excited state [46]. The mechanism of excitation, or population of $^5D_0$ level of Eu^{3+} in Gd_2O_3 host matrix is via the energy transfer from the trap-levels (defect states of the matrix host ions, Gd^{3+})

to that of the activator ions, Eu^{3+}. In order to excite the ions to the higher levels, the system was excited at 300 nm and the emission spectra were observed in the blue-green regime. As for the undoped samples, the observed peak at ~490 nm is originated mainly due to Schottky and Frenkel defect types by virtue of thermal lattice disordering locally and as a consequence of interstitial Gd^{3+} ions. Whereas, the other peak at ~545 nm is due to the co-localization of electrons in the Stark level transitions from ^6G_J state of Gd^{3+} [14]. The host lattice can henceforth be considered as vacancy type luminescent active system.

In fact, the doped samples displayed distinctive transitions in blue-green regime. These transitions are complicated given that a large number of crystal field transitions influence these levels and are rarely reported. The observations indicate inhibition of non-radiative transitions between $^5D_1$ to $^5D_0$, typical for temperatures below 200 K, and leads to non-equilibrium back up of population in $^5D_1$ level [32]. Based on the selection rules which are strictly valid in the Russel Saunders coupling scheme, these transitions are either ED (T1, T2, T4), or MD (T3 and T5) types. We observed luminescence quenching to occur beyond the level of critical doping (~3% EuGNP). Concentration quenching is mainly due to the transfer of excitation energy from an activator to another so that the energy is lost radiationlessly [47].

In general, above bandgap excitation wavelength facilitates nearby carrier trapping site before reaching the dopant ions; hence 400 nm was also chosen as the wavelength of excitation [48]. The PL emission profiles in the red regimes were then revealed. In a compound where Eu^{3+} ion occupies no centre of symmetry at all, both ED and MD transitions are possible. The $J = 0,3,5$ level also displays J mixing with other sublevels of $J = 2,4$. Observance of forbidden T6 transition is explained by many researchers on the basis of J-mixing due to the crystal field perturbation, or mixing of low lying charge transfer states into wavefunctions of $4f^6$ configuration [49–52]. T7 is a strong MD transition observed and is largely independent of the Eu ion environment unlike T8, which is a hypersensitive transition. Not surprisingly, a nonlinear variation in PL intensity with increasing doping levels would suggest that the Eu_2O_3 phases are not formed separately [53].

Although rarely discussed, reports suggest that the intensity of the forbidden transitions can be comparable with that of T7 feature [54]. The intensity ratio decreases upon increasing doping levels representing possible alterations in site-symmetry. The single peak for T6 arises due to a non-degeneracy of the involved levels and single site as well as species [55,56]. Yet again, as predicted earlier, the origin of ~580 nm peak indicates that fraction of Eu^{3+} ions occupy C_{nv}, C_n or C_s symmetry [9]. Another important observation, as shown in Fig. 5B(a), is the broad T6 profile with FWHM ratio of T6 and T7 being highest for 3%Eu:GNP and indicates that Eu^{3+} ions occupy the $S6$ sites (while broad T8 signifies occupation in $C2$ sites) [9]. The dopants in cubic phase Gd_2O_3 are allowed to reside randomly in cation sites with either of the two symmetries- $C2$ (24 non-centrosymmetric sites) and $S6$ (8 centrosymmetric sites) [57,58]. As for Eu^{3+} ions occupying the $S6$ site, only the MD will be observed on the other hand, under $C2$ site symmetry Stark's splitting is realized [59]. Only 11% of the total emission intensity is believed to be from the excited Eu^{3+} ions that occupy the $S6$ site [60]. Our observations with both MD and ED transitions make it clear that dopant ions (Eu^{3+}) reside in both the $C2$ as well as $S6$ sites [61].

The occurrence of ED based T8 depicts that the Eu^{3+} ions are incorporated away from the centrosymmetric site (Fig. 4A(a)) [62]. The intensity ratio is found to be maximum for the highest doping concentration (7% EuGNP), but the peak is found to be sharper than that for 3% EuGNP. The ratio being as high as 9 fold to that of MD based T7 being common and discussed in earlier reports [63,64]. The T7 and T8 peak splitting with additional peak centering at ~599 nm (absent in case of 1% EuGNP) is observed along with strongly intense emission for T8 centering at ~626 nm which indicates that lower doping levels have proper cubic crystal field and the site symmetry is lowered, or altered to axial in higher doping levels [65]. Our XPS based revelations also suggested better interaction between the orbitals at lower concentrations.

An observable increase in intensity for the 7% doped EuGNP system beyond critical concentration can be elucidated considering that higher doping concentrations favor emission from $^5D_0$ level at the expense of higher excited states related transitions, and hence the T8 intensity increases. The quenching in high energy level emission could be largely favorable for lower energy emissions following multiple cross-relaxation events [66] viz.,

$$^5D_1\left(Eu^{3+}\right)+{}^7F_0\left(Eu^{3+}\right)\rightarrow{}^5D_0\left(Eu^{3+}\right)+{}^7F_3\left(Eu^{3+}\right) \quad (4)$$

It is noteworthy that non-uniform incorporation of Eu^{3+} ions throughout the lattice possibly increases with increasing concentrations which leads to Eu^{3+} cluster zones and zones barren of Eu^{3+} ions as well. Therefore, the Eu^{3+} dopants experience a variety of local environments for higher doping cases leading to different local field and symmetry induced splitting [67]. The distance between nearest neighbors (activators) also plays a decisive role in quenching. The critical distance, R_c for the critical concentration, $X_c = 3$ mol% was determined to be ~1.36 Å using Blasse's energy transfer equation given by Refs. [68,69].

$$R_C = \left(\frac{3V}{4\pi N X_c}\right)^{\frac{1}{3}}, \quad (5)$$

where, $N=32$, is the number of cations per unit cell for Gd_2O_3 and V is the unit cell volume determined using 'Powder cell for Windows®' to be ~1268.5 $Å^3$. The sudden rise in intensity for 7% EuGNP can also be explained considering a change in Coulomb interaction of dopants upon higher doping level, which allows Eu^{3+} ions to experience different crystal field leading them to occupy non-centrosymmetric sites [70].

Beyond critical concentration, most of the activators have other activators as nearest neighbors and hence the phonon spectrum and lattice constants would change, and the probability of thermal quenching varies. The nature of the concentration quenching mechanism of Eu^{3+} can be determined by analyzing intensity, (I) following Dexter theory [55,71].

$$I \propto x\left[1+\beta(x)^{\frac{s}{3}}\right]^{-1} \quad (6)$$

In Eq 6, $s = 3,6,8,10$ depends on the series of electronic multipole interaction and is a decisive factor the value of which indicates the type of interaction involved, β is a constant [72]. Here, 's' can duly be determined plotting log (I/x) vs log x on a logarithmic scale of I/x. In our study, $s/3 = 1.32$, i.e., $s = 3.96$ (Fig. 5B(d)). This value, s~3 corresponds to the exchange interaction of ions to be the prime mechanism behind the quenching. Interestingly, the effectual contribution of exchange interaction on splitting of Gd$4d$ XPS signals was profoundly observed. Overlapping of near zone ED fields of activators occur between activators and at sufficiently low concentrations only a small quanta of energy is quenched. Such an exchange interaction between ions occurs when the ions are located near one another such that there is sufficient overlap in their wavefunctions along with the coupling of spins [73,74]. To add, such an observation in red phosphor Eu^{3+}:GNP is extremely crucial not only because of fundamental reasons but also its relevance in spin injection and transport.

Since the vibronic intensity of T8 is known to be lowered at low temperatures, we also studied the PL response for the system, below room temperature conditions. Strikingly, a clear peak splitting was evident for the (ED) transitions to $^7F_2$ as the temperature was lowered. $^7F_2$ has four levels, three non-degenerate and one degenerate and speaking in terms of polarization of light, the perpendicular component leads to peak centering at ~619.3 nm (non-degenerate), component polarized along c-axis at, ~615.5 nm (degenerate) [75]. As far as the splitting of ~650 nm peak of T9 is concerned, $^7F_3$ has three non-degenerate and two doubly degenerate states. The peaks at ~650 nm have optically active components and those at ~654 nm and 656 nm are due to components perpendicular to c-axis. The peak observed at ~652 nm is due to the component parallel to c-axis [75]. The peak

around 648 nm might be due to higher state transitions [75].

4.4. Effect of γ-irradiation on lifetime aspects of phosphorescence decay

Radiation exposure has a profound effect on the optical, electrical and physical properties of materials, and to the extent which primarily depends on the doses used [76]. The degree of crystallinity and aligned orientation can be introduced at high doses of radiation. In our study, the GNP nanophosphor was first dispersed in Millipore® water and then subjected to γ-irradiation in the radiation chamber. Upon γ -ray irradiation of liquids, most of the energy is absorbed by water, so water radiolysis might take place, which results in formation of reactive species such as oxidizing hydroxyl radical (OH^-) and very powerful reducing radicals as hydrated and hydrogen atoms [14]. The interaction generates free radicals by radiolysis process which recombine, or interact with other species present in the solution and induces a change in optical property. High energetic γ-irradiation is also capable of creating and annihilating defects in chemically stable Gd_2O_3 and Fe_3O_4 systems [14,77]. The luminescence responses for both 1% and 3% doped samples as observed in the 450–550 nm range arising from higher energy level-based transitions were found to be augmented (Fig. 6A (c-g). To the best of our knowledge, no earlier report has elaborated the effects of γ -irradiation in the blue-green region. During exposure, electrons are emitted due to the Compton effect resulting by way of interaction of γ -photons with the medium. These electrons can also be accommodated in the pre-existing oxygen vacancies, resulting in formation of adequate F^+ centers leading to an enhanced luminescence, provided we do not consider energy transfer between Gd^{3+} and the F^{2+} centers [29]. Otherwise, it would result in direct pairing to the excited state with subsequent radiative transitions to ground state [29]. Newer peaks are visible after irradiation that ascribe to the defect formations due to radiation exposure. The important ED transition in this range centred at ~532 nm is found to gain intensity manifold after irradiation. As for the FWHM ratio of ED and MD transition in the red regime, we observe an irradiation dosage dependent improvement for both 1% and 3% Eu^{3+} doping levels. We can thus be ascertained that irradiation has induced creation of closely packed non-radiative trap centers which include both neutral as well as ionized vacancies. In the orange red regime, with increasing irradiation dose we observed a nonlinear variation in the intensity ratio for T8:T7. Nevertheless, for the lower dose the ratio drops but gets augmented as the dose was increased. The track interaction model (TIM) suggests localized entity as the electron-hole doubly occupied spatially correlated trap centre/luminescent center pairs [14, 78]. For lower doses, number of generated luminescent centers would be small and may not contribute to extra PL feature. We believe that at a relatively higher dose, formation of such localized entities would be greater as a result of which the distances between them tending to decline. More importantly, the contribution to extra PL intensity would increase as witnessed in our case for higher doses.

In order to obtain further insight into the species excited state dynamics, and its relevance with dose dependency, TR-PL analysis was performed. In all cases we observed that the build-up phase did not begin from zero indicating possibility of two excitation pathways to populate the $^5D_0$ level, one being via $^5D_1$ level and the other promoting ions directly into $^5D_0$ (Fig. 7) [32]. Almost all the emission peaks showed decay profiles that were mono exponential. Lifetime is reported to be 1 ms for C_2 site emission while for Eu^{3+} ions in S_6 sites the life-time increases by at least three-fold (~3–4 ms) [28,61,79]. The lowering in lifetimes, upon increasing doping concentration is attributed to an increase in non-radiative relaxation caused by the surface defects acting as quenchers [80]. In this regard, a very limited literature was devoted to determining the decay parameters of the transitions in the blue–green regime. Interestingly, a steep decrease has been realized for the lifetimes of peaks centred at ~490 nm and 545 nm, upon europium doping. These transitions are dominated over by the strong *D-F* transitions upon Eu doping, thereby changing the decay dynamics of the peaks. The lifetimes associated with MD transitions at ~590 nm, 612 nm followed similar trends at varying doping levels. The lifetimes of both strongest MD and ED transitions drop substantially upon increasing the doping levels of Eu (up to 3%). Conversely, the lifetime of ~626 nm peak was increased by 0.12 ms when the dopant concentration is increased from 1 mol% to 3 mol%. This incongruity with variation in lifetime of other peaks can be defined anticipating that this peak arises from the splitting due to crystal field. For a higher doping level the field is stronger and hence the transition has a different recombination route as compared to the other two transitions.

Irradiation based experiments induce dislocations of activator ions to interact with the defect centers and hence complex multifaceted decay dynamics is expected. The effect of irradiation can be witnessed to have equally impacted both the doping levels, where the lifetime drops for irr-A and regains its value for irr-B in case of 590 nm and 626 nm. Strikingly, as for 612 nm the lifetimes of both 1% and 3% doped samples have dropped for the irr-B case. Thus both radiation exposure and dopant concentration contribute immensely to radiative emission events in a select wavelength range.

5. Conclusions

The citrate gel route derived cubic phase Gd_2O_3 nanopowders displayed excellent bright red luminescence under UV irradiation, when doped with Eu^{3+} at varying concentrations. XRD and PL based observations suggest that Eu_2O_3 phase is not formed separately. TEM imaging allowed us to visualize the nanocrystalline feature along with the indication of amorphous surface layer due to citric acid coating. From the SAED patterns perfect periodicity could be assumed following the concentric ring-type patterns along with distinct bright spots. Noticeable reduction in the spacing between successive planes was realized due to inclusion of Eu^{3+} into the Gd_2O_3 host. Interplanar spacings determined from TEM imaging are estimated to be, ~0.28 nm, 0.29 nm and ~0.3 nm, which correlate the (400), (200) and (222) planes respectively. Following the XPS based study, the valence band maximum was determined to be ~8.4 eV. Upon Eu inclusion as dopant, peaks at ~1137 eV and ~1152 eV have been observed, being characteristic of +3 and + 2 oxidation states of Eu, respectively. This important observation of the signal from +2 oxidation state of Eu, is attributed to 'surface valence transition' involved in the system. The XPS study also suggests that for 3% doped EuGNP the interaction between the Gd-orbitals with that of the surrounding Eu is believed to be higher as compared to other cases. Spin splitting can be witnessed from the Gd*4d* spectra and contribution of spin polarization to the profile was found to be greater in case of doped system, due to sufficient overlap in the wavefunctions of Eu and Gd along with spin coupling. Such observations were not discussed for Eu doped RE oxides in earlier studies.

Concentration quenching was expected above a critical concentration of 3% EuGNP. The exchange interaction of ions can be anticipated through our analysis following Dexter's theory. The effect of overlapping of near zone ED fields of activators hence needed further investigation and consequently, discussed in detail. A rise in intensity of peaks from while observing a decrease in intensity for $^5D_1$ to ^7F levels in the case of 7% EuGNP can be elucidated citing higher doping concentrations to favor emission from $^5D_0$ level at the expense of higher excited states related transitions. Following the emission profiles in the blue-green regime, it can be established that many crystal field transitions influence these levels to follow non-radiative transitions between $^5D_1$ to $^5D_0$. Out of the various transitions via $^5D_0$-^7F_J (J = 0,1,2,3,4) in the red and far-red regime the $^5D_0$-$^7F_0$ transition, positioned at ~580 nm is a captivating observation confirming *J*-mixing due to crystal field perturbation and/or mixing of low-lying charge transfer states into wavefunctions of $4f^6$ configuration. More importantly, the peak also signifies non-degeneracy of the involved levels and single sites as well as species of the dopant ions. Thus, we conclude that the divalent signals from XPS core level spectra are due to signal consideration from non-

uniform incorporation of Eu at surface layers only.

PL profiling upon temperature variation enabled us to outline the vibronic contribution to the spectra. PL emission response of the γ-irradiated samples further elates the effect of distorted local field leading to peak splitting. Non-uniform incorporation of dopant ions leads to Eu^{3+} cluster zones and zones barren of Eu^{3+} ions leading to different local field and symmetry induced splitting. Defect formations caused by irradiation induced phenomena would result in closely spaced non-radiative trap centers including both neutral as well as ionized vacancies. Hence, indicating two possible excitation pathways to populate the $^5D_0$ level, one being via $^5D_1$ level and the other promoting ions directly into $^5D_0$. The most intense ED transition in the blue green regime at 532 nm, displayed the slowest lifetime of 0.042 ms at critical concentration of 3% doping level. Meanwhile, the most intense ED transition in the orange-red regime at ~612 nm exhibited a lifetime of 1.6 ms for 1% EuGNP, and dropped to 1.3 ms for 3% EuGNP. Upon increasing dopant concentration, the slower decay dynamics observed has been ascribed to an increase in non-radiative relaxation caused by the surface defects acting as quenchers. A comparatively more complex decay dynamics was expected and observed for irradiation-based experiments because of aggravated dislocations of activator ions generated upon irradiation, which interact with the defect centers thereafter. Occurrence of non-radiative relaxation as a consequence of surface defects acting as quenchers was also realized after radiation exposure.

CRediT author statement

Aftab Ansari: Conceptualization, Methodology, Software, Writing-Original draft preparation, Visualization. **Dambarudhar Mohanta**: Investigation, Data curation, Writing - Review & Editing, Validation **Abhijit Saha**: Resources, Project administration.

Declaration of competing interest

The authors declare that they have no known competing financial interests or personal relationships that could have appeared to influence the work reported in this paper.

Acknowledgments

The help and support received from SAIC, TU is gratefully acknowledged. We thank UGC-DAE, CSR Kolkata Centre for extending γ-irradiation facility and TR-PL spectroscopy measurements. Also, the technical assistance received from Dr. S. Kundu in acquiring TR-PL data is acknowledged. We sincerely thank NEIST, Jorhat for extending XPS facility to study our EuGNP powder samples.

Appendix A. Supplementary data

Supplementary data to this article can be found online at https://doi.org/10.1016/j.optmat.2021.111627.

References

[1] J.-L. Bridot, A.-C. Faure, S. Laurent, C. Riviere, C. Billotey, B. Hiba, M. Janier, V. Josserand, J.-L. Coll, L. Vander Elst, J. Am. Chem. Soc. 129 (2007) 5076–5084.
[2] N. Dhananjaya, H. Nagabhushana, B. Nagabhushana, R. Chakradhar, C. Shivakumara, B. Rudraswamy, Phys. B Condens. Matter 405 (2010) 3795–3799.
[3] J.Y. Park, M.J. Baek, E.S. Choi, S. Woo, J.H. Kim, T.J. Kim, J.C. Jung, K.S. Chae, Y. Chang, G.H. Lee, ACS Nano 3 (2009) 3663–3669.
[4] P.F. Smet, J. Botterman, K. Van den Eeckhout, K. Korthout, D. Poelman, Opt. Mater. 36 (2014) 1913–1919.
[5] J.M. de Carvalho, C.C.S. Pedroso, I.P. Machado, J. Hölsä, L.C.V. Rodrigues, P. Głuchowski, M. Lastusaari, H.F. Brito, J. Mater. Chem. C 6 (2018) 8897–8905.
[6] F. Clabau, X. Rocquefelte, S. Jobic, P. Deniard, M.-H. Whangbo, A. Garcia, T. Le Mercier, Chem. Mater. 17 (2005) 3904–3912.
[7] J. Xu, D. Murata, J. Ueda, B. Viana, S. Tanabe, Inorg. Chem. 57 (2018) 5194–5203.
[8] J.T. Randall, M.H.F. Wilkins, Proc. Roy. Soc. Lond. Math. Phys. Sci. 184 (1945) 365–389.
[9] K. Binnemans, C. Görller-Walrand, J. Rare Earths 14 (1996) 173.
[10] W. Carnall, G. Goodman, K. Rajnak, R. Rana, J. Chem. Phys. 90 (1989) 3443–3457.
[11] K. Binnemans, Coord. Chem. Rev. 295 (2015) 1–45.
[12] B. Qian, Z. Wang, X. Zhou, H. Zou, Y. Song, Y. Sheng, Ceram. Int. 46 (2020) 25249–25259.
[13] X. Wang, J. Xu, J. Yu, Y. Bu, J. Marques-Hueso, X. Yan, Phys. Chem. Chem. Phys. (2020).
[14] R.K. Tamrakar, K. Upadhyay, D.P. Bisen, J. Radiat. Res. Appl. Sci. 7 (2014) 526–531.
[15] S. Kumar, R. Prakash, R. Choudhary, D. Phase, Mater. Res. Bull. 70 (2015) 392–396.
[16] F. Mercier, C. Alliot, L. Bion, N. Thromat, P. Toulhoat, J. Electron. Spectrosc. Relat. Phenom. 150 (2006) 21–26.
[17] D. Barreca, A. Gasparotto, A. Milanov, E. Tondello, A. Devi, R.A. Fischer, Surf. Sci. Spectra 14 (2007) 60–67.
[18] S. Hazarika, D. Mohanta, Eur. Phys. J. Appl. Phys. 62 (2013).
[19] S. Hazarika, N. Paul, D. Mohanta, Bull. Mater. Sci. 37 (2014) 789–796.
[20] P.D.F. JCPDS-ICCD, International Center For Diffraction Data, Pennsylvania, USA, 2001.
[21] S. Tougaard, I. Chorkendorff, Phys. Rev. B 35 (1987) 6570.
[22] D. Zatsepin, V. Galakhov, M. Korotin, V. Fedorenko, E. Kurmaev, S. Bartkowski, M. Neumann, R. Berger, Phys. Rev. B 57 (1998) 4377.
[23] J.-P. Zhou, C.-L. Chai, S.-Y. Yang, Z.-K. Liu, S.-L. Song, Y.-L. Li, N.-F. Chen, J. Cryst. Growth 270 (2004) 21–29.
[24] D.A. Shirley, Phys. Rev. B 5 (1972) 4709.
[25] E.-J. Cho, S.-J. Oh, Phys. Rev. B 59 (1999) R15613.
[26] S. Mukherjee, P. Dasgupta, P.K. Jana, J. Phys. Appl. Phys. 41 (2008) 215004.
[27] V. Kumar, S.K. Sharma, T. Sharma, V. Singh, Opt. Mater. 12 (1999) 115–119.
[28] G.A. West, N.S. Clements, J. Lumin. 54 (1992) 245–248.
[29] A. Zatsepin, Y. Kuznetsova, L. Spallino, V. Pustovarov, V. Rychkov, Energy Procedia 102 (2016) 144–151.
[30] Y.C. Kang, S. Park, I. Lenggoro, K. Okuyama, Journal of Physics and Chemistry of Solids 60 (1999) 379–384.
[31] J.-C.G. Bünzli, S.V. Eliseeva, Basics of Lanthanide Photophysics, Lanthanide Luminescence, Springer, 2010, pp. 1–45.
[32] A. Singh, K. O'Donnell, P. Edwards, D. Cameron, K. Lorenz, M. Kappers, M. Boćkowski, M. Yamaga, R. Prakash, Appl. Phys. Lett. 111 (2017) 241105.
[33] H. Konno, X-ray Photoelectron Spectroscopy, Materials Science and Engineering of Carbon, Elsevier, 2016, pp. 153–171.
[34] S.L. Mekuria, T.A. Debele, H.-C. Tsai, ACS Appl. Mater. Interfaces 9 (2017) 6782–6795.
[35] A. Molle, C. Wiemer, M.N.K. Bhuiyan, G. Tallarida, M. Fanciulli, G. Pavia, Appl. Phys. Lett. 90 (2007) 193511.
[36] S. Majeed, S. Shivashankar, J. Mater. Chem. B 2 (2014) 5585–5593.
[37] W.-D. Schneider, C. Laubschat, I. Nowik, G. Kaindl, Phys. Rev. B 24 (1981) 5422.
[38] B. Johansson, Phys. Rev. B 19 (1979) 6615.
[39] C. Battistoni, G. Mattogno, E. Paparazzo, Surf. Interface Anal. 7 (1985) 117–121.
[40] C. Wagner, Surf. Interface Anal. 6 (1984) 90–91.
[41] M. Seah, Surf. Interface Anal. 1 (1979) 86–90.
[42] J.-C.G. Bünzli, S. Comby, A.-S. Chauvin, C.D. Vandevyver, J. Rare Earths 25 (2007) 257–274.
[43] B. Mercier, G. Ledoux, C. Dujardin, D. Nicolas, B. Masenelli, P. Melinon, G. Bergeret, J. Chem. Phys. 126 (2007) 44507.
[44] M. Wakaki, T. Shibuya, K. Kudo, Physical Properties and Data of Optical Materials, CRC press, 2018.
[45] Y.A. Kuznetsova, A. Zatsepin, Optical properties and energy parameters of Gd2O3 and Gd2O3: Er nanoparticles, J. Phys.: Conf. Ser (2017) 62001.
[46] M. Forcales, M. Klik, N. Vinh, I. Bradley, J.R. Wells, T. Gregorkiewicz, J. Lumin. 94 (2001) 243–248.
[47] D.L. Dexter, J.H. Schulman, J. Chem. Phys. 22 (1954) 1063–1070.
[48] K. Takahei, A. Taguchi, H. Nakagome, K. Uwai, P. Whitney, J. Appl. Phys. 66 (1989) 4941–4945.
[49] X. Chen, G. Liu, J. Solid State Chem. 178 (2005) 419–428.
[50] P. Porcher, P. Caro, J. Lumin. 21 (1980) 207–216.
[51] M. Tanaka, G. Nishimura, T. Kushida, Phys. Rev. B 49 (1994) 16917.
[52] O. Malta, Mol. Phys. 42 (1981) 65–72.
[53] K. Riwotzki, M. Haase, J. Phys. Chem. B 102 (1998) 10129–10135.
[54] A.O. Wright, M.D. Seltzer, J.B. Gruber, B.H. Chai, J. Appl. Phys. 78 (1995) 2456–2467.
[55] J.-C.G. Bünzli, Lanthanide Luminescence: from a Mystery to Rationalization, Understanding, and Applications, Handbook on the Physics and Chemistry of Rare Earths, Elsevier, 2016, pp. 141–176.
[56] W.D. Horrocks, D.R. Sudnick, Science 206 (1979) 1194–1196.
[57] E.R. Smith, J.B. Gruber, P. Wellenius, J.F. Muth, H.O. Everitt, Phys. Status Solidi 247 (2010) 1807–1813.
[58] A.G. Macedo, R.A. Ferreira, D. Ananias, M.S. Reis, V.S. Amaral, L.D. Carlos, J. Rocha, Adv. Funct. Mater. 20 (2010) 624–634.
[59] G.S.R. Raju, E. Pavitra, J.S. Yu, Dalton Trans. 42 (2013) 11400–11410.
[60] M. Buijs, A. Meyerink, G. Blasse, J. Lumin. 37 (1987) 9–20.
[61] A. Garcıa-Murillo, C. Le Luyer, C. Dujardin, T. Martin, C. Garapon, C. Pedrini, J. Mugnier, Nucl. Instrum. Methods Phys. Res. Sect. A Accel. Spectrom. Detect. Assoc. Equip. 486 (2002) 181–185.
[62] G. Blasse, A. Bril, W. Nieuwpoort, J. Phys. Chem. Solid. 27 (1966) 1587–1592.
[63] K. Binnemans, D. Moors, J. Mater. Chem. 12 (2002) 3374–3376.
[64] J.-C.G. Bünzli, E. Moret, V. Foiret, K.J. Schenk, W. Mingzhao, J. Linpei, J. Alloys Compd. 207 (1994) 107–111.

[65] K. O'Donnell, P. Edwards, M. Yamaga, K. Lorenz, M. Kappers, M. Boćkowski, Appl. Phys. Lett. 108 (2016) 22102.
[66] B.-S. Tsai, Y.-H. Chang, Y.-C. Chen, J. Mater. Res. 19 (2004) 1504–1508.
[67] M. Pang, J. Lin, M. Yu, J. Solid State Chem. 177 (2004) 2237–2241.
[68] G. Blasse, Philips Res. Rep. 24 (1969) 131.
[69] M. Pang, J. Lin, J. Fu, R. Xing, C. Luo, Y. Han, Opt. Mater. 23 (2003) 547–558.
[70] T.-H. Fang, Y.-J. Hsiao, Y.-S. Chang, Y.-H. Chang, Mater. Chem. Phys. 100 (2006) 418–422.
[71] D.L. Dexter, J. Chem. Phys. 21 (1953) 836–850.
[72] L. Van Uitert, J. Electrochem. Soc. 114 (1967) 1048–1053.
[73] R. Birgeneau, M. Hutchings, W. Wolf, Phys. Rev. Lett. 17 (1966) 308.
[74] D. Rao, M. Tovar, S. Oseroff, D. Vier, S. Schultz, J. Thompson, S.-W. Cheong, Z. Fisk, Phys. Rev. B 38 (1988) 8920.
[75] C. Brecher, H. Samelson, A. Lempicki, R. Riley, T. Peters, Phys. Rev. 155 (1967) 178.
[76] R. Clough, Nucl. Instrum. Methods Phys. Res. Sect. B Beam Interact. Mater. Atoms 185 (2001) 8–33.
[77] M. Devi, D. Mohanta, A. Saha, Indian J. Phys. 89 (2015) 115–121.
[78] Y.S. Horowitz, O. Avila, M. Rodriguez-Villafuerte, Nuclr Instrum. Meth.B 184 (2001) 85–112.
[79] L. Ozawa, H. Forest, P. Jaffe, G. Ban, J. Electrochem. Soc. 118 (1971) 482–486.
[80] G. Blasse, J. Solid State Chem. 14 (1975) 181–184.

Physica E 143 (2022) 115357

Contents lists available at ScienceDirect

Physica E: Low-dimensional Systems and Nanostructures

journal homepage: www.elsevier.com/locate/physe

Structural and XPS studies of polyhedral europium doped gadolinium orthovanadate (Eu^{3+}:$GdVO_4$) nanocatalyst for augmented photodegradation against *Congo-red*

Aftab Ansari, D. Mohanta *

Nanoscience and Soft Matter Laboratory, Department of Physics, Tezpur University, PO: Napaam, Tezpur, 784028, Assam, India

ARTICLE INFO

PACS:
Nos. 33.60.Fy
61.46.+w
61.50.Ks
68.37.Lp

Keywords:
Nanoscale
Rare earth
Doping
X-ray photoelectron spectroscopy
Photocatalytic
Solid state synthesis

ABSTRACT

The present work demonstrates structural, valence band mapping (VBM) and photocatalytic activity of Eu^{3+} doped orthovanadate ($GdVO_4$) nanosystem against an azo-dye, *Congo-red*. As evident from x-ray diffraction (XRD) studies, the nanosystem synthesized via a solid-state cum sintering route exhibited zircon-type crystal structure with space group $I\,4_1/amd$. Imaging through transmission electron microscopy (TEM) has revealed polyhedral nanoaggregates, which are of polycrystalline nature. Introduction of Eu^{3+} into the host $GdVO_4$ was substantiated from the energy dispersive x-ray (EDX) spectra, x-ray photoelectron spectra (XPS) and considering inclusion of dopants to binding energy correspondence in the VBM spectra. In this study, the azo-dye *Congo-red* has been opted as the target dye for photodegradation. After UV light illumination, Eu^{3+}:$GdVO_4$ nano-catalyst could degrade the organic dye quite effeciently (up to 91.8%), and offering a rate constant nearly doubled as compared with its undoped counterpart. The dopant ions being associated with the new localized states enabling promotion of additional photoexcited carriers taking advantage of the incident UV exposure. Structural, XPS, and optical studies of the rare-earth vanadate nano-systems as well as their photocatalytic activity would provide new insights to resolve existing concerns, *viz.*, removal of organic contaminants, and environmentally harmful dyes and to carry multi-functional scope for industrial relevance. Moreover, such systems may have immense potential for displaying select emission response as well as photocatalysis even though both processes are mediated via opposite effects.

1. Introduction

Investigation of ABO_3 and ABO_4-type inorganic nanomaterials has aroused growing interest because of their peculiar crystal structure and enriched physico-chemical properties including photoluminescence, photocatalysis, energy storage, as well as magnetically and electrically driven performances [1–3]. Concerning the luminescent materials, for instance, the microstructure of the host is believed to have a crucial impact on the desired property. One of the interesting phenomena associated with the declining of crystallite sizes is the transformation of the local symmetry essential for tailoring properties. To be specific, such conditions are invariably realized in rare earth (RE) sesquioxides, or perovskites. Incorporation of another RE ion by substitution could also influence the local symmetry, to a great extent. Characteristic properties of gadolinium orthovanadate ($GdVO_4$) with lanthanide ions as the dopant were first introduced by Zaguniennyi *et al.* in 1992 [4]. Compared to Eu^{3+}:YVO_4 system, Eu^{3+}:$GdVO_4$ gives a better temperature dependent luminescence feature with augmented intensity at higher temperatures and thus can be a good candidate in high temperature applications [5]. In fact, $GdVO_4$ represents a model zircon-type compound that resembles the structure of many commonly found zircon-type lanthanide orthovanadates ($LnVO_4$), an excellent host of luminescent agents and with a wide variety of applications including phosphors, scintillators, lasers, and amplifiers for fiber optic communication etc [6,7]. For instance, europium doped, gadolinium orthovanadate (Eu^{3+}:$GdVO_4$) system is an excellent red emitter with specific advantages and interest [8]. Amongst different Gd- based luminescent compounds, $GdVO_4$ is of special interest as an advanced optical material because the excitation of the cationic Ln dopants through an energy transfer from the vanadate anion is much more efficient than the direct excitation of the Ln electronic levels. Consequently, the immensely pronounced luminescence response has great relevance in the fields,

* Corresponding author.
E-mail address: best@tezu.ernet.in (D. Mohanta).

https://doi.org/10.1016/j.physe.2022.115357
Received 18 January 2022; Received in revised form 2 June 2022; Accepted 7 June 2022
Available online 9 June 2022

such as cathode ray tubes, fluorescent lamps, X-ray detectors etc [9,10].

Much effort in the development of newer methods/techniques has been encouraged in recent years for tackling environmental remediation of pollutants released through industrial plants and human activity [11]. To be mentioned, highly toxic and carcinogenic azo dyes constitute ~50–70% of all organic dyes used in textile based industries, plants and mills [11,12]. Following an attempt to degrade them, these dyes form harmful byproducts via processes, such as oxidation, hydrolysis, or other regular chemical reactions, leading to secondary problems [13]. It was known that *Congo red* (CR), the first anionic synthetic azo dye with two azo chromophores has a complex aromatic structure and is relatively more stable than other dyes. A great deal of reports can be found in the literature that describe numerous techniques being applied for degradation of azo dyes, including-ion exchange, membrane separation, or nano filtration, usage of activated carbon, irradiation, electro kinetic chemical coagulation/flocculation, electrochemical destruction, ozonation and photochemical degradation [14–22]. Nevertheless, most of the afore-mentioned conventional techniques for photocatalysis are economically not viable as they demand high-end technological interventions, and suffer from severe disadvantages such as production of sludge, and formation of unwanted byproducts [16]. In this regard, potential use of nano-catalysts is worth mentioning which could display efficient catalytic properties in water and waste-water treatment [23], and also splitting of water [24,25].

Theoretically, $GdVO_4$ exhibits the desired position of the optical band edges (with typical band gap, E_g= 3.5-3.7 eV) thereby promising a potential photocatalytic agent with a greater ability to generate hydrogen from water, or water/alcohol solutions via photoexcited reactions via visible light and UV light exposure [26,27]. Photocatalytic behavior of metal-oxide nanosystem is well defined but only a limited number of reports are available that deal with photocatalytic activity of $ReVO_4$ nanosystem [28–31]. A superior photocatalysis of azo based dyes has been speculated recognizing that the $GdVO_4$ nanosystem comes with an excellent capability to generate hydrogen from water [27,32]. Reports can be found in literature that deal with possible enhancement of photocatalytic activity of a nanosystem following inclusion of metal ions as dopants [33]. RE ions as dopants have also shown to empower the activity against azo dyes under visible light [34]. To be mentioned, effect of europium doping on the photocatalytic behavior of AVO_4 systems has been evaluated earlier and the observed augmentation in photocatalytic activity was ascribed to the effective charge separation of electron(*e*)–hole(*h*) pairs [35]. It can thus be ensured that incorporation of suitable RE ions into $REVO_4$ hosts could enhance the photocatalytic activity at large.

Various reports could be found in literature highlighting detailed protocols for preparation of RE doped RE-vanadate systems following solid-state reactions [36–38]. The present work highlights detailing of structural, optical and X-ray photoelectron spectroscopy (XPS) studies of Eu^{3+}: $GdVO_4$ nanoscale systems, derived through solid state cum sintering route. Moreover, a comparative account of the photocatalytic activity is discussed as regards performance of the nano-catalyst, emphasizing the influence of Eu^{3+} against the target azo dye under study.

2. Experimental

2.1. Solid-state derived $GdVO_4$ nanosystems

First, for solid state synthesis, gadolinium oxide (Gd_2O_3, CDH, ~99.9% pure) is mixed with equimolar content of vanadium pentoxide (V_2O_5, CDH, ~99% pure) and grounded homogeneously for 30 min in a mortar. The finely grounded mixture was placed in an alumina crucible and subjected to a tube furnace for nearly, 10 h and at a temperature of 1200 °C [37]. The as-received samples collected at room temperature were washed several times with deionized water and ethanol to yield the desired nanopowder product. In order to obtain the doped nanosystem, we introduced appropriate molar fractions of Eu_2O_3 during the grounding step. Accordingly, the undoped $GdVO_4$ (GdV), and 1%, 3%, 5% and 7% Eu^{3+}:$GdVO_4$ (EuGdV) systems were derived from the reaction mixture.

2.2. Physical techniques employed

Rigaku mini-Flex X-ray diffractometer (XRD) equipped with CuK_α radiation (λ = 1.54 Å) and offering data acquisition in the range of Bragg's angle (2θ) ~ 20–60° with a step size of 0.05°, was utilized in order to reveal structural characterization of the as-derived samples. The morphological characteristics were examined on a transmission electron microscope (TEM) working at an accelerating voltage of 200 kV (Tecnai G2 20 S-Twin FEI, USA). The XPS based analysis was also carried out with the help of a Thermo-Scientific ESCALAB Xi^+ spectrometer having a monochromatic *Al* K_α source of X-rays (1486.6 eV) and a spherical energy analyzer that operates in the constant analyzer energy (CAE) mode employing appropriate electromagnetic lenses. The optical absorption/reflectance studies were conducted on a Lambda 365 spectrophotometer (PerkinElmer®, USA).

2.3. Electrochemical impedance spectroscopy (EIS)

The electrochemical measurements were carried out at room temperature in a configuration of three electrode system (counter electrode, working electrode and reference electrode) for electrochemical impedance spectroscopy (EIS) studies. It was executed in an AUTO FRA modular GAMRY potentiostat/galvanostat in a 1 M KCl solution as the electrolyte, and in the frequency range of 100 kHz–1 Hz at a 0V DC bias potential. Typically, a thick slurry was drop casted on the indium tin oxide (ITO) coated glass slide which offered an electro-active area of dimension 1 × 0.5 cm^2 followed by adequate oven drying at a temperature of 60 °C.

2.4. Photocatalytic studies

To determine the photocatalytic activity of GdV and EuGdV towards degradation of CR, a stock dye solution was prepared with 1 mg of CR added to 200 ml of deionized (DI) water. The nanocatalyst was introduced into the solution suitably and the UV–Vis absorbance spectra were recorded at regular intervals and up to 3 h. For a better comparison of the effect of Eu^{3+} dopants in the enhancement of the photocatalytic activity, the amount of photocatalysts i.e., GdV and 3% EuGdV were kept same for both the studies. To be specific, stock photocatalyst solution was prepared adding 20 mg of catalyst in 1.5 ml DI water. The 400 μl of photocatalyst was added from the stock photocatalyst solution into 100 ml of CR stock dye solution. The resultant suspension was sonicated for 5 min and then stirred in the dark for 30–45 min to ensure the adsorption/desorption equilibrium on the nano-photocatalyst surface prior to irradiation. Normal UV, or visible light exposure with separation between the light source and the reaction mixture about 15 cm was employed in the present study. For visual assessment, digital photographs were captured as regards photodegradation activity. The nature of progressive dye degradation can be quantified using the following equation:

$$\%\ \ Dye\ degradation = \left(\frac{C_0 - C_t}{C_0}\right) \times 100$$

where, C_0 and C_t represent respective concentrations of the dye solution before and after irradiation as determined from the standard absorption curves of known concentrations of CR dye (Fig. S1).

2.5. Inductively coupled plasma-optical emission spectrometry (ICP-OES)

Microwave assisted acid digestion of both undoped (GdV) and doped

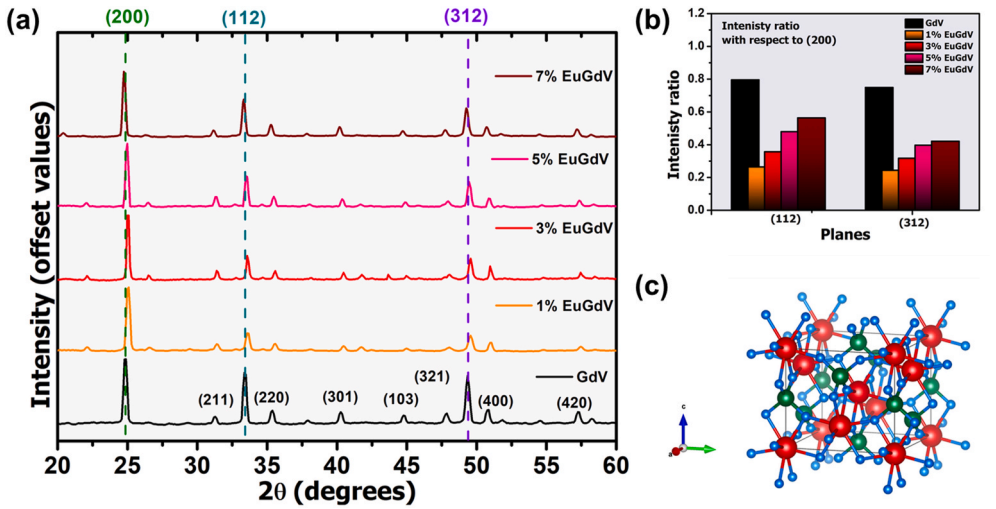

Fig. 1. (a) Comparative XRD patterns for as-prepared nanosystems in the range of Bragg's angle 20-60°. (b) Relative intensity of the (112) and (312) peaks as compared with respect to intensity of most intense (200) peak. (c) Illustrative ball and stick figure symbolizing crystal structure of tetragonal $GdVO_4$ with space group $I\,4_1/amd$ and axial ratio ~ 0.87 Å, obtained using Vesta®. The red, green and blue balls denote Gd, V and O atoms; respectively (colour online).

(3% EuGdV) samples was performed following standard U.S. EPA method [39]. For microwave digestion, 1 mg of the sample was taken in a vessel with 9 ml HNO_3 (for digestion of Gd and Eu) and 1 ml HCl (for V digestion). The temperature was raised to ~175 °C within 5.5 min and then incubated for 4.5 min. Following this, centrifugation at 2500 rpm was performed for nearly 10 min. Before the experimentation, the samples were further diluted up to 50 ml.

Microwave digested samples were produced to Thermo ScientificTM iCAPTM 7600 with simultaneous echelle type, 52.91 grooves/mm ruled grating, 383 mm effective length, and 9.5° UV fused silica cross dispersion prism. ICP-OES data of the investigated nanosystems were compared to ensure stoichiometry of the Eu as dopant.

3. Results and discussion

3.1. Crystal structure and microscopic imaging

The XRD patterns of as-prepared $GdVO_4$ samples are shown in Fig. 1 (a) which essentially characterize tetragonal zircon-type crystal structure, with space group $I4_1/amd$ (JCPDS 86–0996) [40–43]. Earlier, $REVO_4$ was reported to crystallize in two different phases: zircon and monazite-types [42]. Among these, zircon ($ZrSiO_4$)-type tetragonal crystal system is the most studied crystal phase where the RE^{3+} ions occupy single coordination environment with D_{2d} symmetry [44,45]. In contrast, the monazite ($CePO_4$)-type monoclinic structure (e.g., *P21/n*) is rarely discussed in literature [45,46]. The diffractograms of 1%, 3%, 5% and 7% EuGdV also offer similar patterns with varied intensity but without introduction of any extra phase and indicating high crystallinity of the products (Fig. 1(a)). The lattice constants were calculated to be a = 7.18 Å and c = 6.31 Å, and the determined axial ratio (c/a) is 0.87 corresponding to that of pure tetragonal $GdVO_4$ [17]. The typical unit cell volume (V) of GdV was calculated to be 325.29 $Å^3$ using *Vesta*®.

The average crystallite size 'd_{DS}' was calculated using Debye–-Scherrer relation (eq. (1)) and was found to be in the range ~25–38 nm. The estimated size is comparatively smaller than the reported ones, ~50–90 nm obtained for the calcination temperature beyond 900 °C while with the dopant concentration was below 10% [8]. The microstrain and crystallite size were also calculated using popular Williamson-Hull plot 'd_{WH}' as well (Figure S2), following Eq. (2) below.

$$d_{DS} = \frac{0.9\lambda}{\beta cos\theta} \tag{1}$$

$$\beta \cos\theta = \frac{0.9\lambda}{d_{WH}} + 4\varepsilon \sin\theta \tag{2}$$

In both the equations, 'β' is the full width at half maxima (FWHM) in radians, '2θ' is the diffraction angle in degrees and 'λ' is the wavelength (1.543 Å) of the X-rays employed. Again, the crystallite sizes were determined to be in the range of 25–48 nm, similar to our observations made using Scherer's equation. The typical microstrain, ε was found to be of the order of 10^{-4} in all the cases with a negative slope in case of undoped GdV system only. A comparison as regards increment in the intensities of (112) and (312) peaks relative to (200) peak with increasing dopant level can be found in Fig. 1(b). Apparently this implies a figurative effect of change in preferred orientation of crystallites upon inclusion of a dopant into the nanosystem. The representative crystal structure of $GdVO_4$ obtained through Vesta® is depicted in Fig. 1 (c). To acquire a better understanding of the crystal structure relevant to related orientations, the illustrations were refigured for the major projection and upward vector along the normal to [200], [112] and [312] and shown in Figure S2 (B) (a-c), as the case may be.

It was known that the orthovandate structure is composed of VO_4 tetrahedrons and GdO_8 polyhedrons. It is the central V^{5+} ion which forms a VO_4 tetrahedron with the nearest four oxygen ligands in which the O-V-O angles differ slightly (108.19° and 110.18°) from those of a regular tetrahedron as predicted using *Vesta*®. Meanwhile, the host Gd^{3+} forms a bis-disphenoid with eight nearest oxygen ligands, revealing two different bond lengths of Gd–O leading to a highly asymmetric environment on Gd^{3+} as such [37,47]. In a regular Eu^{3+}: $GdVO_4$ lattice, dopant Eu^{3+} replaces host Gd^{3+} with a D_{2d} symmetry and occupies a 4a site of symmetry -4*m*2. The GdO_8 dodecahedra with VO_4 forms chains extended along the *c*-axis, while in the *ab* plane GdO_8 dodecahedra cages are linked with four adjacent VO_4 at corners alternatingly such that two are positioned along [100], and the remaining along [010] directions [42]. The Gd–O bond distance depends on the type of oxygen to which the Gd^{3+} ion is attached *viz.*, 2.4 Å (corner) and 2.6 Å (edge) [48]. The absence of impurity phases and a very small shift of reflections compared to the reflection positions of pure $GdVO_4$ indicate that the dopant ions are adequately incorporated into the $GdVO_4$ host lattice.

Furthermore, % porosity of the photocatalysts were also calculated using the formula stated below [49,50]:

$$\%\ porosity = \left[1 - \frac{\rho_b}{\rho_x}\right] \times 100 \tag{3}$$

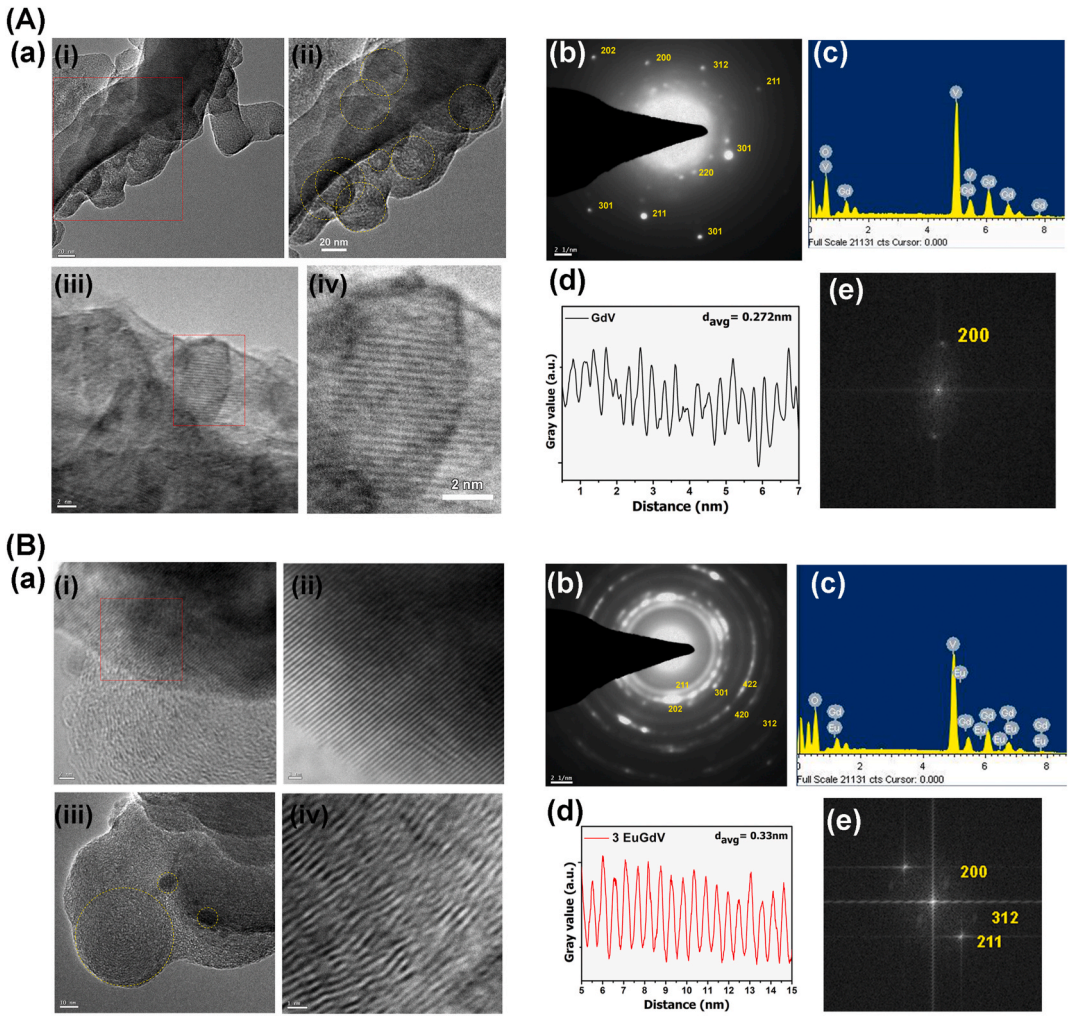

Fig. 2. TEM images (a)(i-iv) for (A) GdV, and (B) 3% EuGdV nanosystems. (b) SAED pattern with characteristic bright spots observed and indexed. The EDX spectra are shown in (c) whereas HR-TEM images revealing lattice fringe patterns are shown in (a) (iv), corresponding gray value profile over a segment are shown in (d), and Fast Fourier Transform (FFT) of the same can be seen at (e).

In eq. (3), ρ_b and ρ_x are bulk density and x-ray density; respectively. Where, ρ_x can be calculated according to equation [49,51],

$$\rho_x = \frac{ZM}{NV}. \tag{4}$$

Here, Z is the number of atoms per unit cell, M is the molecular weight, N denotes the Avogadro's number while V represents volume of the unit cell. The X-ray density decreased to some extent, from 5.558 to 5.554 g/cm^3 upon 7 mol % Eu doping. The declining in the x-ray density upon increasing concentration of dopant can be ascribed to a lighter molecular weight of Eu^{3+} (151.96 a.m.u) as compared to Gd^{3+} (157.25 a.m.u.) [52]. The porosity thus estimated using eqs. (3) and (4) are found to be 4.64%, 4.62%, 4.58%, 4.54%, 4.50% for GdV, 1% EuGdV, 3% EuGdV, 5% EuGdV and 7% EuGdV; respectively. As discussed earlier, Eu^{3+} ions preferably substitute Gd^{3+} host ions. Further addition of Eu^{3+} in the $GdVO_4$ host thus lowers the porosity of the system under study.

Morphological studies of GdV and EuGdV were made using TEM imaging as shown in Fig. 2 (A) (a) (i-ii), which reveals clumps of nearly spherical $GdVO_4$ nanoparticles being present in a sheet-like base. Our observations are analogous to previous reports on microscopic imaging of solid state derived $GdVO_4$, which display crystalline, polyhedral and slightly agglomerated bunches of smaller particles [26,38,41,42,53]. High sintering temperatures, beyond 1000 °C must be the chief reason behind agglomeration and clustering of smaller particles [38]. Fig. 2(B) (a)(i-ii) shows TEM images for 3% EuGdV which also indicate similar morphological feature as that for GdV case. The selected area electron diffraction patterns (SAED) are shown in Figure (A), (B)–(b), which revealed scattered bright spots around the diffused ring pattern in case of GdV and diffused, yet prominent rings in case of 3% EuGdV confirming polycrystalline nature of the specimens. With an oriented crystallographic axis of the system, the planes responsible for the occurrence of the spots are designated accordingly upon calculating the radius of the spots/rings using *Image J*®. HR-TEM images revealing lattice fringes of the respective samples are Fig. 2 (A), and (B), (a)(b), (iii-iv). The *d*-spacing were calculated from the plot profiles generated using *Image J*® displayed in Fig. 2 (A, B)- (d), and were determined to be 0.27 nm and 0.33 nm for GdV and 3% EuGdV; respectively. To be mentioned, these *d*-spacings belonging to the respective planes of (200) and (312), determined using *Vesta*® [JCPDS 86–0996] [43], and designated in FFT images, shown in Fig. 2(A) and (B), (a)(b)- (e). The indices observed are in good agreement with the planes outlined in the XRD analysis. In the energy dispersive X-ray spectra (EDX) based elemental analysis of the specimens, characteristic signals arising from all expected constituents corresponding to different binding energies can be easily traced. Fig. 2 (A)(c), illustrates the EDX spectrum of GdV system indicating presence of Gd, V and O; while introduction of newer signals for Eu can be realized in case of 3% EuGdV as shown in Fig. 2 (B)(c). The EDX line traces suggest that Eu^{3+} was successfully incorporated into the host crystallites substantiating the discussion on XRD based analysis.

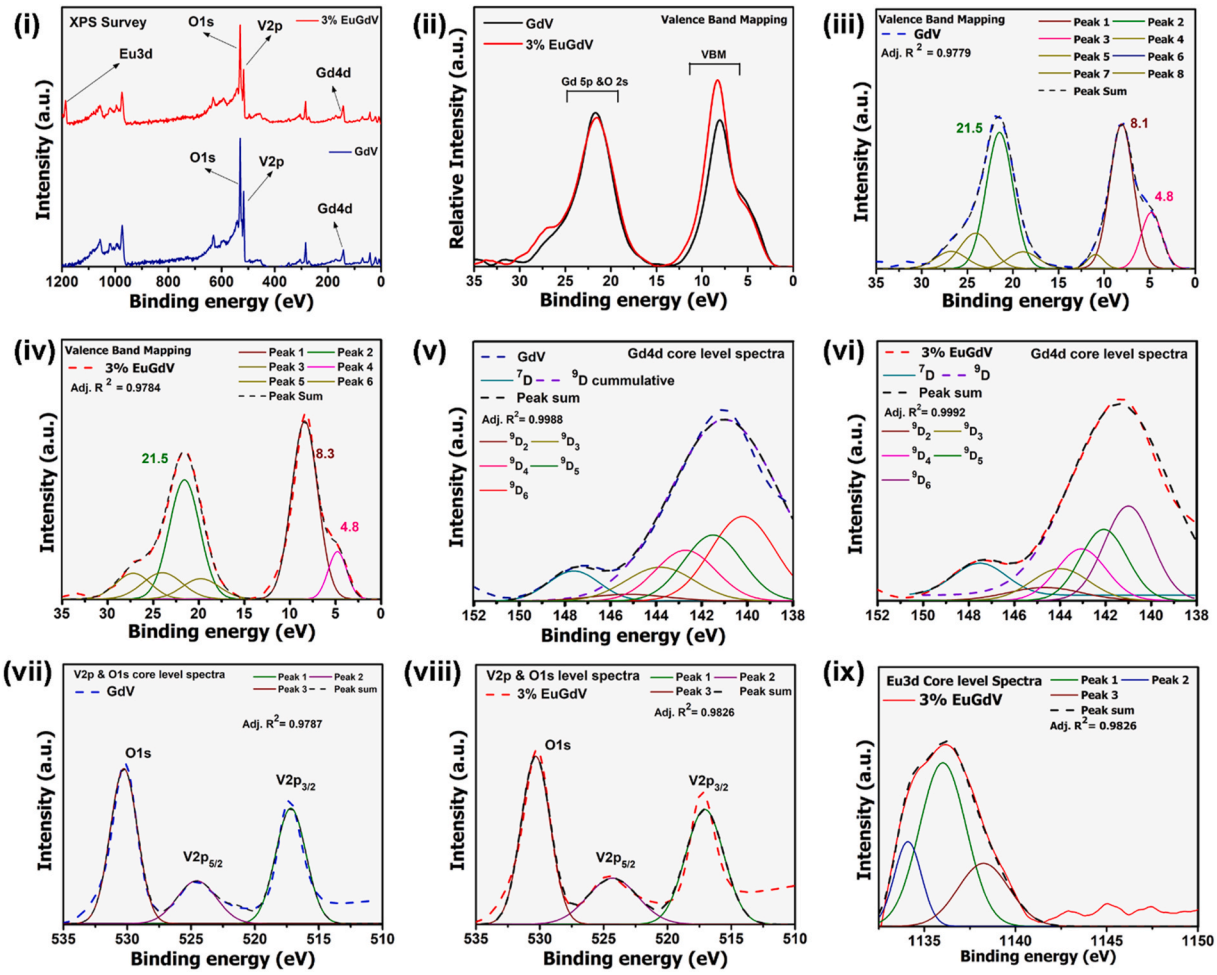

Fig. 3. (i) XPS survey of GdV and 3% EuGdV shown with the comparative VBM displayed in (ii). The deconvoluted VBM is displayed in (iii) GdV and (iv) 3% EuGdV nanosystems. The CLS for the prepared samples for (v, vi) Gd4*d*, (vii, viii) V2*p* & O1*s* (ix) Eu3*d* respectively.

3.2. XPS survey and valence band mapping (VBM) spectra

XPS analysis assists us to corroborate surface revelations of nanomaterials with regard to oxidation states of the host and dopant ions present. As only limited number of reports are available concerning XPS studies of the RE-vanadate based nanosystem, here we plan to introduce valuable quantitative information emphasizing valence band mapping spectra of the Eu^{3+}:$GdVO_4$ nanosystem.

Following the identification of crystal structure of the as-prepared nanoscale sample and confirmation of presence of Eu as a dopant into the matrix, XPS survey was conducted to analyze the elemental oxidation states and to exploit the valence band mapping of the system. Fig. 3 (i) signifies the XPS survey conducted on GdV and 3% EuGdV. The background for the XPS survey was corrected according to the well-known Tougaard rule [54]. The important revelations in the survey were signal determination of Gd4*d*, V2*p* and O1*s* orbitals. Peak centering at ~529.6 eV, agrees with the characteristic +3 oxidation state of Gd [55]. For 3% EuGdV, a weak peak at ~1137 eV has been witnessed, characteristic of +3 oxidation state of Eu offering added indication towards effective doping of Eu^{3+} in the $GdVO_4$ lattice [56,57]. Not surprisingly, other prominent lines observed in the spectrum at 1013, 999, 978 eV etc. corresponded to typical Auger lines.

Usually O2*p* partial states, Gd–O bonds, and Gd4*f* are determined in the range of 3–11 eV in the VBM spectra, shown in Fig. 3 (ii) [58]. We observed that the valence band maximum is situated at ~8.06 eV [58]. The signal was attributed, in general, to Gd4*f* and interestingly upon 3% Eu inclusion, the VBM maximum got shifted to ~8.34 eV. It is noteworthy that in between ~17 and 20 eV, peaks due to O^{2-} (point defects) are observed, and in our case, they were found to be very weak. In the 18–24 eV range, however, the Gd5*p*-O2*s* overlap peak is apparently visible at ~23 eV [58]. We evaluated the intensity and FWHM ratios to obtain a fair assessment of the effect of Eu incorporation, involving the various oxidation states. The intensity ratio of signals for Gd4*f* and Gd5*p*-O2*s* overlap has increased from ~1.1 for GdV to ~1.5 after introduction of Eu^{3+}.

It was known that the large electrostatic interactions between Gd4*d* (holes) and Gd4*f* (electrons) lead to a multifaceted multiplet structure for Gd4*d* core level spectra (CLS) and was so observed in Fig. 3 (v, vi) [58]. The plot displays a characteristic Gd4*d* doublet attributed to spin splitting by exchange interactions. The twin peaks were studied elaborately with a five-fold Voigt fitting and consequently, ^9D initial and ^7D final ionic states were analyzed [59,60]. The effect of dopant was seemingly minimal and thus suggests that incorporation of Eu^{3+} into the vanadate matrix does not interfere with the Gd4*d* states. A lower concentration of dopant ions in comparison to the most abundant host ones might be the sole reason behind such a situation.

In XPS spectrum of V2*p* as can be found in Fig. 3(i), binding energy of $V2p_{3/2}$ and $V2p_{5/2}$ as positioned at 517.1 and 525 eV were corresponding to +5 oxidation state of V [61]. Upon deconvolution (Fig. 3 (vii, viii)) we did not observe any multiplet splitting which is obvious as V^{+5} does not have any unpaired electrons [62]. A symmetrical peak fit suggests that V^{+5} has not undergone any decaying and other species viz. V^{+4}, V^{+3} etc. are absent in the nanosystem. Furthermore, the CLS reveals O1*s* peak at ~530.3 eV and are attributed to V–O and Gd–O bonds in the

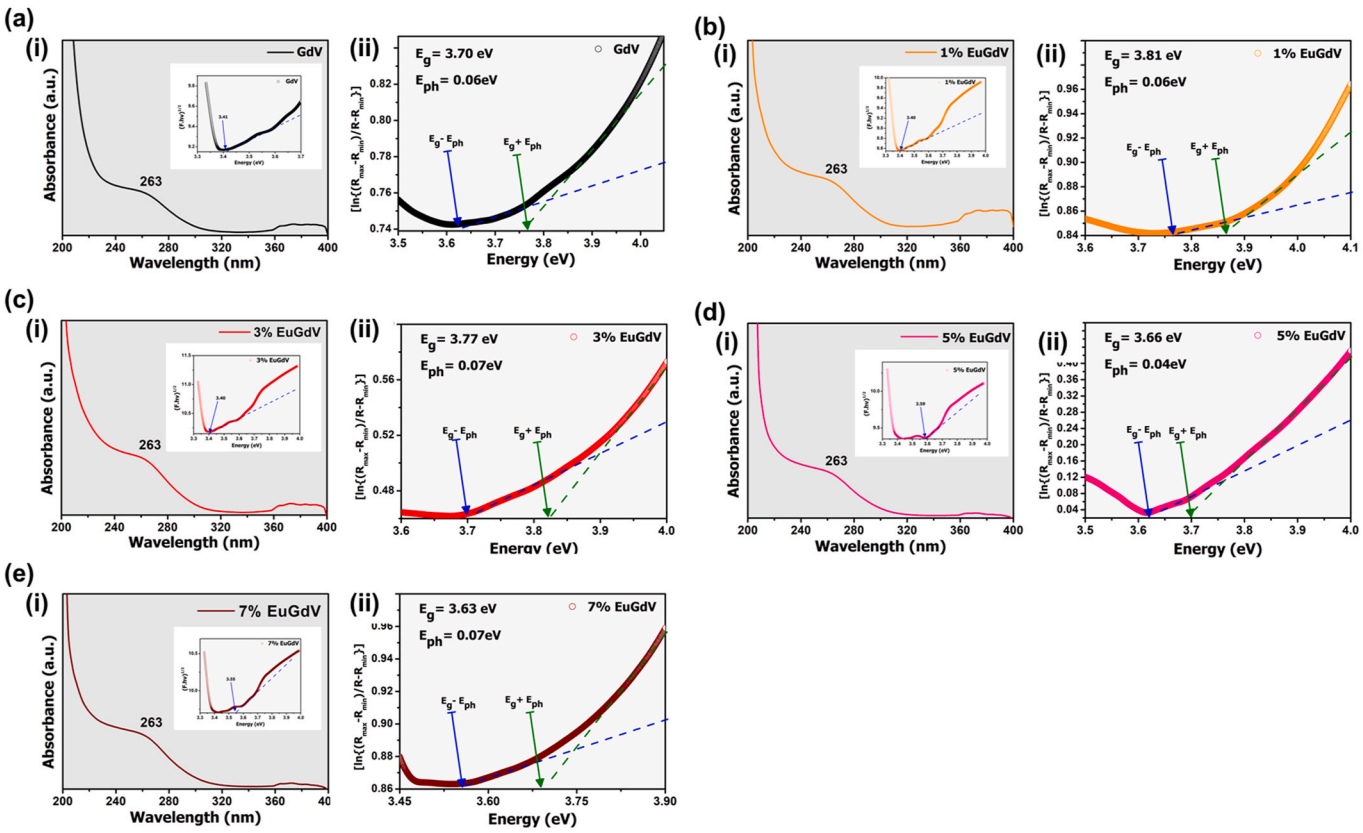

Fig. 4. UV–Vis absorbance spectra of nanophosphors with optical band gap (calculated using Kubelka Munk method) shown as figure inset is shown in (i) for (a), (b), (c), (d), and (e) corresponding to GdV, 1% EuGdV, 3% EuGdV, 5% EuGdV, and 7% EuGdV respectively. Meanwhile the optical band gap and phononic energy calculated using Kumar's model are shown in (ii) for the above-mentioned samples.

tetragonal lattice of $GdVO_4$ [63]. Although the CLS signal for $3d_{5/2}$–1136 eV (characteristic of Eu^{3+}) was observed, no tracefor Eu^{2+} state was witnessed [64]. This observation further provides substantial evidence that the Eu^{3+} has been doped into the vanadate system appropriately.

3.3. Optical absorption and association of charge transfer bands

Like in any typical host sensitizing luminescent candidate, in Eu^{3+}: $GdVO_4$ absorption and consequently, energy transfer (ET) from the host to activators are hugely accountable for emission intensity and phosphor efficiency. Upon UV excitation, the energy absorbed through the $GdVO_4$ host is efficiently transferred to the Eu^{3+} centers. Typically, Fig. 4 shows the UV–Vis spectra in the UV region, which does not warrant any peak centering ~205 nm (corresponding to absorption by $4f^n$ of RE^{3+}), thereby implying effective ET between VO_4^{3-} and 4*f* energy levels [5]. Intense broad bands ranging between 230 and 290 nm are accredited to charge transfer (CT) mediated transitions inside $[VO_4]^{3-}$ groups [38,65]. It was proposed earlier that the CT assisted transition from $^1A_1$ to ($^1T_1$, $^1T_2$) would give rise to a doublet, broad structure as well as intense absorption band in the UV region wherein $^1A_1$ is the ground state and $^1T_1$, $^1T_2$ are excited states of VO_4^{3-}, in conformity with molecular orbital theory (MOT) [66–68]. Furthermore, one-electron CT also takes place between the O2*p* orbital and the vacant 3*d* orbital of the central vanadium (V^{5+}) in the tetrahedral VO_4^{3-} with T_d symmetry. The peak centered at ~263 nm can thus be attributed to the overlapping of two CT processes: (i) involving Eu–O (appearing at higher energy) and V–O components [52,69,70] and (ii) electric and dipole-allowed transitions from the $^1A_2$ to the ^1E and $^1A_1$ excited states of the VO_4^{3-} ion [43]. The weaker line at 396 nm is assigned to the *f* –*f* transitions of Eu^{3+}. The intrinsic Eu^{3+} absorbance at ~400 nm corresponding to general *f* –*f* transitions is much weaker than host excitation of the VO_4^{3-} groups, indicating that the excitation of Eu^{3+} is mainly through the VO_4^{3-} groups [71]. Following Eu^{3+} in eight-coordination, the CT band (220–270 nm) overlaps with that of the vanadate group and a single broad peak is thus observed due to vanadate absorption followed by ET [36]. It is the CT transitions from the highest occupied molecular orbital (HOMO) level *i.e.* O^{2-} nonbonding orbitals, to the lowest unoccupied molecular orbital (LUMO) level composed of antibonding V3*d* orbitals and O2*p* orbitals, in tetrahedral VO_4^{3-}, which describe the origin of the intrinsic luminescence from RE-vanadates [72]. Optical band gap of the RE-vanadate system has been reported earlier ranging 3.28–3.75 eV [38]. Following eqn. (5), we determined the optical band gaps to be 3.4–3.59 eV (shown as insets, in Fig. 4), with meV order increments upon increasing dopant concentration. Furthermore, the optical gaps were also estimated through a model proposed by V. Kumar *et al.*[73]. This band gap so determined (following eqn. (6)) incorporates the phononic absorption and considers its contribution to the optical transitions and was found to be ranging ~3.63–3.8 eV. We have,

$$\alpha(h\upsilon) = F(h\upsilon) = \frac{\{1 - R(h\upsilon)\}^2}{2R(h\upsilon)} \tag{5}$$

$$\alpha h\upsilon = \frac{ln\left[\frac{(R_{max} - R_{min})}{(R(h\upsilon) - R_{min}}\right]}{2l} \tag{6}$$

In eqs. Eqs. (5) and (6), 'α' is absorption coefficient, 'R' is reflectance measured with 'l' as the optical path length.

The difference in ionic radius of dopant and host ions can lead to moderate modifications of phonon density of states which can perturb the observed energy band gap [74]. This occurs due to involvement of an additional process in the transitions i.e., phonon emission component along with photon absorption [75,76]. Furthermore, increment in band

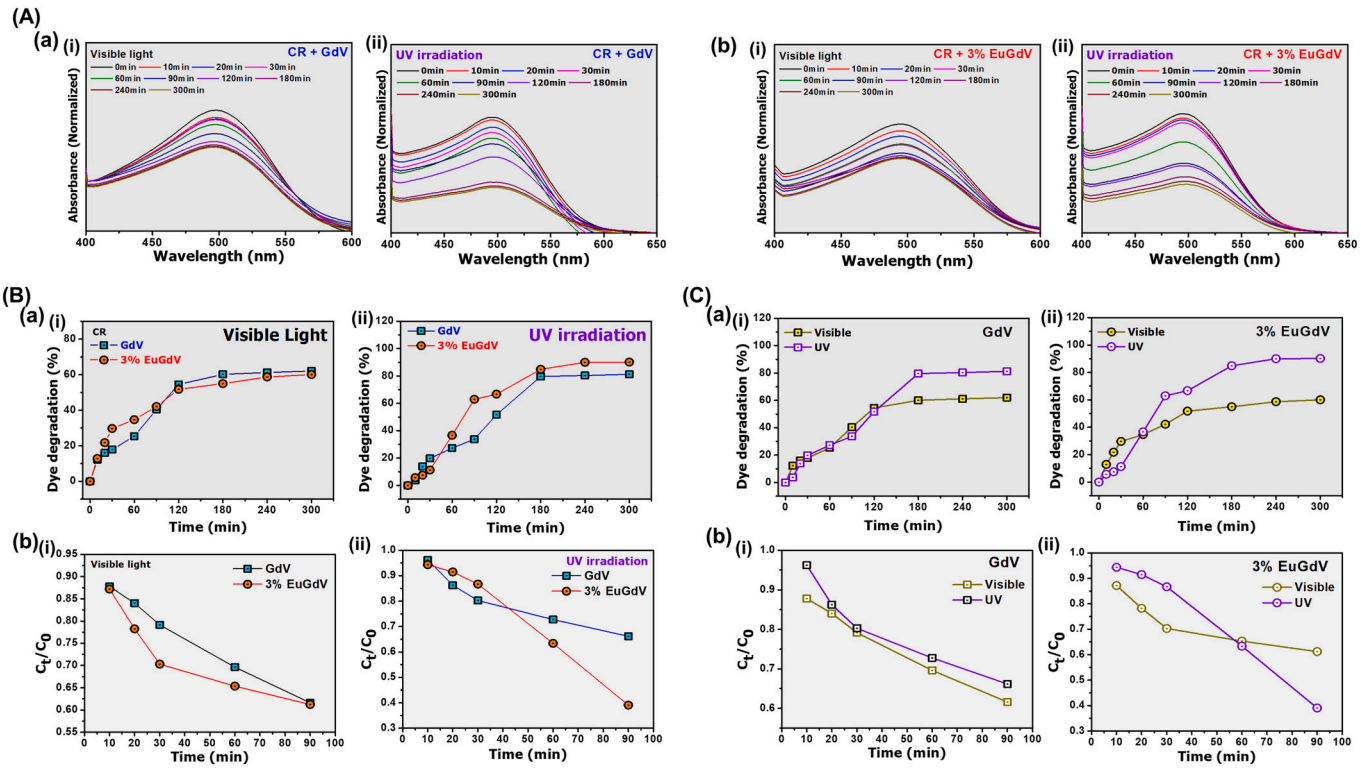

Fig. 5. Photocatalytic behavior of nanocatalyst against CR dye: (A) progressive optical absorption features (a) GdV, and (b) EuGdV with (i) visible light, and (ii) UV light illumination. (B) A comparative view on dye degradation in terms of (a) percentage, and (b) relative concentration with time progression. (C) a comparative account on photocatalystic effeciencies of nanocatalysts under visible and UV exposures.

gap energies in vanadate nanosystem is, in general, ascribed to the Moss-Burstein (M − B) effect instead of quantum confinement, as the Bohr radii for vanadate hosts are quite small, ~1.15 Å [77]. The M-B effect describes a situation where the electron population eventually exceeds both the conduction band edge density of states and the Fermi level. As all the states below the Fermi level are occupied states, it would thus occupy a position in the conduction band itself. The small variation in the band gap can also be attributed to the presence of deep defect states for highly concentrated defect V^{5+} centers, i.e. lower valence state. The vanadium ion adjacent to an oxygen vacancy or a vanadium antisite defect/dislocation could induce numerous newer energy levels thereby lowering the band gap [30].

3.4. Photocatalytic activity of the nanocatalyst against CR

To determine the potential applicability of the GdV and EuGdV against CR dye, photocatalytic experiment was carried out under visible light and UV illumination for a given time duration. Fig. 5(A) displays the absorbance quenching of CR treated with (a) GdV, and (b) 3% EuGdV under both the irradiation conditions i.e., (i) visible and (ii) UV. It is noteworthy that reports can be found suggesting improvement of photocatalytic activity of the doped nanosystem upon increasing Eu^{3+} concentration, however, the enhancement saturates for a dopant level beyond ~1.46 wt% [71]. It must thus be noted that excess Eu species may either act as recombination centers, or covers of active sites on the catalyst surfaces. Consequently, higher Eu concentration results in confinement of Eu^{3+} on the surface of the catalysts, and the possibility for the trapped electrons to recombine with the holes increases eventually. In such case, efficiency of charge separation gets reduced [35]. In addition, it must be noted that Eu^{3+} concentration above ~5 mol% attracts quenching effects that occurs due to energy transfer between neighboring Eu^{3+} ions [78]. Such an energy transfer reduces the efficacy of UV excitation and can result in lower photocatalytic performance. In order to avoid reduction of charge separation due to excess Eu^{3+} in the system leading to increased energy transfer and thus poorer photocatalytic activity, ~3 mol% EuGdV nanosystem was chosen purposefully for photocatalytic studies. In fact, we observed an excellent photocatalytic behavior of the nanocatalyst that leads to an efficient degradation of the target CR molecules within 120 min, beyond which the process is slowed down. The digital photographs of the dye illustrating progressive discoloration after 180 min of treatment time under both the visible light and UV irradiation are shown in Fig.S3.

The variation in percentage of dye degradation for both the nanosystems under bright light illumination can be found in Fig. 5(B) (a). Here, both GdV and EuGdV displayed quite similar results with an effective dye degradation up to ~60% after a treatment time of 300 min. For the initial 120 min, the activity progressed steadily following which the behavior gets a saturative trend. Interestingly, upon treatment with UV light (Fig. 5(B)(a) (ii)), the photodegradation efficiency shoots up to ~80% for GdV, and even as high as ~91.8% for 3% EuGdV nanocatalyst. The kinetics of CR-dye degradation process is shown in Fig. 5(B)(b) and can be well described through Langmuir–Hinshelwood (L-H) model, expressed in the form of a first-order reaction considering a dilute solution [79]:

$$C_t = C_0 e^{-kt} \tag{7}$$

In Eq. (7), 't' is the irradiation time while 'k' is pseudo-first order rate constant. The rate constant was predicted from the plot of (C_t/C_0) versus 't', as shown as insets of Fig. 5(A) and (B)- (b, c). To be mentioned, with visible light irradiation, the rate constants were found similar for both the undoped (GdV) and doped (EuGdV) nanosytems but k value gets augmented considerably from ~0.034 min^{-1} to ~0.071 min^{-1} under UV light illumination. Such an increment in rate constant upon Eu incorporation is unprecedented, suggesting that the Eu^{3+} dopant ions are effecient enough in improving photocatalytic activity under UV exposure. Available reports suggest rate constants, for degradation of azo

Table 1
A comparative view on the photocatalytic performance of $REVO_4$ and other nanophotocatalysts against different organic dye types.

Sl. no	Target dye/ contaminant	Material	Illumination source	Degradation % - Treatment time	Ref
1	Congo red	$CuInSe_2$–ZnO nanocomposites	UV	99.8% - 90min	[83]
			Visible	80.3%- 120min	
2		Ba/Alg/CMC/ TiO_2 composite	Solar light	91.5 %-240min	[86]
3		Zn-doped $CdTiO_3/TiO_2$	Solar light	90%- 15 min	[97]
4		$PbTiO_3$	Visible	92%- 150min	[98]
5		TiO_2	Multi lamp photoreactor	74–120min	[99]
		CNBF/TiO_2	Multi lamp photoreactor	83–120min	
6	Malachite Green	$GdVO_4$	Visible	96.2%- 50min	[84]
	Rhodamine Blue			89.2%- 50min	
	Methylene Blue			87.8%- 50min	
7	Rhodamine Blue	$GdVO_4$	Solar light	69%- 360min	[31]
8	Acetone	$GdVO_4$-V_2O_5	Visible	95.5%- 180min	[26]
9	Methyl orange	$GdVO_4$	UV light	85% −70 min	[100]
10	Congo red	Eu^{3+}:$GdVO_4$	UV light and visible light	91%- 180 min	This work

dyes using $ReVO_4$ nanosystem to be 0.064 min^{-1} ($CeVO_4$), 0.066 min^{-1} ($PrVO_4$) and 0.058 min^{-1} ($NdVO_4$) [80]. Our observation in case of 3% EuGdV is comparable to the degradation rate constant for commercially available TiO_2/Degussa P-25 (k = 0.079 min^{-1}) thereby confirming potential use for azo dye degradation. Based on the available literature, description of origin of photocatalytic activity by a nanosystem involves various parameters, *viz.* high surface area, finite band gap, crystallinity of the photocatalyst, presence of defect states (typically, oxygen based) etc. Previously lanthanides have shown substantial enhancement in photocatalytic activity under visible light irradiation as well, however the prime mechanism responsible has not yet been established [81]. A comprehensive comparative overview focusing on photocatalytic performance of $REVO_4$ as nano-photocatalyst against CR and other dye types can be found in Table 1. In general, a photocatalytic reaction proceeds via several bulk steps [21,82,83]:

(a) *Photoexcitation:* Depending on the source of illumination and bandgap of the catalyst used, photons of definite energy are utilized in exciting the electrons of the valence band (VB) to jump into the conduction band (CB).
(b) *Charge separation*: The photoexcitation process leads to generation of electron-hole pairs with positive holes (h^+) in VB and electrons (e^-) in the CB [84,85].
(c) *Migration:* A share of the photogenerated pairs distributes out to the photocatalyst surface wherein they participate in chemical reactions with the solvent media adsorbed onto the surface reducing the dissolved oxygen and surface hydroxyl group (-OH) leading to photocatalysis [86,87].
(d) *Recombination:* Recombination is a very quick process, and thus efficacy of the photocatalysis relies on the amount of reactants adsorbed on the surface of the photocatalyst. Holes have strong oxidizing capacity and are capable of producing highly reactive hydroxyl radicals and superoxide radical ions by oxidizing adsorbed organic contaminants and water adsorbed on the photocatalyst surface [83,84]. Consequently, the super reactive radicals facilitate dye degradation thereby generating wide ranging intermediates, which are known to completely mineralize into carbon dioxide, water, ammonium and nitrate ions [86]. The reaction steps involved in the entire photocatalytic response is detailed below:

$$GdV \xrightarrow{h\nu} GdV\left(e_{CB}^- + h_{VB}^+\right) \quad \text{(i)}$$

$$GdV\left(h_{VB}^+\right) + H_2O \text{ or } OH^- \rightarrow H^+ + OH^{\cdot} \quad \text{(ii)}$$

$$GdV\left(e_{CB}^-\right) + O_2 \rightarrow O^{2-} \quad \text{(iii)}$$

$$O^{2-} + H^+ \rightarrow HO_2^{\cdot} \quad \text{(iv)}$$

$$2HO_2^{\cdot} \rightarrow H_2O_2 + O_2 \quad \text{(v)}$$

$$H_2O_2 \rightarrow 2OH^- \quad \text{(vi)}$$

Consequently,

$$CR\ dye + O_2^- + OH^{\cdot} \rightarrow intermediate\ products \rightarrow CO_2 + H_2O + NO_3^- + NH_4^+ \quad \text{(vii)}$$

K. Hubenko *et al.* has reported that Eu^{3+}:$GdVO_4$ nanoparticles have a great potential in generating reactive oxygen species in aqueous solutions containing azo dyes [88]. Furthermore, surface oxygen coordination defects of V atoms are known to activate the water dissociative adsorption thereby creating radical ions. It is worth mentioning here that the highest occupied state of the RE-vanadates energy levels are located above occupied O2*p* orbitals of the adsorbed water molecules, enabling them to generate hydrogen from water dissociation [89]. Optically excited transitions involved in $GdVO_4$ *viz.* from occupied valence band to unoccupied Gd 4*f* band and O2*p* to V3*d*, promotes hydrogen generation in aqueous media [83]. For more clarity of the effect of irradiation type in enhancing as regards the photocatalytic activity of both the polyhedral nanosystems, we refer to Fig. 5(C)(a). It infers augmented dye degradation process upon UV irradiation which is quite evident for (i) GdV and (ii) 3% EuGdV. Interestingly, the observation is more pronounced in case of 3% EuGdV with an efficiency as high as 91.8%.

In fact, our observations suggest that incorporation of Eu^{3+} as dopant into the GdV host leads to a better photocatalytic agent. It is noteworthy that for both the photocatalysts, the synthesis as well as treatment conditions were same. The only difference lies in the presence/absence of Eu^{3+} as dopant in the host lattice. Inclusion of dopants into the system introduces various changes in the host system, both physical as well as optical. It has been reported that increment of porosity due to doping can lead to enhanced photocatalytic activity [49]. However, in our case, the porosity was found to be slightly lowered: 4.64% for GdV, and 4.58% for 3% EuGdV. The effect of change in porosity is not the only criterion for augmenting the photocatalytic activity observed. It is worth mentioning that the UV irradiation wavelength is closer to absorbance transition peak of Eu^{3+} which facilitates photoexcitation events efficiently resulting in profound generation of *e-h* pairs. The increased activity of photocatalyst upon Eu dopant has been proposed to occur via trapping of photogenerated electrons within the catalyst, thereby reducing the extent of electron–hole recombination known for diminishing the activity [90]. Such electron trapping by Eu^{3+} dopant reduces the electron–hole recombination rate in the reaction and therefore additional holes are available for the redox reactions involved in the photodegradation of the dye [91]. The CT processes involving Eu–O and general intra *f* transitions due to Eu^{3+} incorporation into the vanadate matrix, further enables greater generation of more reactive species that facilitates decomposition and decolorization of CR under UV light.

Enhanced photocatalytic activity of 3% EuGdV in our observation can be explained citing the organic contaminant, CR, disintegrated

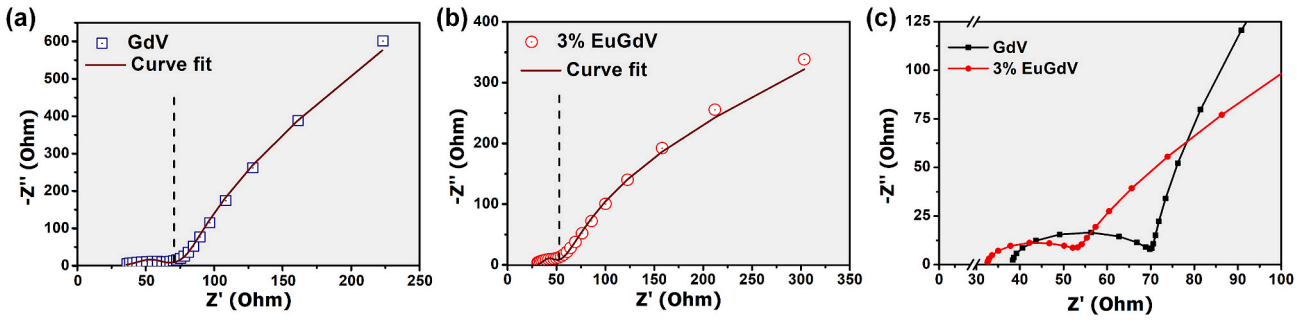

Fig. 6. Electrical impedance spectroscopy (EIS) of nanocatalysts (a) GdV, and (b) 3% EuGdV. A comparative, zoomed view of the arcs can be found in (c).

eventually following production of CO_2, water and other byproducts.

3.5. Electrochemical impedance spectroscopy (EIS) studies

To evaluate the resistive behavior of the photocatalysts, they were fabricated as electrodes and electrochemical route was employed for EIS measurements, shown in Fig. 6. It demonstrates Z″ vs. Z' response of impedances at different frequencies along with typical electrode effect. These plots, popularly known as, the Nyquist plots normally appear with the linear part (low-frequency region) and the arc (high frequency region) and their conjunction in the mid-frequency regime. The exact vertical trend at lower frequencies indicates a pure capacitive feature, and a representative of the ion diffusive nature in the electrode structure. It is known that the long tail of the linear Nyquist plot in the low frequency region ideally forms the diffusion mediated impedance (termed as, Warburg impedance) which arises as a consequence of diffusion of redox entities from the bulk solution to the electrode surfaces [92]. A curve in low frequency region can be demonstrated as either a vertical line (characteristic of an ideal capacitor) [93], or a bent curve which implies complex structure of the porous material [94]. Noticeably, the GdV is closer to the vertical trend and hence exhibits a better capacitive feature as compared to 3%EuGdV system. Consequently, 3%EuGdV electrode experiences a better charge diffusion process, preventing charge accumulation at large.

In the high frequency regime, the arc/semicircle is generally associated with the surface adsorption properties of the porous electrode, in accordance with the faradaic charge transfer resistance (R_{ct}) [92]. The respective R_{ct} values predicted for GdV, and 3% EuGdV are 32.1 Ω and 20.59 Ω. Apparently, a smaller R_{ct} value of 3% EuGdV can imply better electrode-electrolyte charge transfer as compared to its GdV counterpart [94,95]. The variation in R_{ct} values between two active materials can be attributed to the variation in specific surface areas and dispersity of the nanosystem in the electrolyte [96]. The incorporation of Eu^{3+} is believed to favor quicker charge separation and migration and hence, offer a better nanocatalyst for a doped system.

4. Conclusion

This work demonstrated processing and characterization of Eu^{3+} doped orthovanadate nanosystem exhibiting zircon type crystal structure. The samples were analyzed employing diffraction, spectroscopic and electrochemical techniques. The effect of introduction of Eu^{3+} dopant into the vanadate matrix was studied in detail. To be mentioned, a weak peak at ~1137 eV has been witnessed in the XPS spectra for the 3%EuGdV, describing +3 oxidation state of the europium in the $GdVO_4$ lattice. While the XRD study and TEM imaging reveal structural and morphological features, optical and photocatalytic characteristics helped determine optical band gaps and photodegradation efficiency; respectively. The CR dye was apparently degraded to the tune of ~91.8% by Eu^{3+}:$GdVO_4$ nanocatalyst, to other intermediate aromatic species, with noticeable discoloration effect. In the process, the rate constant gets doubled with the inclusion of dopants into the host lattice and possible explanation for enhanced charge diffusion was made with the help of EIS analysis. The quantification and toxicity tests of these intermediate products, which promise to be an interesting area of research would provide vital information regarding environmental remediation and safe use of the catalytic agent for its industrial relevance.

Data availability

The data involved in this work may be available upon reasonable request.

Declaration of competing interest

The authors declare that they have no known competing financial interests or personal relationships that could have appeared to influence the work reported in this paper.

Acknowledgments

The authors express their sincere thanks to SAIC-TU for providing TEM facility and NEIST, Jorhat for extending XPS measurements and SAIF-NEHU for carrying out ICP-OES measurements. One of the authors (AA) thank Mr. Ankush Medhi, Department of Physics, TU for his assistance in conducting EIS analysis and Ms. Anamika Nath, Department of Environmental Science, TU for her support in microwave digestion of samples for ICP-OES measurements.

Appendix A. Supplementary data

Supplementary data to this article can be found online at https://doi.org/10.1016/j.physe.2022.115357.

References

[1] F. Wang, X. Xue, X. Liu, Angew. Chem. 120 (2008) 920–923.
[2] J. Shen, L.D. Sun, J.D. Zhu, L.H. Wei, H.F. Sun, C.H. Yan, Adv. Funct. Mater. 20 (2010) 3708–3714.
[3] M. Zhao, G. Li, J. Zheng, L. Li, L. Yang, CrystEngComm 14 (2012) 2062–2070.
[4] A. Zagumennyĭ, V. Ostroumov, I.A. Shcherbakov, T. Jensen, J. Meyen, G. Huber, Sov. J. Quant. Electron. 22 (1992) 1071.
[5] X. Su, B. Yan, H. Huang, J. Alloys Compd. 399 (2005) 251–255.
[6] L. Qian, J. Zhu, Z. Chen, Y. Gui, Q. Gong, Y. Yuan, J. Zai, X. Qian, Chem.–Eur. J. 15 (2009) 1233–1240.
[7] Z. Xu, C. Li, Z. Hou, C. Peng, J. Lin, CrystEngComm 13 (2011) 474–482.
[8] N.S. Singh, R. Ningthoujam, L.R. Devi, N. Yaiphaba, V. Sudarsan, S.D. Singh, R. Vatsa, R. Tewari, J. Appl. Phys. 104 (2008), 104307.
[9] R. Ropp, J. Electrochem. Soc. 115 (1968) 940.
[10] L. Yang, G. Li, W. Hu, M. Zhao, L. Sun, J. Zheng, T. Yan, L. Li, Control over the Crystallinity and Defect Chemistry of YVO_4 Nanocrystals for Optimum Photocatalytic Property, Wiley Online Library2011.
[11] S. Erdemoğlu, S.K. Aksu, F. Sayılkan, B. Izgi, M. Asiltürk, H. Sayılkan, F. Frimmel, Ş. Güçer, J. Hazard Mater. 155 (2008) 469–476.
[12] R. Molinari, F. Pirillo, M. Falco, V. Loddo, L. Palmisano, Chem. Eng. Process: Process Intensif. 43 (2004) 1103–1114.

[13] V.A. Sakkas, M.A. Islam, C. Stalikas, T.A. Albanis, J. Hazard Mater. 175 (2010) 33–44.
[14] M. Varga, D. Kopecký, J. Kopecká, I. Křivka, J. Hanuš, A. Zhigunov, M. Trchová, M. Vrňata, J. Prokeš, Eur. Polym. J. 96 (2017) 176–189.
[15] S. Rattanapan, J. Srikram, P. Kongsune, Energy Proc. 138 (2017) 949–954.
[16] A.K. Jha, S. Chakraborty, Water Sci. Technol. 82 (2020) 2491–2502.
[17] C. Namasivayam, D. Kavitha, Dyes Pigments 54 (2002) 47–58.
[18] S. Chakraborty, M. Purkait, S. DasGupta, S. De, J. Basu, Separ. Purif. Technol. 31 (2003) 141–151.
[19] T. Etemadinia, B. Barikbin, A. Allahresani, Surface. Interfac. 14 (2019) 117–126.
[20] X. Song, G. Qin, G. Cheng, W. Jiang, X. Chen, W. Dai, X. Fu, Appl. Catal. B Environ. 284 (2021), 119761.
[21] H. Li, S. Yin, Y. Wang, T. Sato, Appl. Catal. B Environ. 132 (2013) 487–492.
[22] K. Wang, R. Jiang, T. Peng, X. Chen, W. Dai, X. Fu, Appl. Catal. B Environ. 256 (2019), 117780.
[23] A. Ismail, I. Ibrahim, M. Ahmed, R. Mohamed, H. El-Shall, J. Photochem. Photobiol. Chem. 163 (2004) 445–451.
[24] H. Xu, H. Shang, C. Wang, L. Jin, C. Chen, C. Wang, Y. Du, Appl. Catal. B Environ. 265 (2020), 118605.
[25] H. Xu, H. Shang, L. Jin, C. Chen, C. Wang, Y. Du, J. Mater. Chem. 7 (2019) 26905–26910.
[26] Y. He, J. Cai, T. Li, Y. Wu, H. Lin, L. Zhao, M. Luo, Chem. Eng. J. 215 (2013) 721–730.
[27] M. Oshikiri, J. Ye, M. Boero, J. Phys. Chem. C 118 (2014) 12845–12854.
[28] P. Karimi, K. Hui, K. Komal, Iran. J. Mater. Sci. Eng. 7 (2010) 25–30.
[29] H. Xu, H. Wang, H. Yan, J. Hazard Mater. 144 (2007) 82–85.
[30] V. Klochkov, J. Photochem. Photobiol. Chem. 310 (2015) 128–133.
[31] Y. Bai, Y.M. Ding, Z.M. Li, Photocatalytic water splitting and photocatalytic degradation in aqueous GdVO4 suspensions under simulated solar irradiation, Advanced Materials Research, Trans. Tech. Publ2014, 571-574.
[32] P. Mazierski, J. Sowik, M. Miodyńska, G. Trykowski, A. Mikołajczyk, T. Klimczuk, W. Lisowski, J. Nadolna, A. Zaleska-Medynska, Dalton Trans. 48 (2019) 1662–1671.
[33] H. Lim, S.B. Rawal, Prog. Nat. Sci.: Mater. Int. 27 (2017) 289–296.
[34] Y. Xie, C. Yuan, X. Li, Mater. Sci. Eng. B 117 (2005) 325.
[35] A. Zhang, J. Zhang, J. Hazard Mater. 173 (2010) 265–272.
[36] J. Bae, S. Park, T. Hong, J. Kim, J. Yoon, E. Jeong, M. Won, J. Jeong, Curr. Appl. Phys. 9 (2009) S241–S244.
[37] S. Osawa, T. Katsumata, T. Iyoda, Y. Enoki, S. Komuro, T. Morikawa, J. Cryst. Growth 198 (1999) 444–448.
[38] D.J. Jovanović, A. Chiappini, L. Zur, T.V. Gavrilović, T.N.L. Tran, A. Chiasera, A. Lukowiak, K. Smits, M.D. Dramićanin, M. Ferrari, Opt. Mater. 76 (2018) 308–316.
[39] L. Carvalho, A.T. Reis, E. Soares, C. Tavares, R.J. Monteiro, P. Figueira, B. Henriques, C. Vale, E. Pereira, Water, Air, Soil Pollut. 231 (2020) 1–14.
[40] S.-M. Ryu, C. Nam, Appl. Phys. A 126 (2020) 1–8.
[41] Z. Xu, B. Feng, Y. Gao, Q. Zhao, D. Sun, X. Gao, K. Li, F. Ding, Y. Sun, CrystEngComm 14 (2012) 5530–5538.
[42] A. Szczeszak, T. Grzyb, Z. Śniadecki, N. Andrzejewska, S. Lis, M. Matczak, G. Nowaczyk, S. Jurga, B. Idzikowski, Inorg. Chem. 53 (2014) 12243–12252.
[43] S. Tang, M. Huang, J. Wang, F. Yu, G. Shang, J. Wu, J. Alloys Compd. 513 (2012) 474–480.
[44] B. Yan, J.-H. Wu, Mater. Lett. 63 (2009) 946–948.
[45] K.A. Gschneidner, J.-C.G. Bunzli, V.K. Pecharsky, Handbook on the Physics and Chemistry of Rare Earths: Optical Spectroscopy, Elsevier2011.
[46] J.H. Kang, W.B. Im, D.C. Lee, J.Y. Kim, D.Y. Jeon, Y.C. Kang, K.Y. Jung, Solid State Commun. 133 (2005) 651–656.
[47] J.t. Baglio, O. Sovers, J. Solid State Chem. 3 (1971) 458–465.
[48] S. Mahapatra, A. Ramanan, J. Alloys Compd. 395 (2005) 149–153.
[49] M. Sukumar, L.J. Kennedy, J.J. Vijaya, B. Al-Najar, M. Bououdina, Ceram. Int. 44 (2018) 18113–18122.
[50] N. Ashraf, M. Aadil, S. Zulfiqar, H. Sabeeh, M.A. Khan, I. Shakir, P.O. Agboola, M. F. Warsi, ChemistrySelect 5 (2020) 8129–8136.
[51] G.T. Anand, L.J. Kennedy, J. Nanosci. Nanotechnol. 13 (2013) 3096–3103.
[52] K. Riwotzki, M. Haase, J. Phys. Chem. B 102 (1998) 10129–10135.
[53] T. Carbonati, C. Cionti, E. Cosaert, B. Nimmegeers, D. Meroni, D. Poelman, J. Alloys Compd. 862 (2021), 158413.
[54] S. Tougaard, I. Chorkendorff, Phys. Rev. B 35 (1987) 6570.
[55] J.-P. Zhou, C.-L. Chai, S.-Y. Yang, Z.-K. Liu, S.-L. Song, Y.-L. Li, N.-F. Chen, J. Cryst. Growth 270 (2004) 21–29.
[56] D. Barreca, A. Gasparotto, A. Milanov, E. Tondello, A. Devi, R.A. Fischer, Surf. Sci. Spectra 14 (2007) 60–67.
[57] F. Zheng, W. Wang, P. Yang, Optoelectr. Adv. Mater. Rapid Commun. 5 (2011) 596–599.
[58] D. Zatsepin, V. Galakhov, M. Korotin, V. Fedorenko, E. Kurmaev, S. Bartkowski, M. Neumann, R. Berger, Phys. Rev. B 57 (1998) 4377.
[59] J. Gupta, D. Landheer, J. McCaffrey, G. Sproule, Appl. Phys. Lett. 78 (2001) 1718–1720.
[60] A. Molle, C. Wiemer, M.N.K. Bhuiyan, G. Tallarida, M. Fanciulli, G. Pavia, Appl. Phys. Lett. 90 (2007), 193511.
[61] C. Wagner, A. Naumkin, A. Kraut-Vass, J. Allison, C. Powell, J. Rumble Jr., National Institute of Standards and Technology, Gaithersburg, MD, 2003, 20899.
[62] M.C. Biesinger, L.W. Lau, A.R. Gerson, R.S.C. Smart, Appl. Surf. Sci. 257 (2010) 887–898.
[63] P. Shandilya, D. Mittal, A. Sudhaik, M. Soni, P. Raizada, A.K. Saini, P. Singh, Separ. Purif. Technol. 210 (2019) 804–816.
[64] D. Kim, Y.-H. Jin, K.-W. Jeon, S. Kim, S.-J. Kim, O.H. Han, D.-K. Seo, J.-C. Park, RSC Adv. 5 (2015) 74790–74801.
[65] Q.-l. Zhang, C.-x. Guo, C.-s. Shi, S.-z. Lü, J. Alloys Compd. 309 (2000) 10–15.
[66] H. Ronde, G. Blasse, J. Inorg. Nucl. Chem. 40 (1978) 215–219.
[67] T. Nakajima, M. Isobe, T. Tsuchiya, Y. Ueda, T. Manabe, J. Phys. Chem. C 114 (2010) 5160–5167.
[68] H. Ronde, J. Snijder, Chem. Phys. Lett. 50 (1977) 282–283.
[69] D. Geng, E. Cabello-Olmo, G. Lozano, H. Míguez, Mater. Horiz. 5 (2018) 661–667.
[70] L. Yang, G. Li, M. Zhao, J. Zheng, X. Guan, L. Li, Nanotechnology 23 (2012), 245602.
[71] Z. Xu, X. Kang, C. Li, Z. Hou, C. Zhang, D. Yang, G. Li, J. Lin, Inorg. Chem. 49 (2010) 6706–6715.
[72] M.R. Dolgos, A.M. Paraskos, M.W. Stoltzfus, S.C. Yarnell, P.M. Woodward, J. Solid State Chem. 182 (2009) 1964–1971.
[73] V. Kumar, S.K. Sharma, T. Sharma, V. Singh, Opt. Mater. 12 (1999) 115–119.
[74] D.J. Jovanović, Ž. Antić, R.M. Krsmanović, M. Mitrić, V. Đorđević, B. Bártová, M. D. Dramićanin, Opt. Mater. 35 (2013) 1797–1804.
[75] M. Wakaki, T. Shibuya, K. Kudo, Physical Properties and Data of Optical Materials, CRC press2018.
[76] Y.A. Kuznetsova, A. Zatsepin, Optical properties and energy parameters of Gd2O3 and Gd2O3: Er nanoparticles, J. Phys.: Conf. Ser. (2017), 062001. IOP Publishing.
[77] G. Mialon, S. Turkcan, A. Alexandrou, T. Gacoin, J.-P. Boilot, J. Phys. Chem. C 113 (2009) 18699–18706.
[78] Z. Wei, L. Sun, C. Liao, J. Yin, X. Jiang, C. Yan, S. Lü, J. Phys. Chem. B 106 (2002) 10610–10617.
[79] S.J. Hazarika, D. Mohanta, Appl. Phys. A 123 (2017) 381.
[80] S. Mahapatra, G. Madras, T. Guru Row, Ind. Eng. Chem. Res. 46 (2007) 1013–1017.
[81] A. Sobhani-Nasab, M. Behpour, J. Mater. Sci. Mater. Electron. 27 (2016) 11946–11951.
[82] B. Palanisamy, C. Babu, B. Sundaravel, S. Anandan, V. Murugesan, J. Hazard Mater. 252 (2013) 233–242.
[83] M. Bagheri, A.R. Mahjoub, B. Mehri, RSC Adv. 4 (2014) 21757–21764.
[84] A. He, L. Feng, L. Liu, J. Peng, Y. Chen, X. Li, W. Lu, J. Liu, J. Mater. Sci. Mater. Electron. 31 (2020) 13131–13140.
[85] M.R. Hoffmann, S.T. Martin, W. Choi, D.W. Bahnemann, Chem. Rev. 95 (1995) 69–96.
[86] M. Thomas, T.S. Natarajan, M.U.D. Sheikh, M. Bano, F. Khan, J. Photochem. Photobiol. Chem. 346 (2017) 113–125.
[87] T.L. Thompson, J.T. Yates, Chem. Rev. 106 (2006) 4428–4453.
[88] K. Hubenko, S. Yefimova, T. Tkacheva, P. Maksimchuk, I. Borovoy, V. Klochkov, N. Kavok, O. Opolonin, Y. Malyukin, Nanoscale Res. Lett. 13 (2018) 1–9.
[89] M. Oshikiri, M. Boero, A. Matsushita, J. Ye, J. Chem. Phys. 131 (2009), 034701.
[90] E. Borgarello, J. Kiwi, M. Graetzel, E. Pelizzetti, M. Visca, J. Am. Chem. Soc. 104 (1982) 2996–3002.
[91] J. Xu, Y. Ao, D. Fu, C. Yuan, J. Colloid Interface Sci. 328 (2008) 447–451.
[92] Y. Wang, D. Zhao, Y. Zhao, C. Xu, H. Li, RSC Adv. 2 (2012) 1074.
[93] Y. Wang, Z. Shi, Y. Huang, Y. Ma, C. Wang, M. Chen, Y. Chen, J. Phys. Chem. C 113 (2009) 13103–13107.
[94] L. Wang, G. Duan, J. Zhu, S.-M. Chen, X.-h. Liu, S. Palanisamy, J. Colloid Interface Sci. 483 (2016) 73–83.
[95] A. He, L. Feng, L. Liu, J. Peng, Y. Chen, X. Li, W. Lu, J. Liu, J. Mater. Sci. Mater. Electron. 31 (2020) 13131–13140.
[96] X. Zhang, Y. Zhao, C. Xu, Nanoscale 6 (2014) 3638–3646.
[97] A. Moradzadeh, A. Mahjoub, M.S. Sadjadi, M.H. Sadr, N. Farhadyar, Polyhedron 170 (2019) 404–411.
[98] U.O. Bhagwat, J.J. Wu, A.M. Asiri, S. Anandan, ChemistrySelect 3 (2018) 11851–11858.
[99] R. Ramakrishnan, S. Kalaivani, J.A.I. Joice, T. Sivakumar, Appl. Surf. Sci. 258 (2012) 2515–2521.
[100] M. Vosoughifar, J. Mater. Sci. Mater. Electron. 28 (2017) 6119–6124.

Bull. Mater. Sci. (2022)45:21
https://doi.org/10.1007/s12034-021-02592-2

Significant red-luminescence from citrate-gel and hydrothermally derived nanoscale Eu^{3+}: Gd_2O_3 with alkali metal ion (Na^+, K^+) co-doping

AFTAB ANSARI, SANCHITA DEY and DAMBARUDHAR MOHANTA*
Nanoscience and Soft Matter Laboratory, Department of Physics, Tezpur University, Tezpur 784028, India
*Author for correspondence (best@tezu.ernet.in)

MS received 20 April 2021; accepted 7 September 2021

Abstract. Structural and optoelectronic features as well as influence of local symmetry due to inclusion of dopants are being reported for nanoscale Eu^{3+}: Gd_2O_3 systems with alkali metal ion (Na^+, K^+) co-doping. The origin of red emission ($\sim$612 nm) as mediated by specific *D–F* transitions and nature of local symmetry are discussed. The co-doped nanosystems were synthesized following a citrate-gel route and a hydrothermal route as for nanoparticles (EuGNP) and nanorods (EuGNR), respectively. Revealing cubic crystal structure, X-ray diffractometer results also convey incorporation of the dopants into the host matrix, while the transmission electron microscopy images endorse formation of nearly spherical nanoparticles and nanorods. Photoluminescence responses exhibit augmentation in the emissions for the co-doped phosphors with the intensity ratio between the most intense electrically driven red emission at $\sim$612 nm ($^5D_0 \rightarrow {}^7F_2$) to be four-fold stronger than the magnetically driven orange emission $\sim$590 nm ($^5D_0 \rightarrow {}^7F_1$) in the case of Na^+ co-doped EuGNP system. Along with comparative emission intensity and line widths, the anomalous trend in emission feature of Na^+ co-doped EuGNR has also been discussed.

Keywords. Nanoscale; rare earth; optical; dopants; luminescence; *D–F* transition.

1. Introduction

In the last few decades, there has been a significant progress in the development of luminescent nanomaterials, particularly semiconductor quantum dots being deployed in bioimaging and biolabelling applications. On the other hand, the quest for suitable, efficient nanophosphors begun much lately with carefully chosen compounds that would offer highly stable, yet delayed emission responses. Processing of highly efficient, photostable, narrow band phosphors is quite encouraging [1,2]. Extensive research efforts were put in the past to derive nanophosphors from different kinds of materials, following various top-down as well as bottom-up approaches [3–7]. To be specific, as an important host of rare-earth oxide (REO), gadolinium oxide (Gd_2O_3) can accommodate suitable dopants to yield nanophosphors of certain kind. To be mentioned, commercial grade chelated gadolinium is in extensive use in diagnostics as a contrast agent for magnetic resonance imaging, and consequently, the rare-earth (RE) ion-doped Gd_2O_3 has an immense potential for dual imaging with combination of magnetic resonance imaging and luminescence-based analysis [8–10]. In a cubic crystal of Eu^{3+}:Gd_2O_3, the dopant Eu^{3+} ions normally occupy the available *C2*, or *S6* lattice sites upon substituting the Gd^{3+} ions. Earlier works suggest that, Gd_2O_3 matrix incorporated with Eu^{3+} ions could warrant a wide range of applications, including lamp and display devices, while revealing strong absorption signature in the UV range [11,12]. Moreover, accompanied by *D–F* transitions of Eu^{3+}, the emission provides a distinctive narrow-band feature with longer lifetimes and a relatively large Stoke's shift, thereby making the system a favourable bio-fluorophore candidate in various sorts of luminescence immunoassays [13,14]. Interestingly, a combination of two different RE ions, *viz.* Gd^{3+} and Eu^{3+} can also be utilized to realize quantum cutting processes, which is a two-photon down-conversion process that can lead to quantum efficiency >100% [15,16]. However, such two-step processes require VUV excitation and also require the material to be oxygen free, as oxygen impurities result in emission (non-radiative relaxations) via Eu-O charge transfer states [17].

Use of co-dopants has been a vital tool in order to achieve enhanced luminescence, especially in case of nanophosphors [18]. The co-doping can be performed by incorporating a RE dopant as well as a non-RE dopant. Among the latter kinds, alkali elements are widely selected as co-dopants owing to their varied and extensive relevance in luminescent hosts [19]. Typically, the ionic-radius and oxidation states of the alkali metal ions (M^+) differ from those of the host ions (Gd^{3+}). This in turn distorts the lattice

Published online: 22 January 2022

structure locally, thereby destroying the symmetry around Eu^{3+} site largely. Such distortions due to co-doping thence provide us with RE-based nanophosphors with enhanced colour parity [20,21]. Yu *et al* [22] have already reported modification in the local site symmetry of Eu(III) by co-dopants Li^+, Na^+ and K^+. Owing to their characteristic lower oxidation states and distinct ionic radii, the group observed an improved luminescence efficiency in the co-doped $SrZnO_2:Eu^{3+}$ [22]. Moreover, Li *et al* [23] have processed size-controlled $CaMoO_4:Tb^{3+}:M^+$ (M = Li, Na, K) phosphors by usual solid-state reaction routes and studied their phosphorescence in detail. Observably, the incorporation of M^+ in a varied, yet appropriate concentration into the host yielded a noteworthy enhancement in the emission response.

Of late, nanoscale one-dimensional (1D) systems gained considerable attention as important functional materials while taking advantage of their unique, 1D spatial confinement in addition to inherently large surface area [24,25]. The morphology of RE-doped nanophosphors can play a crucial role in the manifested emission intensity that would result due to a change in its specific surface area [26]. Moreover, such a variation in morphology has a dependency on various factors, including pH, annealing temperature, precursor as well as intermediate steps followed. Amongst many, hydrothermal routes enable a greater control over nano-structuring and homogeneous growth.

Following a facile route, herein, we highlight the processing of $Eu^{3+}:Gd_2O_3$ nanophosphors with inclusion of suitable co-dopants (Na^+, K^+) independently. The structural, optical absorption and concentration-dependent red-luminescence characteristics are discussed emphasizing the effect of co-doping wherever necessary.

2. Experimental: materials and methods

To synthesize Gd_2O_3 nanoparticles (GNP) and nanorods (GNR), we employed the well-known citrate-gel and hydrothermal routes [27], with necessary modifications for doping and co-doping aspects as discussed below.

2.1 *GNP with inclusion of dopants*

The facile, citrate-gel route involves gadolinium acetate (GdAc: $(CH_3COO)_3Gd$, CDH, 99.99% pure) as the main reactant. At first, a specific quantity of citric acid solution is added to the aqueous solution of GdAc, followed by mixing on a magnetic stirrer, for about 30 min. The final gel-like solution is oven dried at a temperature of 70°C and then subjected to calcination for about 4 h in a tube furnace set at a temperature of 600°C. Europium acetate (EuAc: $(CH_3COO)_3Eu$, CDH, 99.99% pure), sodium acetate (CH_3COONa, CDH, 99.99% pure) and potassium acetate (CH_3COOK, CDH, 99.99% pure) were added in stoichiometric proportions in order to consider inclusion of 1% Eu^{3+} into the Gd_2O_3 host along with the co-dopants as desired. Accordingly, we obtained samples such as, $Eu^{3+}:Gd_2O_3$ only (EuGNP), and $Eu^{3+}:Gd_2O_3$ co-doped with Na^+ and K^+ marked as, EuGNP(Na), and EuGNP(K); respectively.

2.2 *GNR with inclusion of dopants*

Knowing that top-down approach cannot deliver the requisite form of nanometric Gd_2O_3 from its bulk counterpart being thermally and mechanically stable, an alternative strategy is in place to suit the desired purpose [7,28]. It involves a three-step hydrothermal process: acidification, formation of hydroxide and eventual reduction to its nanometric oxide form. At first, in an aqueous solution containing 0.5 g of bulk Gd_2O_3 a suitable amount of conc. HNO_3 (69%) was added gently to obtain a nitrate product ($Gd(NO_3)_3$) in the form of a clear sol. A stoichiometric amount of Eu_2O_3 was also added to the mixture so as to incorporate 1% Eu^{3+} into the Gd_2O_3 host, marked as EuGNR. In the next step, the addition of NaOH was facilitated in order to reduce the nitrate compound formed in the first step to a hydroxide product ($Gd(OH)_3$). As for the synthesis of 1% $Eu^{3+}:Gd_2O_3$ co-doped with Na^+ and with K^+, suitable amounts of $NaNO_3$ (CDH, 99.99% pure) and KNO_3 (CDH, 99.99% pure) were transferred separately to the concerned precursor. The respective sample codes were EuGNR(Na) and EuGNR(K). In the next step, the precursors were subjected to autoclaving at a temperature of 140°C in a polypropylene-lined autoclave, for ~24 h. The final step involved calcination at a temperature of 600°C, for a time duration of ~5 h.

To be mentioned, the amount of alkali precursors, i.e., alkali acetates and alkali nitrates employed were so chosen that the ionic ratio between Eu^{3+} and M^+ ions remains equal in the solution. For instance, in order to acquire equal ionic concentrations between the dopant and co-dopant, 5 mg of $(CH_3COO)_3Eu$, and 2.4 mg of CH_3COONa and 2.83 mg of CH_3COOK were weighed and mixed suitably for preparing Na^+ and K^+ co-doped EuGNP systems, respectively. In contrast, as for hydrothermally derived GNR systems, 5 mg of Eu_2O_3, and 2 mg of $NaNO_3$ and 2.4 mg KNO_3 were added to fabricate Na^+ and K^+ co-doped EuGNR systems; respectively. The similarity in size and chemical behaviour between the Eu^{3+} and Gd^{3+} ions would thermodynamically favour the RE compound to be formed readily. The requirement of an equal ionic concentration of Eu^{3+} and M^+ is crucial to support the accurate co-doping of the later within the system of interest.

The nanoscale GNP and GNR products obtained were washed thoroughly and repetitively with the deionized (DI) water and AR-grade ethanol to yield products free from any undesired species and subsequently, kept ready for further characterizations.

2.3 *Analytical techniques employed*

Both diffraction and spectroscopic techniques were employed to characterize the GNP and GNR systems. Whereas, powder form has been considered for the diffraction measurements, a requisite amount of the specimen was suspended in DI water for spectroscopic studies. As for structural characterization of the GNP and GNR systems, a Rigaku Mini-Flex X-ray diffractometer (XRD) equipped with CuK_α radiation (λ = 1.54 Å) has been employed. The diffraction data could be acquired considering the range of Bragg's angle (2θ) ~10°–60° and with a precision of 0.05°. Optical absorption studies were performed on a dual beam Perkin Elmer spectrophotometer (UV-VIS Lambda 365, USA). On the other hand, luminescence spectra could be obtained on a Horiba fluorescence spectrophotometer while using the excitation line, λ_{ex} = 230 nm. Here, a relatively lower wavelength of excitation was intended to induce promotion of carriers across the wide bandgap of the host Gd_2O_3. In order to extract useful information, all the data were carefully analysed with appropriate curve fittings wherever necessary. The transmission electron microscopy (TEM) images for the products synthesized via citrate-gel route were captured on a JEOL 2100 machine, while a Tecnai G2 20 S-TWIN (200 kv) system was employed to reveal the morphological feature of the hydrothermally derived GNR. The time resolved photoluminescence (TR-PL) spectra were gathered from a Horiba fluorescence spectrophotometer enabled with the time correlated single photon counting (TCSPC) system, for a fixed emission wavelength (590 nm, 612 nm).

3. Results and discussion

3.1 *Structural and morphological features of nanoscale Gd_2O_3*

Acquired XRD patterns, as displayed in figure 1, reveal four prominent peaks that correspond to (222), (400), (440) and (622) crystallographic planes of the cubic crystalline structure of Gd_2O_3 (JCPDS No.76-0155) [28]. Independent of synthesis route followed for either GNP or GNR cases, most of the crystallites were believed to have grown with preferred orientation along the (222) plane. As no separate peaks of the byproduct (e.g., Eu_2O_3) can be traced in the diffractograms, the dopants need not crystallize separately. Given the comparable ionic sizes of Eu^{3+} (rad. ~108.7 pm) and Gd^{3+} (rad. ~93.8 pm), the dopant is expected to occupy the substitutional sites in the host Gd_2O_3 lattice. Incorporation of dopants into the interstitial sites is discarded as doping concentration is well below the permissible doping, beyond which concentration quenching and alloying would occur. Conversely, the incorporation of appropriate alkali metal ions into the Eu^{3+}:Gd_2O_3 lattice results in a substantial improvement in their crystallinity while the byproduct may account for superior particle formation [20]. In general, it is the cationic site of the host compound where both the RE dopants, Eu^{3+} and the alkaline ion, M^+ are randomly distributed, as a result of which distortions in the sublattice symmetry around the former would develop luminescent centres [29].

The average crystallite size (d), and micro-strain (ε) were estimated using the well-known Williamson–Hall (W–H) equation given by:

$$\beta \cos\theta = \frac{0.9\lambda}{d} + 4\varepsilon \sin\theta. \quad (1)$$

Here, β is the full-width at half-maxima (FWHM) in radians and 2θ is the Bragg's angle in degrees. The undoped GNP and GNR systems predict average crystallite sizes as, d ~4.2 and ~4.26 nm; respectively (figure 1 and table 1). However, the values slightly alter with doping and co-doping cases, offering a maximal crystallite size of ~8.3 nm for the EuGNR(K) system. Typically, ε ~10^{-3} with positive and negative signs to indicate either a compact or a relaxed system. Despite the difference in processing conditions, the average crystallite sizes are quite close with site-specific inclusions of dopant and co-dopant, while the specimens retain the cubic symmetry. The Eu^{3+} ions within a cubic *C*-type oxide Gd_2O_3 tend to enter into the six-fold coordinated sites in either of the two local site symmetries: *C2* point symmetry or *S6* point symmetry [30]. In the first type of symmetry, the Eu^{3+} ions are invariably substituted in a cubic arrangement such that the two oxygen atoms are placed on one of the face diagonals effectively. Almost all of the prominent electronic transitions revealed in the luminescent system can be associated with the ions present in this site [31]. In contrast, the *S6* site is considered to be of higher symmetry and comes with an inversion symmetry, such that two oxygen vacancies reside on a body-diagonal. In principle, the higher site symmetry yields intense transitions corresponding to both magnetic dipole as well as phonon-assisted weak vibronic transitions [32].

The degree of crystallinity has been estimated for the samples under study and shown in table 1. The as-prepared undoped GNP and GNR displayed excellent crystallinity; however, an observable decline in crystallinity can be witnessed upon inclusion of dopant (Eu^{3+}) and co-dopants (Na^+ and K^+). The crystallinity gets lowered upon co-doping with Na^+ and K^+ and to ~82%. Incorporation of dopants leading to the loss of crystallinity has already been shown by earlier groups and ascribed to adequate distortion in the host lattice [33,34]. The local strain developed in the system due to the introduction of ions of varying sizes can modify the periodicity as well as the crystal symmetry [35,36]. As for the co-dopants Na^+ and K^+, a difference in their ionic radii can lead to the manifestation of lattice defects, which in turn decreases the crystallinity as observed in our case [37].

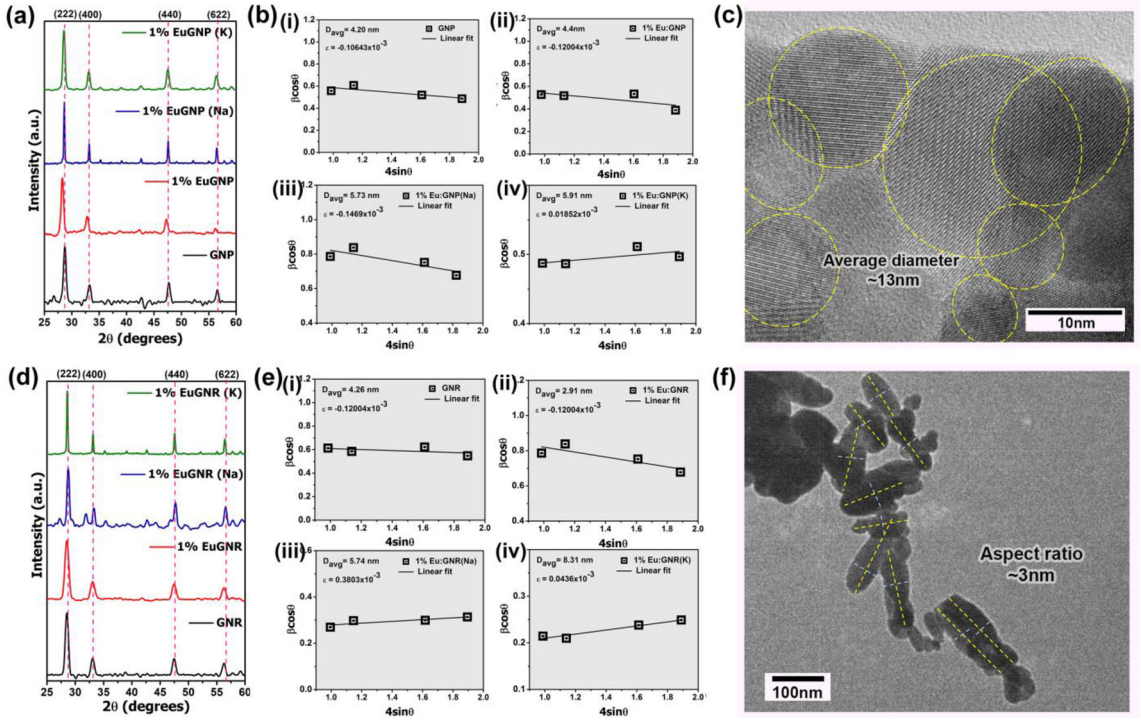

Figure 1. XRD patterns of the undoped and Eu^{3+}: Gd_2O_3 nanosystems with Na^+ and K^+ co-doping prepared via (**a**) citrate-gel (GNP) and (**d**) hydrothermal (GNR) routes. The corresponding W–H plots are shown in (**b**) and (**e**) for the nanoparticles and nanorods, respectively. Respective TEM images of nanoparticles and nanorods prepared are depicted in sub-figures (**c**) and (**f**).

Table 1. Energy gap and degree of crystallinity determined for undoped, doped and co-doped Gd_2O_3 nanosystems.

Nanoparticles (GNP)			Nanorods (GNR)		
Sample	E_g (eV)	Crystallinity (%)	Sample	E_g (eV)	Crystallinity (%)
GNP	5.72	96.73	GNR	5.74	96.96
1% EuGNP	5.88	96.67	1% EuGNR	5.51	94.22
1% EuGNP(Na)	5.66	92.09	1% EuGNR(Na)	5.69	71.20
1% EuGNP(K)	5.42	82.38	1% EuGNR(K)	5.70	86.48

In order to attain further insights from the systems relevant to their morphological features, TEM imaging was performed with care. TEM images invariably display spherical and rod-like morphologies for the GNP and GNR samples derived through the citrate-gel and hydrothermal route, respectively (figure 1c and f). Our observations are in concurrence with earlier reports, which revealed quite similar features [28,38]. The average diameter of nanoparticles was determined using *ImageJ*® software and was found to be ∼13 nm. On the other hand, the nanorods of varying aspect ratio were seen from the micrograph and giving an average aspect ratio close to 3. Although particles and nanorods do appear in un-clustered form, distinct isolated particles could not be imaged possibly due to inherent magnetic interactions.

3.2 *UV–Vis spectral features and the effect of doping and co-doping*

The typical optical absorption spectra exhibit absorption characteristics in the UV range with few poorly resolved peaks in the visible range (figure 2). These weaker transitions are usually attributed to intra-*4f* transitions of Eu^{3+}. Featuring a characteristic absorption peak at ∼231 nm, the GNP system reveals inter-band transitions of the Gd matrix, shown in figure 2a(i) [39]. In addition to the aforesaid peak, the EuGNP system offered a broad central maxima at ∼300 nm, which is ascribed to the transitions accompanied by the localized states created due to the inclusion of Eu as a dopant [39,40].

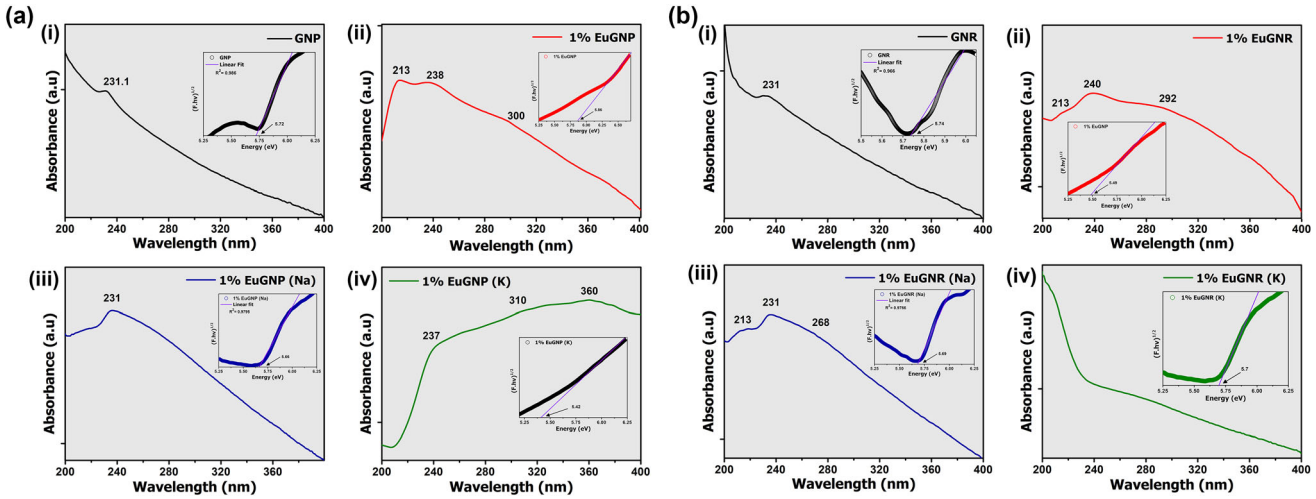

Figure 2. The UV–Vis optical responses of the Eu^{3+}: Gd_2O_3 nanosystems prepared by (**a**) citrate-gel route (GNP) and (**b**) hydrothermal route (GNR). The sub-figures are represented as: (i) undoped, (ii) 1% Eu doped without co-doping, and co-doped with (iii) Na^+ and (iv) K^+.

Knowing the off-white appearance of GNP and GNR powders, the absorbance values cannot be appreciated for determining their unusually high bandgaps. However, the reflectance values incorporated in Kubelka–Munk model can help determine their optical gaps eventually [41]. The Kubelka–Munk (K-M) function is given as:

$$F(R) = \frac{(1-R)^2}{2R}. \tag{2}$$

Here, F is directly proportional to the absorption coefficient, α, which depends on the incident photon energy and described through the power-law expression in accordance with Tauc's proposition:

$$\alpha h\nu = A\left(h\nu - E_g\right)^n, \tag{3}$$

where E_g stands for the optical energy gap, and n determines the nature of the involved inter-band transitions with values, 0.5, 1.5, 2 and 3 for the direct-allowed, direct-forbidden, indirect-allowed and indirect-forbidden transitions, respectively. A is a material-dependent parameter. Here, calculation has been made considering n = 2 as the RE oxides are largely characterized by indirect-allowed electronic transitions [21,42].

The *K–M* plot, shown as inset of figure 2, reveals the bandgap of GNP estimated to be ∼5.7 eV, which is comparatively higher than that of its bulk counterpart (∼5.4 eV). Such an increase can be attributed to the quantum confinement effect on conversion of bulk into nanoscale dimension [43]. Also the extent of distortion and disorder introduced due to doping and co-doping has a direct linkage with the observed variations in the bandgap (table 1). Subsequently, such changes incurred to the host can adequately modify the distribution of intermediary energy levels due to the uneven incorporation of Eu^{3+} into the rare-earth oxide matrix. Since the Eu^{3+} concentration is low (∼1%), local accumulation is quite improbable though it may have a dependency on the steps involved. The values of the bandgap ranging 5.4–5.8 eV are in decent agreement with the available reports [44]. The occupation of the Gd^{3+} sites by Eu^{3+} ions would give rise to oxygen vacancies, thereby affecting the energy band structure. The Na^+ and K^+ ions with respective atomic radii ∼0.97 and 1.33 Å are responsible for their occupation in the interstitial sites [21], and may lead to the extension of the host-lattice structure. This extension in turn weakens the bond strength as additional oxygen vacancies are formed [21]. Such vacancies are known to enhance the deformation degree of O2*p* orbitals along with perceptible superposition in their electronic wavefunctions. Introduction of new entrants, e.g., K^+ and Na^+ with oxidation states differing from that of the host Gd^{3+}, further perturbs their superposition. Effectively, a narrowing down of the gap can be ascertained with the absorption edge shifted towards the orange-red range of the visible spectrum upon alkali doping [21].

3.3 *Effect of doping and co-doping on luminescence features*

The room temperature PL emission spectra of the as-prepared Gd_2O_3:Eu^{3+} nanosystems co-doped with Na^+ and K^+ ions are mainly depicted in the orange-red regime, in figure 3a(i–vi). In order to acquire a thorough evaluation and a better perspective at large, the asymmetric PL spectra were deconvoluted with the normalized multi-peak Gaussian fitting. The condition was to match experimental curve with the empirical curve, later being emerged as consequence of superposition of deconvoluted parts. With a good statistical agreement, such a fitting enables us to identify the peak positions and compare intensities as well as FWHM at large.

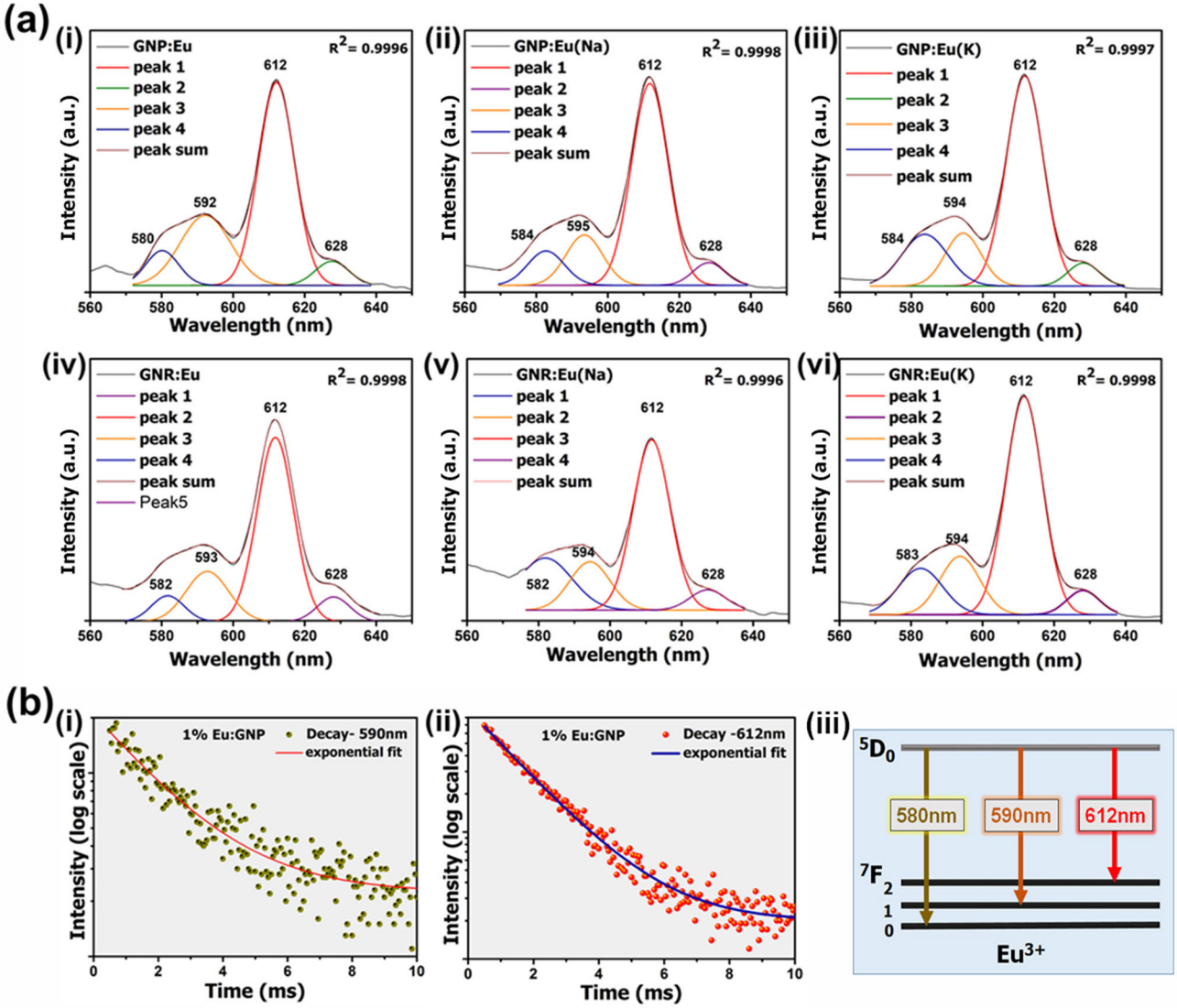

Figure 3. (**a**) De-convoluted photoluminescence spectra of (i) EuGNP, (ii) EuGNP(Na), (iii) EuGNP(K), (iv) EuGNR, (v) EuGNR(Na) and (vi) EuGNR(K) nanosystems. (**b**) TR-PL decay curves for 1% EuGNP system corresponding to emission peak (i) ~590 and (ii) ~612 nm. A schematic of important transitions is illustrated in **b**(iii).

In the PL spectra, the most intense peak maxima are positioned at ~612 nm in addition to other characteristic bands located at ~580, 590, 612 and 626 nm (figure 3a). The weak emission band observed at ~590 nm can be assigned to the $^5D_0 \rightarrow {}^7F_1$ transitions of Eu^{3+} [11]. As for the Eu^{3+} emission profile via $^5D_0 \rightarrow {}^7F_J$ transitions, the peaks are generally encountered at ~580, 590, 615, 650, 720 for $J = 0, 1, 2, 3, 4$; respectively [39]. To be mentioned, the emission line at ~590 nm is attributed to the magnetic dipole-driven (MD) transitions, $^5D_0 \rightarrow {}^7F_1$; while the other two emissions located at ~612 and 626 nm are assisted via electric dipole-driven (ED) transitions of Eu^{3+} ions, $^5D_0 \rightarrow {}^7F_2$. Depending on the chemical environment of the ions, the shape of the spectra may differ appropriately with a change in the relative intensity as well as crystal field splitting of the bands. The ED transitions are known to be hypersensitive in nature; i.e., its emission profile may alter with the local symmetry around the luminescent centres. The dopant Eu^{3+} ion obeys the selection rule ($\Delta J = 2$) and is known to be forced electric-dipole driven [45]. The ED peak at ~612 nm dominates the entire spectra, whereas, a relatively weak subsidiary peak at ~626 nm is due to the splitting of the ~612 nm transition. Remarkably, the Eu^{3+} transitions were known to split with a degeneracy of $(J + 1)$ [39]. The MD transitions, largely, are independent of local environment of the activator site, while the ED ones are hypersensitive to the local structure around Eu^{3+} ions. Here, we also witnessed the ED-based $^5D_0 \rightarrow {}^7F_0$ transitions positioned at ~580 nm, which is rarely discussed in the existing literature. The intensity distribution of the transitions among different $^5D_0 \rightarrow {}^7F_J$ ($J = 0, 1, 2, 3$) levels are dependent on the local symmetry of the dopant ions and can

be described in terms of Judd–Ofelt theory [27,46]. Accordingly, the MD transition is an allowed transition, while the ED is a parity forbidden one. Nevertheless, for the Eu^{3+} ions residing in the *C2* sites, local symmetry of the activators will not necessarily provide any inversion centre. In such cases, the parity forbidden is partially allowed and hence the imparted transition is termed as the forced one.

The TR-PL data of the 1% EuGNP at a fixed emission of ~590 nm (MD) and 612 nm (ED) are depicted in figure 3b(i,ii). The decay profiles follow single exponential trends while revealing respective lifetimes as ~1.98 and ~1.55 ms. Earlier also the lifetime accompanied by the MD transitions was found to bear a higher value than that of the hypersensitive ED transition [15]. Furthermore, lifetime was shown to be dependent on the site allocation for the dopant Eu^{3+} ions and typically, ~1 ms for the *C2* site, and increases up to ~3–4 ms for the *S6* site [31]. Our observations suggest that Eu^{3+} ions would preferably occupy the C_2 sites in the host Gd_2O_3, with occasional occupancy at the S_6 site. Figure 3b(iii) provides a schematic representation of the major transitions involved in the given system.

The effect of co-doping generally accounts for enhancing the PL response, as can be found in figure 4a and b. The EuGNP system offers a greater augmentation in the emission with K^+ co-doping as compared to its Na^+ co-doping counterpart, or simply without co-doping. We further analysed the intensity of the ED transition (~612 nm, red emission) relative to the MD transition (~590 nm, orange emission), shown in figure 4c and table 2. It clearly shows that the ED-to-MD intensity ratio is relatively higher for the nanorod system (EuGNR) than the nanoparticles (EuGNP), and without co-doping cases. When co-doped with either Na^+ or K^+, it was EuGNP that gave a stronger feature. Observably, the intensity ratio rises from ~2.9 for EuGNP to nearly four times upon co-doping with the alkali ions (figure 4c and table 2). Conversely, the EuGNR system exhibits a value of ~3.67, which enhances only slightly up to 3.74 with the inclusion of co-dopant K^+ into the EuGNR system (figure 4c). Interestingly, upon co-doping with Na^+, the intensity ratio dropped to ~3.5. Figure 4d displays the schematic representation of underlying mechanisms, such as energy sensitization and energy transfer between the involved dopant and co-dopants, leading to apparent augmentation of luminescence discussed in later sections. We have also compared the subsidiary ED, ~626 nm peak with the MD peak, ~590 nm peak, and observed a rise in case of the co-doped EuGNP (figure 5a). However, a steady fall has been realized in the case of the co-doped EuGNR (figure 5b). This anomalous observation is discussed in the successive sections.

3.3a *Effect of co-doping on local symmetry:* Eu^{3+} ions occupying the sites with inversion centres reveal intense $^5D_0 \rightarrow {}^7F_1$ transition peaks, while the $^5D_0 \rightarrow {}^7F_2$ transition remains parity forbidden. Thus, for intense red emission ($^5D_0 \rightarrow {}^7F_2$), it is required that the Eu^{3+} ions are located away from the inversion centre and in addition, their local symmetry be distorted. It is widely accepted that the magnetic dipole transition centring at ~590 nm ($^5D_0 \rightarrow {}^7F_1$) is independent of local environment, while the electric dipole transition centring at ~612 nm ($^5D_0 \rightarrow {}^7F_2$) is hypersensitive to the site symmetry of local environment around Eu^{3+} ions. In this context, it is necessary to evaluate our observations in view of the intensity ratio and FWHM ratio of transitions with respect to that of the $^5D_0 \rightarrow {}^7F_1$. Know that intensity describes the number of transitional events occurring in each transition while FWHM is linked with their line broadening aspect. Figures 5 and 6 display the relative intensity ratios of the observed important transitions. Upon co-doping, the intensity ratio as well as FWHM ratio of 590 nm peak ($^5D_0 \rightarrow {}^7F_1$)-to-580 nm peak ($^5D_0 \rightarrow {}^7F_0$) would drop substantially (figure 5a and b). It is important to note that the intensity of MD transition (~590 nm) is insensitive to the changes in local symmetry of dopants and the observation suggests that the 580 nm peak has been broadened. Notably, the intensity and the FWHM of the peak positioned at ~580 nm defines the amount of Eu^{3+} ions occupying C_{nv}, C_n or C_s symmetry [30]. Also, in figure 6a, we observe a decline in intensity ratio between the ~612 and ~580 nm peak. This in turn suggests that the co-doping results in a more intense ~580 nm peak as the co-doping led occupation in *C2* sites has risen noticeably. Apparently, GNPs derived via citrate-gel route are likely to offer a better co-doping effect in the desired *C2* sites as compared to the hydrothermally processed GNR.

Integration of alkali co-dopant metal ions in the host lattice structure generates local stress in the adjacent ions and disturbs the native environment of activator ions. The alkali metal ions substitute for Gd^{3+} in the matrix, which could then aggravate the local symmetry and result in the formation of point defects, mainly oxygen vacancies. These defects can act as sensitizer and facilitate transfer of energy between the host Gd^{3+} and Eu^{3+} ions. Such a strong mixing of charge-transfer states can eventually lead to augmentation in the emission profiles [47]. Depending on their ionic radii and type of co-dopants it would affect local structural ordering. While some ions act as sensitizers, others enter into the host lattice which promotes creation of oxygen vacancies, primarily realized in oxide compounds [48,49]. The co-dopants may also alter the crystal field due to the host matrix adjoining the activator ions, thus affecting their phosphorescence [18]. The mismatch in the ionic radii and charge state of M^+ with that of the host RE ions could act as the cause for the introduction of some bound *e–h* pairs. As a consequence of generation of stress, the reduced symmetry alters the crystal field around the Eu^{3+} ions and improve the possibility of radiative electronic transitions, which leads to a rise in PL emission intensity with lifted parity selection rule [50,51]. Furthermore, manifestation of lattice defects due to incorporation of co-dopants as revealed by decrease in crystallinity and thereby the increment in dislocation density, greatly influences the local symmetry of the Eu^{3+}

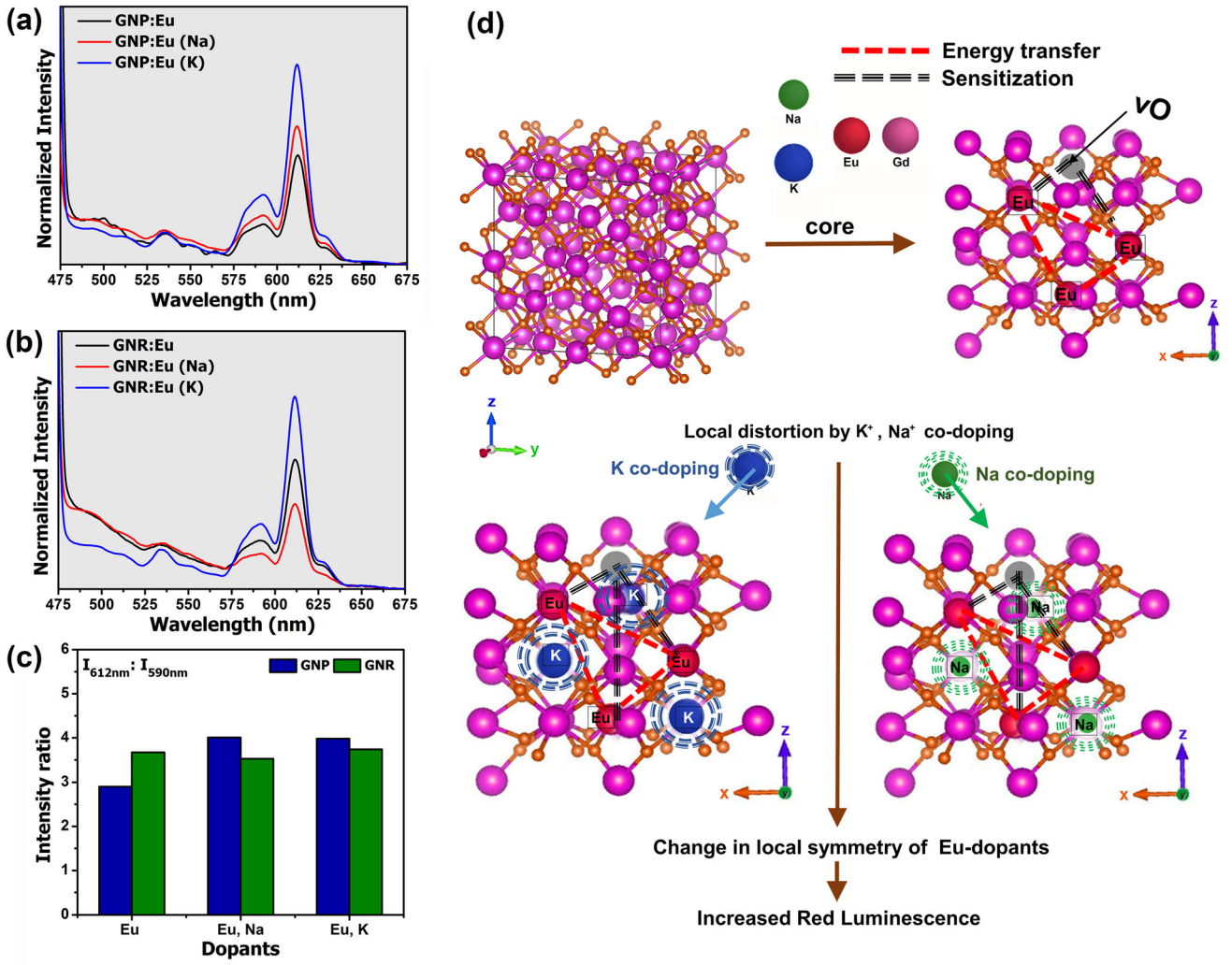

Figure 4. Normalized PL features without and with co-doping: (**a**) GNP and (**b**) GNR nanosystems. The ED-to-MD transition intensity ratios of the samples are depicted in **c**, on a comparative basis. The underlying mechanism on the augmentation of emission process is shown in a scheme in (**d**).

Table 2. Relative intensity ratios for various $D \rightarrow F$ transitions for doped and co-doped Gd_2O_3 nanosystems.

Samples	Ratio (nm)	Relative intensity		
		Eu only	Eu with Na	Eu with K
GNP	612–580	5.83	5.87	4.06
	612–590	2.90	4.01	3.98
	626–590	0.35	0.45	0.44
	590–580	0.49	0.42	0.42
GNR	612–580	7.12	3.27	4.71
	612–590	3.67	3.53	3.74
	626–590	1.94	0.93	1.26
	590–580	2.01	1.47	1.02

ions. The availability of uneven ionic charges could lead to the enhancement of the local distortion, thereby facilitating ED-mediated transitions [39].

Transitions from $^5D_1$ levels are responsible for the occurrence of peaks in the blue-green regime. If we observe closely in figure 4, the peak intensity in the blue-green regime has decreased in the case of EuGNR(K). This indicates that there is an increase in population levels in the $^5D_0$ level due to radiationless transition from higher energy levels like, $^5D_1$, $^5D_2$ to ground $^5D_0$ level, followed by the increase in intensity in the red regime. Although the emission intensity of EuGNR(Na) drops as compared to that of the EuGNR, it is observed that the intensity ratio of the two major *D–F* transitions (612 and 590 nm) is greater in EuGNR system as compared to that of the EuGNP (figure 4c). However, the ratio of intensity of the two transitions is maximal in the case of co-doping with Na^+ for specimen EuGNP(Na), which allows it to be termed as a better red phosphor amongst the ones studied. Surprisingly, as for nanorods, the ratio does not increase largely and lies between $\sim$3.5 and 3.8. While elaborating the results, the variation in ionic radii should also be held accountable. The

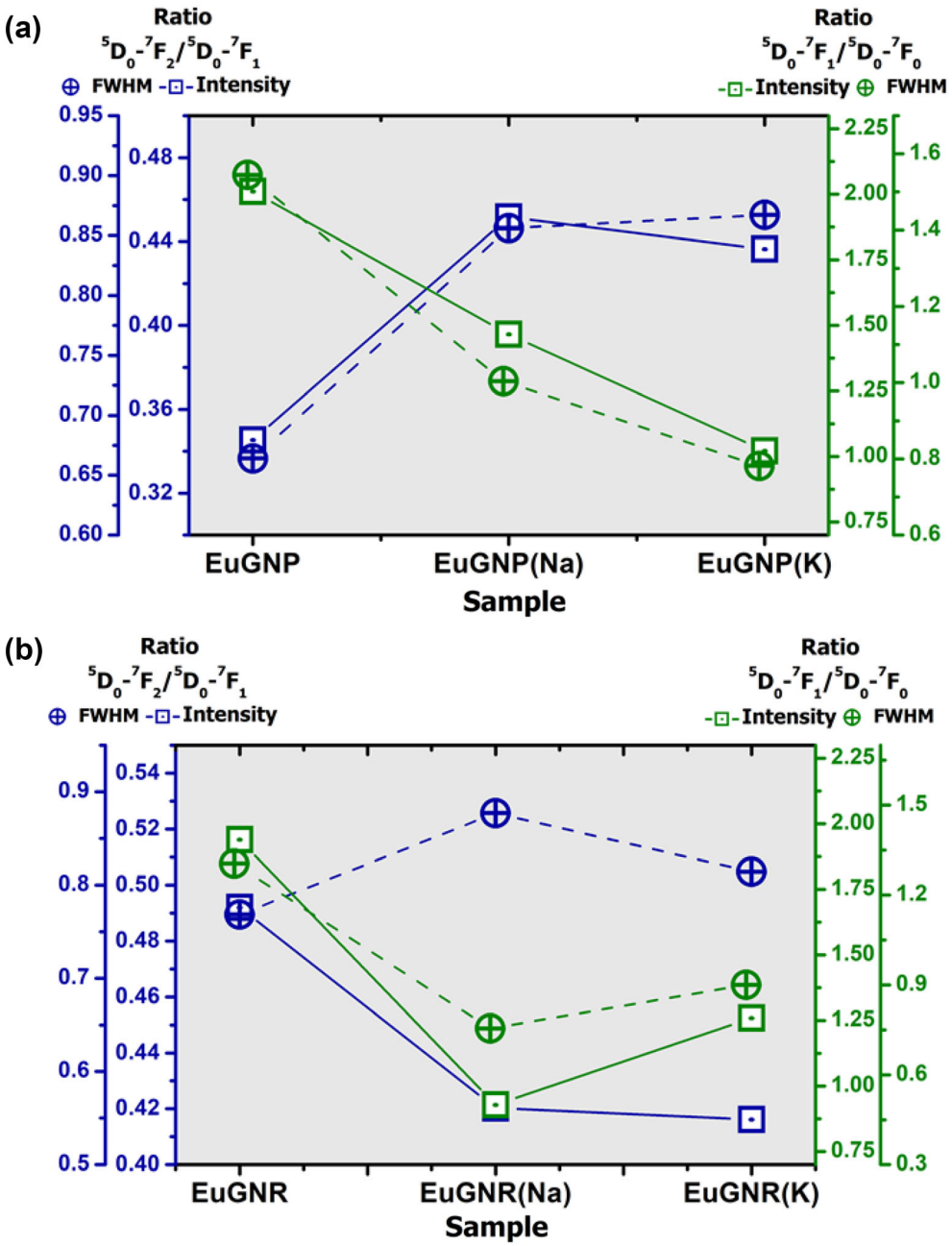

Figure 5. Comparison of the selective transitional intensities and FWHM ratios for the emission peaks located at ~626 nm ($^5D_0 \rightarrow {}^7F_2$), ~590 nm ($^5D_0 \rightarrow {}^7F_1$) and ~580 nm ($^5D_0 \rightarrow {}^7F_0$) for (**a**) GNP and (**b**) GNR systems.

radius of K^+ is 1.33 Å while that of Na^+ is 0.97 Å. The variation upsurges the range of available sub-lattice structure around the activators, thereby stimulating the spin-orbit coupling and also disturbs the crystal field effect on Eu^{3+} ions [52]. Creation of some bound electron–hole pairs due to incorporation of metal alkali atoms in the host can also be speculated.

3.3b *Effect of morphology on luminescence response:* As shown in figure 3, most of the nanosystems presented a better PL response in the presence of co-dopants. This can be validated considering the presence of surface trap sites that quench the luminescence profiles [53]. The nanorods are formed due to oriental attachment of nanoparticles and are greater in size as compared to the spherical nanoparticles. It has been reported that the particle size has negligible effect in the $D \rightarrow F$ transitions of Eu^{3+} ions considering the intra *4f* transition-mediated emission bands in Eu^{3+} ions [54,55]. However, a smaller size implies a larger surface area and thus a greater number of defects

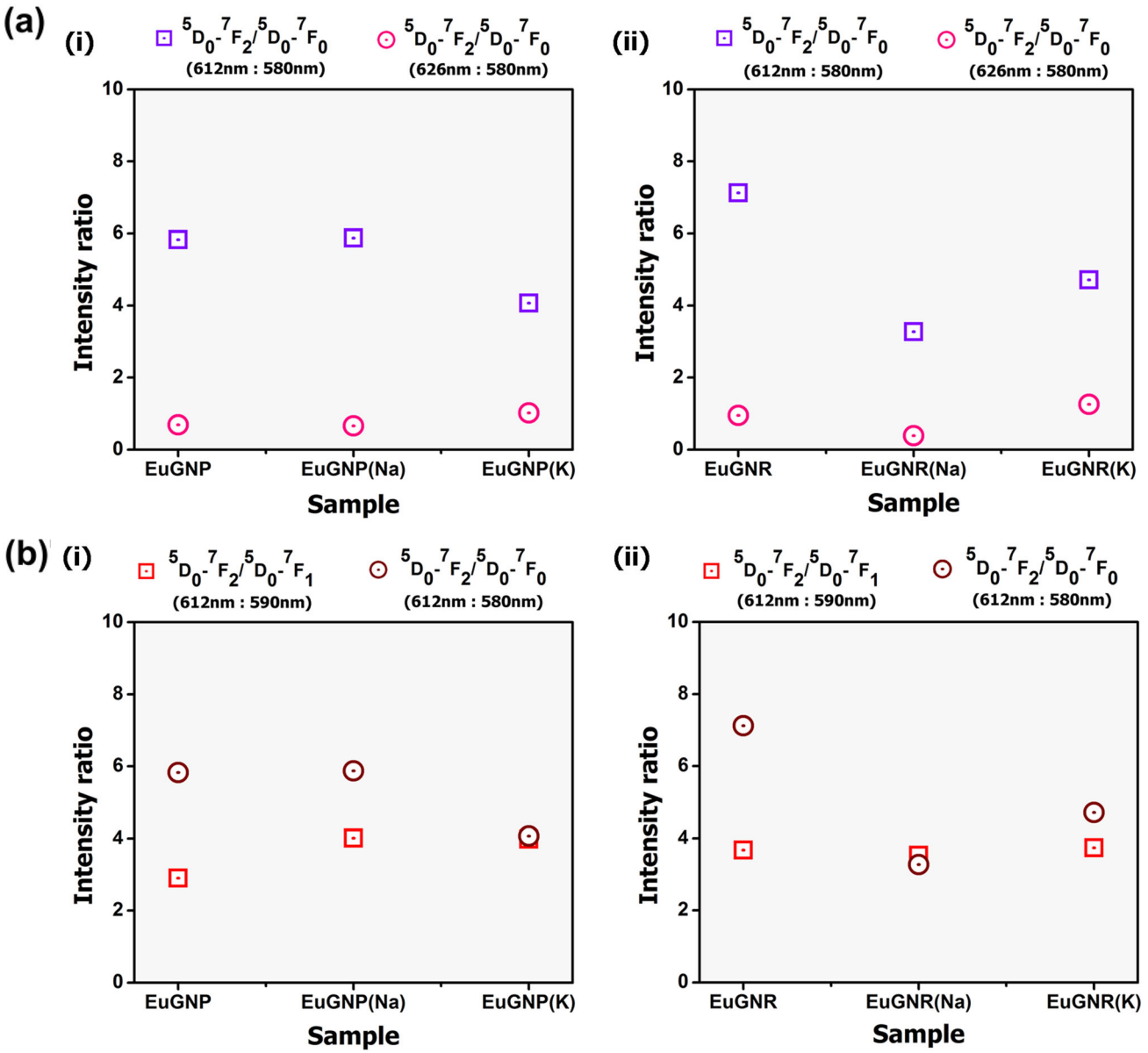

Figure 6. A comparative account of the PL relative intensity features accompanied via different transitions for the GNP and GNR nanosystems.

would act as quenchers rather than sensitizing the luminescence response [56,57]. A decrease in thickness also implies decrement in radiative transition probability due to surface quenching effect, resulting in trapped energy of activators by surface defects and other quenching sites present in the surface [58]. As compared to the nanorods, nanoparticles have greater surface areas and hence quenching due to near-surface sites is prevailed. Surface sites also carry dominant recombination routes, which however can be shifted upon by incorporation of an impurity in the confined structure.

The morphology dependent emission intensity observed in our case can also be corroborated considering the variation in number of particles per unit area facing towards incident light. This tends to change according to variation in morphological features and thereby the number is different for particles and rods [59]. For RE-based activators, the transition induced by dopants can be localized and thereby significant increase in the radiative efficiency of emission can be observed [60]. Non-radiative transitions decrease with an increment in aspect ratio and thus EuGNR system with aspect ratio ~ 3 displayed a better luminescent behaviour as compared to the EuGNP having aspect ratio unity [61]. 1D nanostructures can also display lower *e–h* recombination rate due to a greater mobility of electrons being laterally confined and are guided to move in axial direction [61,62]. Henceforth, the PL behaviour of GNRs can be improved upon either by modifying the aspect ratio or by incorporation of dopants/co-dopants [63].

3.3c *Cause of anomalous trend in EuGNR with Na^+ co-doping:* It was a matter of surprise on observing an anomalous trend in the PL emission feature of the EuGNR system with the red emission not augmented upon co-doping with Na^+. The possible reason can be elaborated considering the reactants used in the hydrothermal route. The route normally involves fixing of pH using NaOH as base and HNO_3 as the acidic component. The acid reduces RE oxides into their nitrate products; upon a maintained pH by addition of NaOH, RE hydroxides are produced with $NaNO_3$ being the possible byproduct in the reaction. Notably, the crystallinity predicted for EuGNR(Na) was compromised as compared to EuGNP(Na), which may imply that incorporation of Na^+ into the lattice is more favoured in the latter case. The general reactions for obtaining GNR can be as described below:

$$\text{Bulk } Gd_2O_3 + HNO_3 \rightarrow Gd(NO_3)_3 + 3H_2O$$

$$Gd(NO_3)_3 + NaOH \rightarrow Gd(OH)_3 + 3NaNO_3$$

$$Gd(OH)_3 \rightarrow \text{Nanoscale } Gd_2O_3$$

While for Na^+ co-doping the precursor used is $NaNO_3$, it is highly possible that various sites are already occupied by Na^+ during the preparation of EuGNR and hence the increment in the 612-to-590 nm ratio as compared to that prepared EuGNP via the citrate-gel route. With the addition of $NaNO_3$ the reaction is compromised with a tendency to go beyond the optimal doping of Na^+ ions, which in turn could not assist further incorporation of Na^+ into the host matrix. The intensity ratio is at par with the EuGNR, yet more than that of EuGNP. An excess of atoms could also aggregate on the grain boundaries due to a lower solubility of alkali atoms in Eu^{3+}:Gd_2O_3, leading to surface states that would affect the surface kinetics. The low level of crystallinity revealed for EuGNR(Na) implies that the synthesis route is not suitable to produce highly crystalline sample and a reasonable amount of unwanted byproduct is attained. Existing literature also suggests that for the $^5D_0 \rightarrow {}^7F_2$ transition in RE-based system, the choice of precursors also plays a significant role [54]. On the other hand, an increased shielding of the Eu^{3+} activator ions from quenching collisions in RE acetates can result in an increased asymmetry in Eu^{3+} local environment [54]. Such shielding involved in routes with acetate precursors (citrate-gel route) can facilitate adequate ligand–ligand exchange between the activator RE species and co-dopant alkali ions, which could activate radiative mechanism [64] and consequently, a profound increase in PL intensity has been observed.

4. Conclusions

Both the citrate-gel and hydrothermal routes are found suitable for processing alkali metal ion co-doped Eu^{3+}:Gd_2O_3 in the form of nanoparticles and nanorods possessing cubic crystalline structure, which exhibits enhanced luminescent behaviour with an exception for the case of EuGNR(Na). As revealed from the optical measurements, owing to quantum confinement effect the typical bandgap of the GNP and GNR systems can be greater than the typical bulk value of $\sim$5.4 eV. Effect of using Na^+ and K^+ as co-dopants on the PL emission properties of EuGNP and EuGNR phosphors has been discussed. The results indicate remarkable improvement in the red ($^5D_0 \rightarrow {}^7F_2$) and orange ($^5D_0 \rightarrow {}^7F_1$) emission features upon incorporation of K^+ ion as the co-dopant for the nanosystems. Interestingly, hydrothermally derived nanorods do not evidently favour enhancement of red emission upon Na^+ co-doping. This is because, as $NaNO_3$ being produced in an intermediate step can supply excess of Na^+ given that, $NaNO_3$ is also chosen as a precursor in our synthesis and can help aggregate on the particle grain boundaries. The enhancement in luminescence can be considered as that result of the alkali metal ions substitution in Gd^{3+} sites and creation of oxygen vacancies capable of acting as sensitizers for the energy transfer between the host and activator ions. The improvement of PL intensity may also be credited to the distortion in crystal field surrounding Eu^{3+} activator due to the inclusion of the alkali metal ions as co-dopant, which led to the enhancement of red emission in the phosphors. The role and scope of co-doping on modulating optical and opto-electronic properties is viewed as an all-time control aspect in advanced nanofabrication and applications.

Acknowledgements

We extend our sincere thanks to the SAIC, TU, for extending TEM facility. We also thank UGC-DAE CSR Kolkata Centre, for their help and support in TR-PL data acquisition. One of the authors (AA) thank Tezpur University for providing support under Research & Innovation Grant. The help and assistance received from the peers and colleagues are acknowledged.

References

[1] Weber M J 2002 *J. Lumin.* **100** 35
[2] Zych E, Brecher C and Lempicki A 1998 *Spectrochim. Acta A Mol. Biomol. Spectrosc.* **54** 1763
[3] Kang Y C, Park S, Lenggoro I and Okuyama K 1999 *J. Phys. Chem. Sol.* **60** 379
[4] Bazzi R, Flores M, Louis C, Lebbou K, Zhang W, Dujardin C *et al* 2004 *J. Coll. Interf. Sci.* **273** 191
[5] Chen H, Zhang J, Wang X, Gao S, Zhang M, Ma Y *et al* 2006 *J. Coll. Interf. Sci.* **297** 130
[6] Hirai T, Hirano T and Komasawa I 2002 *J. Coll. Interf. Sci.* **253** 62
[7] Dhananjaya N, Nagabhushana H, Nagabhushana B, Chakradhar R, Shivakumara C and Rudraswamy B 2010 *Physica B* **405** 3795

[8] Bridot J-L, Faure A-C, Laurent S, Riviere C, Billotey C, Hiba B *et al* 2007 *J. Am. Chem. Soc.* **129** 5076
[9] Louis C, Bazzi R, Marquette C A, Bridot J-L, Roux S, Ledoux G *et al* 2005 *Chem. Mater.* **17** 1673
[10] Garcıa-Murillo A, Le Luyer C, Dujardin C, Martin T, Garapon C, Pedrini C *et al* 2002 *Nucl. Instrum. Methods Phys. Res. A* **486** 181
[11] Blasse G and Grabmaier B (eds) 1994 *Luminescent materials* (Berlin: Springer)
[12] Yamamoto H 1996 *J. Soc. Inf. Disp.* **4** 165
[13] Feng J, Shan G, Maquieira A, Koivunen M E, Guo B, Hammock B D *et al* 2003 *Anal. Chem.* **75** 5282
[14] Goldys E M, Drozdowicz-Tomsia K, Jinjun S, Dosev D, Kennedy I M, Yatsunenko S *et al* 2006 *J. Am. Chem. Soc.* **128** 14498
[15] Wegh R, Donker H, Oskam K and Meijerink A 1999 *J. Lumin.* **82** 93
[16] Chouryal Y N, Sharma R K, Ivanovskikh K V, Ishchenko A V, Shi Q, Ivanov V Y *et al* 2021 *New J. Chem.* **45** 1463
[17] Ghosh P and Mudring A-V 2016 *Nanoscale* **8** 8160
[18] Liu X, Han K, Gu M, Xiao L, Ni C, Huang S *et al* 2007 *Solid State Commun.* **142** 680
[19] Li J, Wang Y and Liu B 2010 *J. Lumin.* **130** 981
[20] Dhananjaya N, Nagabhushana H, Nagabhushana B, Rudraswamy B, Shivakumara C and Chakradhar R 2011 *J. Alloys Compd.* **509** 2368
[21] Dhananjaya N, Nagabhushana H, Nagabhushana B, Rudraswamy B, Shivakumara C, Narahari K *et al* 2012 *Spectrochim. Acta A Mol. Biomol. Spectrosc.* **86** 8
[22] Yu X, Xu X, Zhou C, Tang J, Peng X and Yang S 2006 *Mater. Res. Bull.* **41** 1578
[23] Li X, Yang Z, Guan L, Guo J, Wang Y and Guo Q 2009 *J. Alloys Compd.* **478** 684
[24] Hu J, Li L-S, Yang W, Manna L, Wang L-W and Alivisatos A P 2001 *Science* **292** 2060
[25] Xia Y, Yang P, Sun Y, Wu Y, Mayers B, Gates B *et al* 2003 *Adv. Mater.* **15** 353
[26] Jia G, Huang Y, Song Y, Yang M, Zhang L and You H 2009 *Eur. J. Inorg. Chem.* **25** 3721
[27] Wang G, Wang Z, Zhang Y, Fei G and Zhang L 2004 *Nanotechnology* **15** 1307
[28] Hazarika S, Paul N and Mohanta D 2014 *Bull. Mater. Sci.* **37** 789
[29] Van Vliet J P M, Blasse G and Brixner L H 1988 *J. Solid State Chem.* **76** 160
[30] Binnemans K and Görller-Walrand C 1996 *J. Rare Earths* **14** 173
[31] Antic-Fidancev E, Lemaitre-Blaise M and Caro P 1982 *J. Chem. Phys.* **76** 2906
[32] Antic-Fidancev E, Hölsä J, Lastusaari M and Lupei A 2001 *Phys. Rev. B* **64** 195108
[33] Pal M, Pal U, Jiménez J M G Y and Pérez-Rodríguez F 2012 *Nanoscale Res. Lett.* **7** 1
[34] Lee K, Na H, Sohn H and Kim J 2014 *J. Korean Phys. Soc.* **65** 709
[35] Karmakar R, Neogi S, Banerjee A and Bandyopadhyay S 2012 *Appl. Surf. Sci.* **263** 671
[36] Singh P, Kaushal A and Kaur D 2009 *J. Alloys Compd.* **471** 11
[37] Deekshitha U G, Upadhya K, Antony A, Ani A, Nowak M, Kityk I *et al* 2019 *Mater. Sci. Semicond. Process.* **101** 139
[38] Hazarika S and Mohanta D 2013 *EPJ Appl. Phys.* **62** 30401
[39] Mukherjee S, Dasgupta P and Jana P K 2008 *J. Phys. D: Appl. Phys.* **41** 215004
[40] Rahman A A, Vasilev K and Majewski P 2011 *J. Coll. Interf. Sci.* **354** 592
[41] Kubelka P and Munk F 1931 *Z. Tech. Phys.* **12** 593
[42] Liu X, Zhou F, Gu M, Huang S, Liu B and Ni C 2008 *Opt. Mater.* **31** 126
[43] Kennedy R and Campbell J 1980 *J. Phys C Solid State Phys.* **13** 5341
[44] Samsonov G V (ed) 1982 *The Oxide handbook* (US: Springer)
[45] Ofelt G 1962 *J. Chem. Phys.* **37** 511
[46] Li G, Lai Y, Cui T, Yu H, Liu D and Gan S 2010 *Mater. Chem. Phys.* **124** 1094
[47] Jeong J H, Yang H K, Shim K S, Jeong Y R, Moon B K, Choi B C *et al* 2007 *Appl. Surf. Sci.* **253** 8273
[48] Yi S-S, Bae J S, Shim K S, Jeong J H, Park J-C and Holloway P 2004 *Appl. Phys. Lett.* **84** 353
[49] Chi L S, Liu R S, Lee B J 2005 *J. Electrochem. Soc.* **152** J93
[50] Macfarlane R and Shelby R 1987 in A A Kaplyanskii and R Macfarlane (eds) *Modern problems in condensed matter sciences* (The Netherlands: North-Holland Physics Publishing) Vol 21, p 51
[51] Waldrip K E, Lewis J, Zhai Q, Puga-Lambers M, Davidson M R, Holloway P H and Sun S-S 2001 *J. Appl. Phys.* **89** 1664
[52] Shi S, Gao J and Zhou J 2008 *Opt. Mater.* **30** 1616
[53] Wang X, Xu J, Yu J, Bu Y, Marques-Hueso J and Yan X 2020 *Phys. Chem. Chem. Phys.* **22** 15120
[54] Sharma P, Jilavi M, Nass T and Schmidt H 1998 *J. Mater. Sci. Lett.* **17** 823
[55] Leng Z, Zhang N, Liu Y, Li L and Gan S 2015 *Appl. Surf. Sci.* **330** 270
[56] Yang L, Zhou L, Huang Y and Tang Z 2011 *Mater. Chem. Phys.* **131** 477
[57] Shao B, Zhao Q, Guo N, Jia Y, Lv W, Jiao M *et al* 2013 *CrystEngComm.* **15** 5776
[58] Wang F, Wang J and Liu X 2010 *Angew. Chem. Int. Ed.* **49** 7456
[59] Sharma P K, Jilavi M H, Burgard D, Nass R and Schmidt H 1998 *J. Am. Ceram. Soc.* **81** 2732
[60] Bhargava R N 1997 *J. Lumin.* **72–74** 46
[61] Yang E, Li G, Fu C, Zheng J, Huang X, Xu W *et al* 2015 *J. Alloys Compd.* **647** 648
[62] Wang Z, Wu L, Zhou J, Cai W, Shen B and Jiang Z 2013 *J. Phys. Chem. C* **117** 5446
[63] Chall S, Mati S S, Rakshit S and Bhattacharya S C 2013 *J. Phys. Chem. C* **117** 25146
[64] Matthews L R, Wang X-J and Knobbe E 1994 *J. Non-Cryst. Solids* **178** 44